DETERMINISTIC DESIGN OF PEPTIDE-MEMBRANE INTERACTIONS

BY

NATHAN WARREN SCHMIDT

DISSERTATION

Submitted in partial fulfillment of the requirements
for the degree of Doctor of Philosophy in Physics
in the Graduate College of the
University of Illinois at Urbana-Champaign, 2011

Urbana, Illinois

Doctoral Committee:

Assistant Professor Yann R. Chemla, Chair
Professor Gerard C. L. Wong, Director of Research
Professor Kenneth S. Schweizer
Professor Robert M. Clegg

Abstract

Antimicrobial peptides (AMPs) are present in virtually every multi-cellular organism and comprise an important component of the innate host defense system. Collectively, AMPs have broad spectrum and selective microbicidal effects. A general mechanism of AMP activity is destabilization of the physical integrity of cell plasma membranes leading to depolarization, leakage, and eventual cell death. This thesis provides a detailed molecular model how AMPs destabilize membranes specifically, based upon their fundamental structural motif: they are amphipathic and cationic. Generic electrostatic and hydrophobic interactions between a cationic, amphipathic AMP and a cell membrane lead to strong binding between the peptide and membrane and subsequent partial insertion of the peptide into the bilayer. The physical chemistry of AMPs leads to a whole taxonomy of local membrane distortions, specific combinations of which are topologically active and can lead to membrane destabilization. AMPs permeabilize model bacterial membranes but not model eukaryotic membranes by selectively generating topologically active saddle-splay ('negative Gaussian') curvature in membranes rich in negative curvature lipids and anionic lipids, compositions characteristic of bacterial cell membranes. A mechanism of action based on saddle-splay membrane curvature generation is broadly enabling, since it is a necessary condition for processes such as pore formation, blebbing, budding, vesicularization, all of which destabilize the barrier function of cell membranes. The topological requirement for saddle-splay curvature places constraints on the amino acid compositions of membrane disruptive peptides. In AMPs decreasing arginine content is offset by a simultaneous increase in lysine and hydrophobic content. This 'saddle-splay curvature design rule' is consistent with the amino acid compositions of 1,080

known cationic AMPs. Furthermore, good correspondence is observed between membrane curvature generation and the microbicidal profiles of prototypical AMPs, suggesting that curvature generation is an indicator of AMP activity. Finally, this thesis concludes with brief discussions on the possibility of other AMP design rules, as well as the presence of amphipathic domains in other curvature generating proteins which generate similar or distinct curvatures to AMPs depending on their structural motifs.

To my parents

Acknowledgments

This work is the product of many contributors who I wish to thank and acknowledge.

I thank my adviser and mentor, Gerard C. L. Wong, who initiated this research project. He gave me the right amount of independence to pursue research directions which I felt were interesting and, at the same time, provided me with the support and guidance I needed to not get lost. In my opinion, striking the balance between these things is essential to being a good mentor, and it is not easy. Some of my fondest memories of graduate school are from our Monday morning meetings, where we discussed the data and developed our model of how AMPs work. Through this process I learned how incredibly enjoyable it is to figure things out. I will always be grateful.

I also thank all the Wong group members I have overlapped with throughout the years, many whom have become good friends and collaborators, in particular: Abhijit Mishra, Ghee Hwee Lai, Robert Coridan, Lori Sanders, Lihua Yang, Kun Zhao, Fan Jin, Max Gibiansky, Scott Slimmer, Vernita Gordon, Kirsten Purdy, and John Butler. The discussions I have had with them about research have benefited my work and the way I think about science in general. Additionally, much of my data was collected at synchrotron sources. Synchrotron runs require a great deal of cooperation and support, and I thank the Wong group members who attended synchrotron runs with me for all their assistance and good company.

I thank all the undergraduate researchers especially David Kuo, Eveyln Huang, Daria Zelasko, and Matt Davis for their contributions. Each of them went above the call of duty, and I have been consistently impressed with their insights and development as young scientists. I hope that they have learned as much from working with me as I have from

teaching them.

I thank our collaborators, notably Dr. Andre Ouellette, Dr. Michael Selsted, and Kenneth Tai. Gaining the enthusiasm of immunologists went a long way toward convincing me that my research is interesting to those outside the realm of physics. While I enjoy working on basic science, it is nice to think that the results have some practical applications.

Finally, I want to thank several professors who I have worked with in the past. Both Dr. James R. Doyle (at Macalester College) and Dr. Paul Ratteron (then at SUNY Stony Brook, now at Universite Lille) were important early mentors in my scientific career and influenced my decision to pursue a doctoral degree in physics.

I acknowledge the National Institutes of Health, the National Science Foundation Water-CAMPWS, and the National Science Foundation Division of Materials Research for funding this research.

Table of Contents

Chapter 1

Review of Lipid Membranes and Antimicrobial Peptides

1.1 Introduction

Cell membranes are essential in biology, since cellular life requires separation of the living material from the harsh conditions of the surrounding environment. This does not mean they form an impenetrable barrier, however. Cells must selectively exchange material such as nutrients, ions, waste products, and signal proteins with the medium [1, 2]. The selective barrier function of membranes is also employed within the cell as many have a modular design [1, 2, 3]. Eukaryotic organelles such as mitochondria, golgi, vacuoles, chloroplast, ER, etc., are all surrounded by membranes [1, 2]. Compartmentalizing space allows the different modules to perform their specific tasks and functions in a highly organized setting [1, 4]. While this specialization provides better control over complex biological processes, the modules must be synchronized and they must cooperate in order to maintain proper cell operation [4]. The selective permeability of membranes as well as their relative ease of transport allows them to indirectly and directly provide communication pathways in cells [1, 4]. Therefore, membranes define the cell boundary, they help organize its structures, and they have multiple communication and regulatory roles in cells.

At first glance, the morphologies of cells are counter-intuitive. Since it is energetically unfavorable to expose the non-polar hydrocarbon interior of the bilayer to water molecules, membranes typically assemble to form closed surfaces. As a sphere is the shape which minimizes surface area for a given volume, membranes should partition space using this shape.

Indeed, vesicles are usually spherical. Furthermore, unicellular organisms might be expected to adopt spherical structure since minimization of surface area means the metabolic cost associated with producing and maintaining their plasma membrane is also minimized [5]. However, while coccus bacteria are spherical other morphologies such as bacillus 'rod-shaped' bacteria and spirillum 'spiral-shaped' bacteria are common, and eukaryotic cells display an even wider variety of membrane morphologies. There are multiple endocytic pathways, e.g. clathrin-mediated and caveolin-mediated endocytosis, macropinocytosis, phagocytosis, each of which employ many specialized, dedicated proteins as well as other proteins and unique lipid compositions in order to deform the membrane into the shapes necessary for endocytosis [6, 7]. Furthermore, the membrane structures in organelles such as the elaborate tubular networks seen in the smooth endoplasmic reticulum [8, 9] and in the inner mitochondrial membrane [10, 11, 12] exhibit dramatic, complex morphologies and topologies. By closely regulating their membrane compositions as well as exerting tight control over their membrane-associated scaffolding cells modify membranes into shapes conducive to their function.

While cell membrane elasticity has many benefits, it is also a vulnerability. Membrane curvature in a controlled manner can confer a functional advantage by providing a more efficient route to take up nutrients and expel waste in the case of endocytosis and exocytosis [6], or by increasing the membrane surface area per volume to enhance ATP production in mitochondria [13, 12]. However, excessive membrane curvature or the wrong type of membrane curvature can be destabilizing. It can lead to unwanted membrane fission events or uninhibited, direct contact between the cell interior and outside world, both of which disrupt the barrier function of the cell membrane and jeopardize the life of the cell. Since the breakdown of membrane integrity has devastating consequences, the susceptibility of cell membranes to destabilizing curvatures has not gone unnoticed.

The purpose of this thesis is to elucidate the selective mechanisms of action membrane-active antimicrobial peptides (AMPs) use to destabilize cell membranes [14, 15]. It is well

known that certain AMPs can multiplex membrane interactions with binding intracellular targets such as DNA, and some have adopted other specialized roles as modifiers of the host immune response [14, 15, 16]. However, in the same way that AMPs share a fundamental structural motif, they are cationic and hydrophobic [14], AMPs share a common ability to disrupt cell membranes. This thesis provides a detailed molecular model how AMPs destabilize membranes specifically, based upon their fundamental structural motif. Generic electrostatic and hydrophobic interactions between a cationic, amphiphilic AMP and a cell membrane lead to strong binding between the peptide and membrane and subsequent partial insertion of the peptide into the bilayer. We argue that the physical chemistry of AMPs leads to a whole taxonomy of local membrane distortions, specific combinations of which are topologically active and can lead to membrane destabilization. From lyotropic systems, examples of these curvatures include positive mean curvature seen in micelles, negative mean curvature seen in inverted hexagonal phases, and negative Gaussian (saddle-splay) curvature seen in cubic phases. Furthermore, saddle-splay curvature membrane deformations are expected to be especially disruptive since this type of curvature is topologically necessary for a number of membrane destabilizing processes.

Chapter 1 reviews the basic properties of lipids and antimicrobial peptides with an emphasis on the background information necessary to understand their interactions. Chapter 2 provides a short introduction to small angle x-ray scattering (SAXS), the experimental method used to characterize AMP-induced membrane curvature, followed by a brief summary of previous SAXS studies of systems where macromolecule-lipid membrane interactions influenced membrane curvature. Chapter 3 shows that prototypical defensins target membrane composition differences between host cells and microbes by selectively generating topologically active saddle-splay membrane curvature only in membranes with compositions characteristic of bacteria. Moreover, saddle-splay curvature generation places constraints on the cationic (arginine, lysine) and hydrophobic amino acid contents of AMPs which are consistent with trends in the amino acid compositions of 1,080 known antimicrobial peptides.

Chapter 4 investigates the correspondence between membrane curvature generation and the killing activities of α-defensins. We show that the phase behaviors of wild type and variant α-defensins track with their microbicidal profiles. Therefore, curvature generation is a good indicator of AMP activity. Chapter 5 presents a systematic study on how the functional group of arginine, guanidine, generates saddle-splay curvature in homopolymers and polymers enriched with hydrophobicity. We find that curvature generation by poly-guanidine polymers is sensitive to the spatial arrangement and coordination of the guanidinium groups, and that hydrophobicity generally enhances saddle-splay curvature generation. Chapter 6, the outlook chapter, first explores the possibility of other amino acid composition design rules in AMPs. Next we review other biological systems where the cationic and hydrophobic structural motif is used to remodel cell membranes. Finally, we highlight our recent research on a peptide with a different structural motif which generates a different type of membrane curvature.

1.2 Phospholipid Membranes

1.2.1 Properties of glycerophospholipids, the principle lipids in cell membranes

The principal structural ingredient in cell membranes is the lipid. In animal cells lipids constitute about 50% of the total mass of cell membranes [2]. A lipid is an amphipathic molecule composed of a polar headgroup attached to 'oily' hydrocarbon tails. There are three main types of membrane lipids (1) glycerophospholipids, (2) sphingolipids, and (3) sterols [4]. Glycerophospholipids are the main lipid type found in eukaryotic cell membranes, and all of the lipids used in this thesis are glycerophospholipids. The two hydroxyl groups of their glycerol-3-phosphate backbone (Figure 1.2A) are ester-linked to fatty acid tails while the phosphate group is ester-linked with a hydrophilic head group such as choline [17].

The structure of the common glycerophospholipid 1,2-Dioleoyl-sn-Glycero-3-Phosphocholine (DOPC) is illustrated in Figure 1.1.

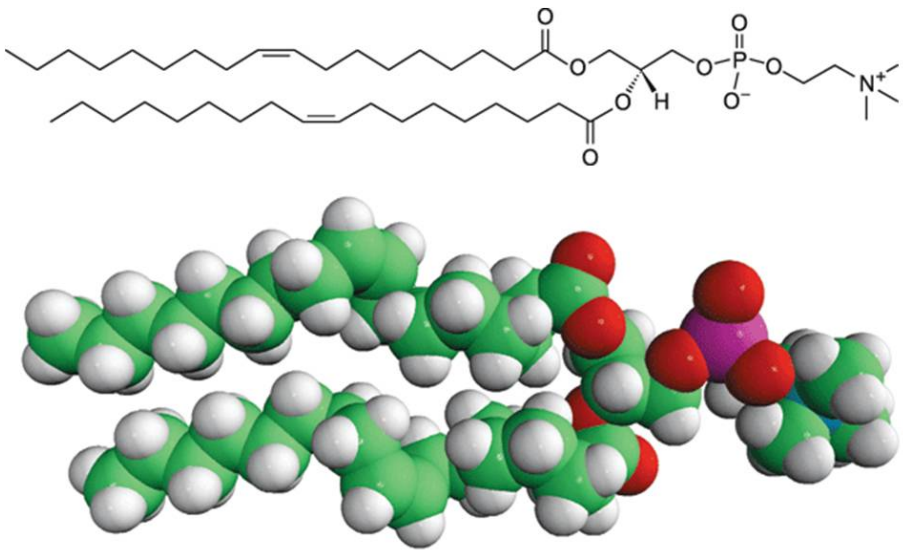

Figure 1.1: The typical glycerophospholipid DOPC. Molecular structure (top) and space-filled model (bottom). Figure adapted from images on Avanti lipids website: www.avantilipids.com

From a physical standpoint the properties of glycerophospholipids (now referred to as just lipids) are determined by their head group structures and fatty acid tails. The most commonly found head groups of cell membrane lipids are shown in Figure 1.2B. Lipids with phosphatidylcholine (PC) and phosphatidylethanolamine (PE) head groups are zwitterionic, while phosphatidylglycerol (PG), phosphatidylinositol (PI), phosphatidylserine (PS), and phosphatidic acid (PA) are anionic with net charge -1 at neutral pH [1]. In addition to their electrical properties, headgroup size is also important. For example, PC, PG, and PS headgroups are larger than the smaller PE and PA headgroups [1]. The fatty acid tails are characterized by the number of carbon atoms, the number of double bonds, and the structural differences between the two tails. For human erythroctyes typical tail lengths vary between 16 to 24 carbon atoms with the number of double bonds ranging from 1 to 6 [4].

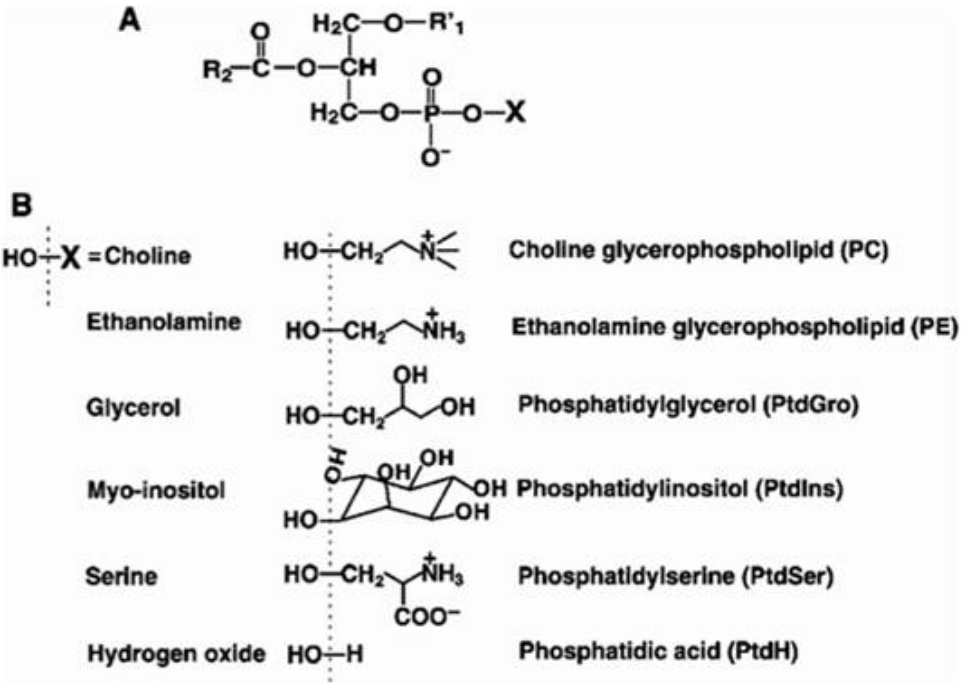

Figure 1.2: Glycerophospholipid headgroup structures. A. Glycerol-3-phosphate backbone B. The most commonly found lipid headgroups of cell membrane lipids. Image from: http://msr.dom.wustl.edu/Research/Lipidomics.htm

1.2.2 Lipids self-assemble to form membranes

A typical cell membrane is composed of lipids with zwitterionic and charged headgroups as well as membrane proteins (Figure 1.3). The structure of cell membranes is dictated by the properties of lipids. The hydrophobic effect drives the aggregation properties of lipids in water. While van der Waals interactions induce weak attraction between water and oil, the mutual attraction of water to itself is much greater, which causes segregation of water from oil [18]. When lipids are placed in water the hydrophobic effect causes them to self-assemble into a variety of different structures. The one most relevant for cells is their assembly into membranes composed of lipid bilayers, two sheets of apposing hydrophobic tail regions sandwiched between the polar headgroups. The basic bilayer structure is found in both prokaryotic and eukaryotic cells, and despite the great functional diversity of biological membranes, most are composed of a lipid bilayer [1]. This structure was first inferred

through Langmuir trough studies [19], and later directly observed by TEM studies [20] on cell membranes. More recently, x-ray and neutron diffraction experiments have determined the time-averaged transmembrane probability distribution curves of lipid components (e.g. phosphates, methylenes) for a lipid bilayer in a fluid state [21, 22]. While these results reveal there is significant out of membrane thermal motion based on the widths of the probability densities, the densities are consistent with the bilayer structure.

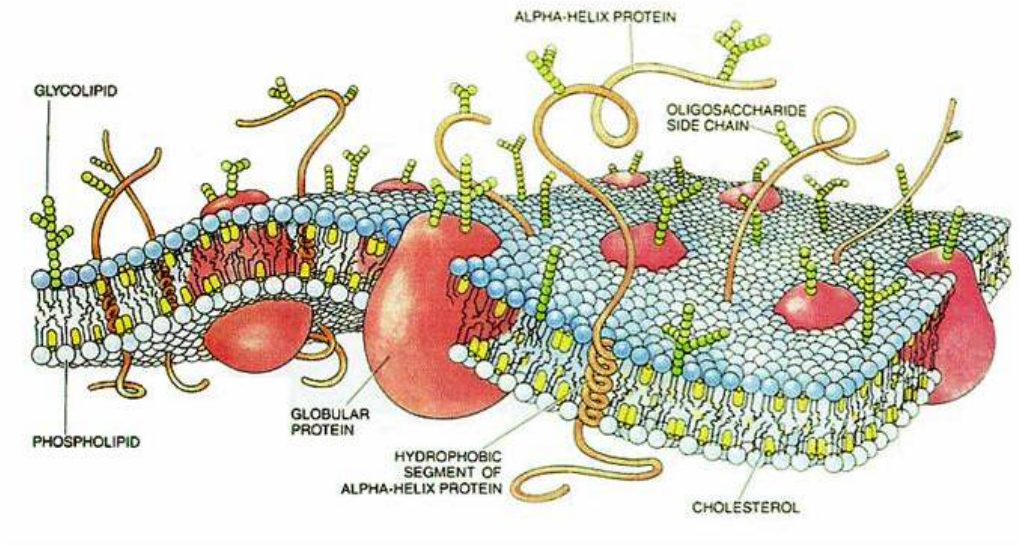

Figure 1.3: Illustration of a cell membrane. Illustration is from Wikimedia commons and was originally made by Dana Burns. Also found in [23]

Physically the cell membrane bilayer is a two-dimensional smectic A liquid crystal alloy composed of lipids and integrated proteins. This is often restated in the textbook Singer-Nicholson fluid mosaic model [24] where the bilayer has long range order but lacks short range crystalline order. Support for viewing the bilayer as a two dimensional lipid solvent containing soluble proteins comes from measurements of lateral movement of membrane constituents. Although lateral diffusion rates of phospholipid molecules vary depending on their properties and the specific composition of the membrane, typical lateral diffusion coefficients are measured to be 10^{-8} $10^{-7} cm^2/sec$ in fluid membranes [25, 26]. This indicates that for a bacterium such as E. Coli, a lipid can explore the entire plasma membrane surface area

in about a second. Similar measurements on integral membrane proteins reveal that many have comparable diffusion rates [27, 28]. However, these proteins appear to be exceptions to the norm. Most membrane proteins do not experience unrestricted lateral diffusion which is expected for a random two dimensional fluid [29]. At the simplest level this indicates there is some amount of lateral heterogeneity in membrane structure. Indeed, emerging evidence suggests the presence of microdomains - membrane regions enriched in certain types of proteins and lipids due to their preferential association with one another [30]. One example is the so-called lipid raft hypothesis, which supposes the existence of distinct domains consisting of cholesterol, sphingolipids, saturated lipids, and a variety of proteins, especially those involved in cell signalling [31, 32, 33]. Furthermore, interactions between the membrane and cell cytoskeleton often modify the lateral movements of membrane proteins and alter the distribution of both proteins and lipids in the membrane [29, 30]. Taken together these results indicate that cell membranes are not simply 2D random distributions of lipids and proteins. Instead interactions between membrane molecules as well as between these molecules and their surroundings impose a degree of lateral organization in cell membrane structure.

1.2.3 Structural properties of lipids influence the physical properties of the membrane

The fluidity of a cell membrane will depend on its composition. A cell membrane is a highly diverse composite of many different varieties of lipids and proteins. For example, erythrocytes contain over 100 different lipid types [4]. To simplify matters biophysicists typically study the phase behavior of membranes composed of a single lipid species as a function of temperature or water content (Figure 1.4A). For phosphatidylcholine (PC) lipids the typical phase progression with increasing temperature is gel ($L_{\beta'}$), rippled gel ($P_{\beta'}$), and finally liquid (L_α) phase [34]. Gel phases are characterized by their lipid hydrocarbon chains being essentially ordered and 'frozen' in the all-trans conformation, while in liquid phases

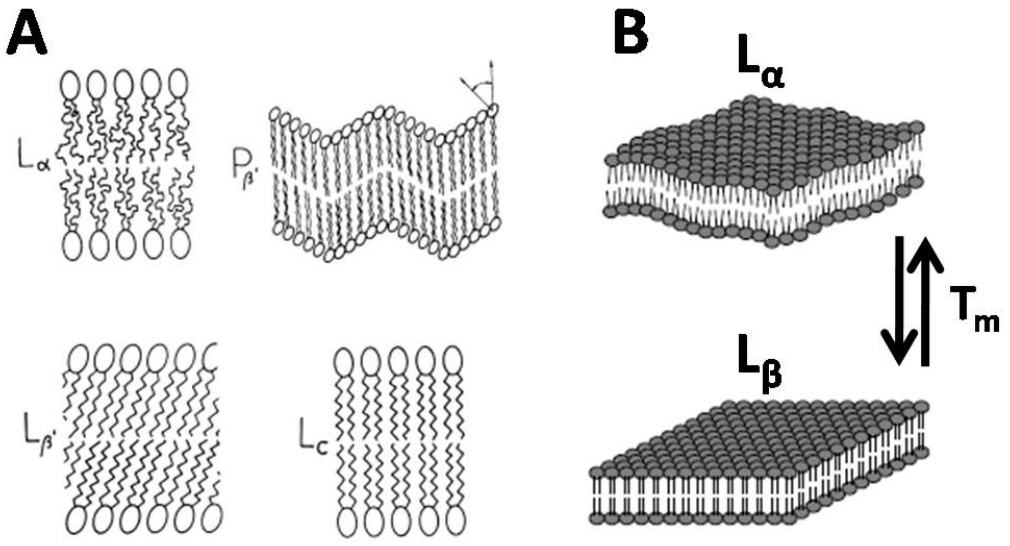

Figure 1.4: The different lamellar phases. A. Illustration of liquid disordered phase (top left), ripple phase (top right), gel phase (bottom left) and liquid ordered phase (bottom right). B. The gel-liquid phase transition at the melting temperature, T_m. Image is adapted from [34].

the chains have melted into a disordered fluid state. In the ($L_{\beta'}$) phase the hydrocarbon tails are organized in a crystal lattice structure, and are tilted in respect to the direction normal to the plane of the membrane. Since the $L_{\beta'} \rightarrow P_{\beta'}$ transition is a solid-solid transition the hydrocarbon chains remain ordered. The $P_{\beta'}$ also has crystallized hydrocarbon tails that are tilted, but with the additional remarkable feature of a rippled structure. Finally at the chain melting temperature, T_m, the chains transition from the all-trans to a disordered state and the liquid disordered L_α phase appears [34]. However, these phases are not exhaustive, especially in multicomponent membranes. For example, a liquid ordered, L_o, phase where the lipid chains are in a liquid but ordered state has been proposed for membrane microdomains such as lipid rafts which are enriched in cholesterol and phospholipids with saturated tails [31].

The gel to liquid melting temperature, T_m, is an important lipid property, since biological membranes must be in a liquid state for proper cell function (Figure 1.4B). In general, T_m

increases with chain length, and introduction of a non-saturated bond into hydrocarbon chains will tend to drastically reduce T_m [34]. For example, 18:1c9 PC (DOPC), meaning one double bond at the 9^{th} carbon of the 18 carbon tails in cis- state, has $T_m = -20°C$, saturated 16:0 PC (DPPC) has $T_m = 40°C$, and 16:1 PC has $T_m - 36°C$. T_m is also highly dependent on lipid headgroup [35]. In PE lipids 18:1c9 PE (DOPE) has $T_m = -16°C$, while the commonly used 16:0-18:1 PE (POPE) lipid has $T_m = 25°C$, right around room temperature [35]. This should be kept in mind when using POPE lipids.

1.2.4 Interactions between lipid molecules can generate membrane curvature

Liquid phases such as the L_α are the most relevant to the structure and function of biomembranes. Above T_m, lipid molecules will tend to self-assemble into the liquid lamellar phase - locally flat membranes of the basic bilayer structure. However, this is not always the case. Asymmetry between the monolayer leaflets composing the bilayer from differences in lipid and protein composition, or in solution conditions across the bilayer can influence the membrane and cause it to bend away from a flat state. Even in symmetric bilayers certain compositions and conditions can render the membrane more susceptible to being curved. If a perturbation tends to promote membrane curvature towards the aqueous solution, then transitions from the lamellar phase to non-lamellar cubic or inverted hexagonal phases become more favorable. Recently much research has focused on non-lamellar phases. A large amount of electron microscopy data supports the existence of both hexagonal and cubic phases in certain cell types [36]. Lipid membranes and genetic material such as DNA and RNA self-assemble into inverted hexagonal [37, 38] and cubic [39] complexes which have potential biotechnological applications for drug delivery and gene therapy. And lipidic cubic phases have been used to crystallize membrane proteins [40].

1.2.5 Formalisms of membrane curvature

Membrane curvature can be described using formalisms from topology. At any point on a membrane the surface will curve in a manner that depends on direction. For smooth surfaces the membrane will bend maximally in one direction and minimally in the perpendicular direction (Figure 1.5). These extremum directions of curvature are called the principal directions. By constructing circles with radii, R_{max} and R_{min}, which best fit the curvature along the principal directions the principal curvatures, $c_1 = 1/R_{max}$ and $c_2 = 1/R_{min}$, are defined at any point. The principle curvatures can be combined into two different general expressions to describe the shape of the surface:

$$H = \frac{1}{2}(c_1 + c_2) \tag{1.1}$$

$$K = c_1 c_2 \tag{1.2}$$

H is the average or mean curvature, while K is the Gaussian curvature. Flat lamellar surfaces have both zero mean curvature and zero Gaussian curvature. If the surface is rolled up into a cylindrical object the mean curvature will be non-zero, while the Gaussian curvature will remain zero. Objects such as spheres have both non-zero mean curvature and positive Gaussian curvature, since c_1 and c_2 have the same sign. If c_1 and c_2 are opposite sign the surface has negative Gaussian curvature (also called saddle-splay curvature), and locally will have the shape of a saddle. A surface with $c_1 = -c_2$ at every point is known as a minimal surface. In accordance with convention this thesis defines negative curvature as when a membrane monolayer bends away from the non-polar interior and toward solution, and positive curvature when the monolayer bends in the opposite way. For example, with this definition inverted hexagonal phases have negative mean curvature.

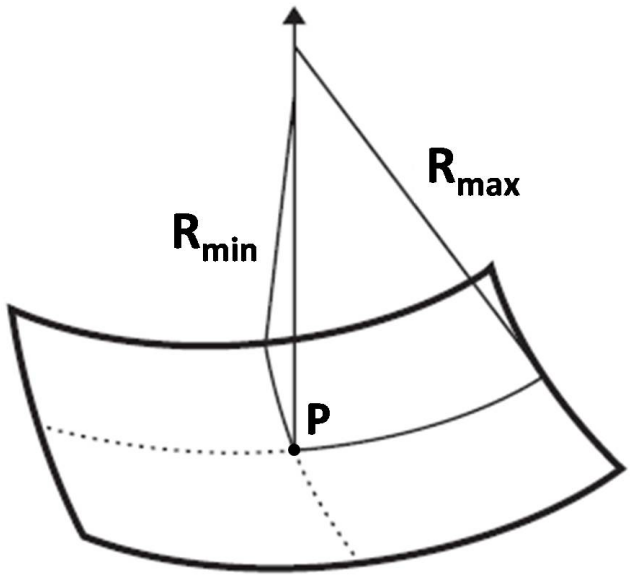

Figure 1.5: At any point, P, on a surface the principle axes of curvature, $c_1 = 1/R_{max}$ and $c_2 = 1/R_{min}$, describe the curvature at that point. Image adapted from [41].

1.2.6 Geometrical packing model of lipid molecules

Equipped with a topological description of surface curvature, the contribution of lipid molecules to membrane curvature can be discussed. One commonly used approach to understand lipid polymorphism is the "geometric packing" model developed by Israelachvili *et al* [42]. In this model the concept of an average molecular shape for a lipid molecule is introduced. Aggregated lipids experience two very different environments. In their hydrophobic interior region their tails interact mainly through attractive van der Waals and repulsive steric forces. Differently, in the hydrophilic headgroup region repulsive steric interactions, electrostatically-based interactions including those directly between ionic and zwitterionic lipid headgroups, and with head groups and aqueous phase ions, counterions, and water molecules, all contribute [42]. The directions and strengths of these forces acting throughout the lipid are subsumed into an average molecular shape which is described with a dimensionless packing parameter, S, where

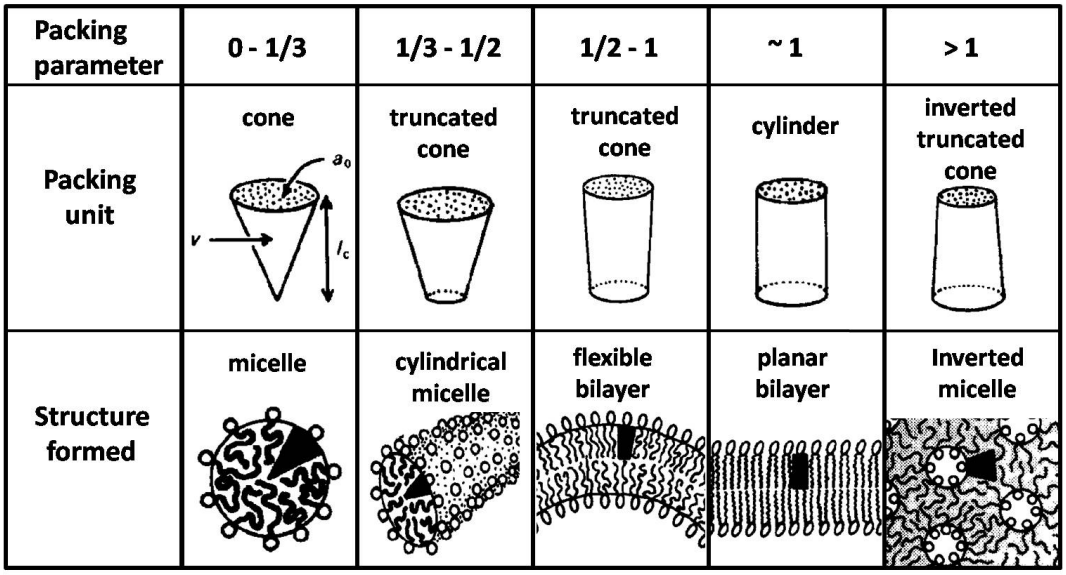

Figure 1.6: Illustration showing the relationship between the packing parameter, the geometric representation of the lipid, and the preferred aggregate. Adapted from [43].

$$S = \frac{V}{A_0 L_c} \tag{1.3}$$

Here V is the molecular volume of the hydrocarbon tails, A_0 is the optimal head group area, and L_c is the critical chain length. Israelachvili showed that lipids tended to assemble into aggregates with a geometry consistent with their packing paramters. For example, the single-chained lipid, lysophosphatidylcholine has $1/3 < S < 1/2$ and tends to form positively curved micellar structures [43]. The various packing parameter values and their corresponding lipid shapes are summarized in Figure 1.6.

Representing the forces experienced by an aggregated lipid as an average molecular shape is useful for understanding polymorphic phase behavior of lipids. Qualitative agreement is seen between the geometric packing model and certain experiments. It does have limitations, however. For example, this model cannot predict the formation of bicontinuous cubic phases, such as those found in single component membranes composed of monoolein [44]. Since cubic phases have negative Gaussian curvature the average shape of the constituent lipid molecules will be splayed in one direction and compressed in another so they cannot be described by

a single packing parameter. Furthermore, generalizing this model to multi-component lipid membranes is not straightforward, and the model cannot explain the rich phase behavior observed in these systems [45, 46]. Finally, an important property of membranes is how they respond to being deformed away from their native state. In the molecular packing picture deforming a aggregate of lipids can be visualised as producing gaps and overlapping regions between the lipid 'building blocks'. It is therefore apparent that such deformations should be energetically penalized. However, in order to translate this into a membrane curvature elasticity component to the system free energy an alternative approach first proposed by Helfrich is generally used.

1.2.7 The Helfrich approach

In this approach the curvature elastic energy per unit area of bending a membrane monolayer from its native state is [47]:

$$F_c = 2\kappa(H - c_0)^2 + \kappa_G K \tag{1.4}$$

Here c_0 is the spontaneous curvature. The bending modulus, κ, is a constant that describes the stiffness of the membrane, while the Gaussian curvature modulus, κ_G, is a constant related to how amenable the membrane is to Gaussian curvature deformations. The first term in the equation measures the energetic penalty of bending the membrane away from its spontaneous curvature, while the second term measures the energetic penalty of Gaussian curvature distortions which bend and stretch the membrane and are prerequisite to topological transitions.

The monolayer spontaneous curvature arises because the interactions in the monolayer will depend on the position in the monolayer. For example, at the hydrophilic surface the interactions between the lipid headgroups will generally produce different in-plane forces than the interactions between the lipid tails at the hydrophobic surface. If the sum of the

in-plane forces is balanced for an area which is smaller at the headgroups than at the tail ends, then the minimum-energy configuration is a monolayer which bends back toward the headgroups. In this situation the monolayer is said to have negative spontaneous curvature, i.e. $c_0 < 0$. Lipids which tend to promote this configuration are called negative spontaneous curvature lipids. They are typically illustrated with small headgroups and splayed tails, or geometrically as having a traffic cone shape. At physiological conditions the physical and chemical properties of PE and CL often render them negative spontaneous curvature lipids. Differently, the properties of PC and PG lipids typically lead to in-plane forces at their headgroup and tail regions which are balanced for equivalent areas. These lipids typically self-assemble to form flat membranes, i.e. $c_0 \approx 0$, and they are often geometrically represented as having cylindrical shape.

Another way to understand this is by examining the lateral stress, t(z), as a function of the distance, z, through a lipid monolayer. A typical lateral stress profile is depicted in Figure 1.7A. At the interface the hydrophobic effect acts to minimize the amount of contact between the surrounding water molecules and hydrocarbon tails. This produces an interfacial pressure which pushes the lipid molecules together in the bilayer. Offsetting the attraction are repulsive pressures due to steric interactions between the hydrocarbon chains and the steric, electrostatic, and hydration interactions between headgroups. The equilibrium area per lipid throughout the monolayer is achieved when the integral of the lateral stress across the lipid monolayer, $\int t(z)\,dz$, is zero. Since the first moment of the lateral stress profile, $\int zt(z)\,dz$, is proportional to c_0, lipid lateral stress profiles from inter-lipid interactions affect monolayer curvature [48].

It should be noted that if two monolayers with identical spontaneous curvatures combine to produce a membrane bilayer the spontaneous curvature of the bilayer must be zero to avoid producing energetically costly voids (Figure 1.7B). Bilayer spontaneous curvature arises from asymmetry between the monolayer leaflets. However, the consequences of forming a lamellar phase membrane with $c_0 \neq 0$ monolayer leaflets is stored elastic energy. As we shall see, for

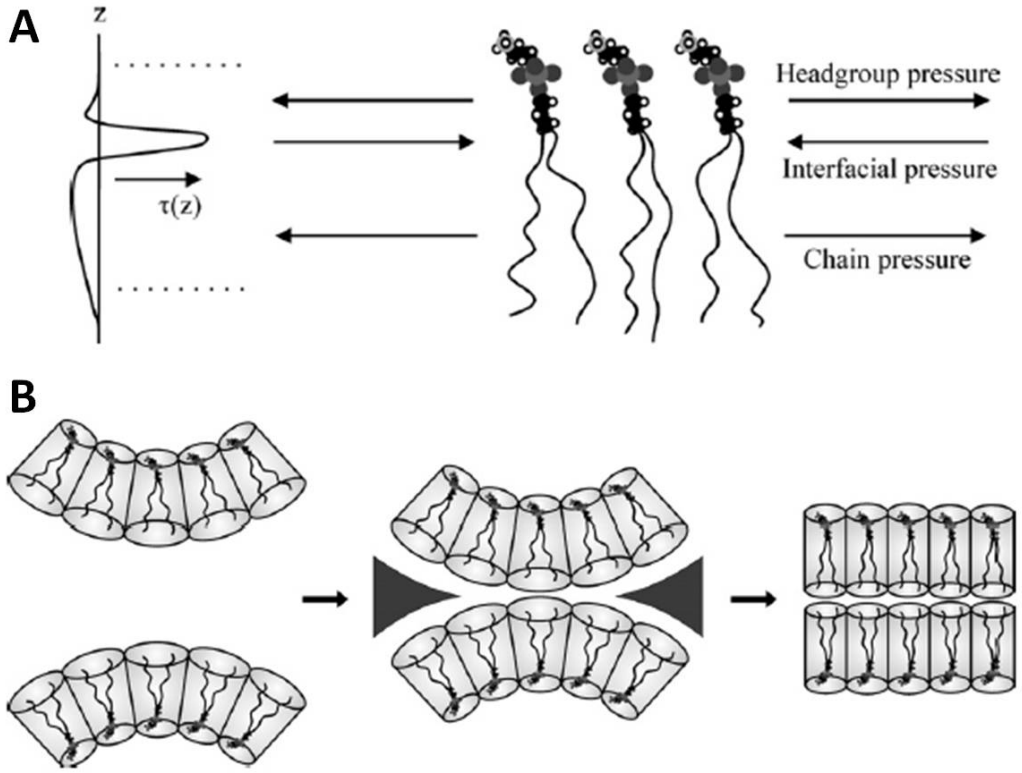

Figure 1.7: Lipid lateral stress, *t(z)*, profiles affect membrane curvature. A. Schematic of the lateral stress through a lipid monolayer. At equilibrium the integral of the lateral stress is zero. The first and second moments of the lateral stress are equal to $-\kappa c_0$ and κ_G, respectively [49]. Therefore, *t(z)* determines the curvature properties of a monolayer. B. Joining monolayers with non-zero spontaneous curvature produces a bilayer with zero curvature provided there is no asymmetry between monolayers. Adapted from [41].

antimicrobial peptides the presence of greater amounts of negative spontaneous curvature lipids in bacterial membranes compared with eukaryotic membranes is important for their selective activity.

1.2.8 Relationship between monolayer and bilayer curvature elastic parameters, and their influence on topological transitions

For a symmetric bilayer the bilayer spontaneous curvature, c_0^b, bending modulus, κ^b, and Gaussian modulus, κ_G^b, are related to the monolayer elastic parameters through the following expressions [50]:

$$c_0^b = 0 \tag{1.5a}$$

$$\kappa^b = 2\kappa \tag{1.5b}$$

$$\kappa_G^b = 2(\kappa_G - 4\kappa c_0 d) \tag{1.5c}$$

The first expression simply restates that the membrane is symmetric. The expression for κ^b explains that the energy required to bend two monolayers is twice the amount needed to bend one. The third expression is more complicated, as κ_G^b is not simply twice the monolayer Gaussian modulus, but it also depends on κ, c_0, and d, the distance from the middle of the bilayer to the monolayer pivot point. The bilayer Gaussian curvature modulus is related to the resistance of the membrane to topological transitions. This is a consequence of the Gauss-Bonnet theorem, which can be used to show that the integral of Gaussian curvature over a closed surface with genus, g, is [50]

$$\int K \, dA \; = 4\pi(1 - g) \tag{1.6}$$

The genus is zero, $g = 0$, for a sphere. For a torus, $g = 1$, which is topologically equivalent to a sphere with a 'handle'. For each new handle the genus increases by one. As expected, spheres have $K = 4\pi$, total Gaussian curvature, while torus has $K = 0$, and so on with the formation of each handle imparting a change of -4π Gaussian curvature. Infinite periodic minimal surfaces such as the Pn3m (D), Im3m (P), and Ia3d (G) cubic phases (Figure 1.8) have infinite genus and are therefore rich in negative Gaussian curvature. A simple way to understand the connection between κ_G^b and topological transitions is to examine the lamellar to cubic phase transition. As stated before lamellar phases have $H = 0$, and $K = 0$, whereas cubic phases have $H = 0$, while $K < 0$. Therefore the difference in curvature energy between the two phases, ΔF, comes solely from their differing Gaussian curvatures [50]:

$$\Delta F_c = F_{cubic} - F_{lamellar} = \kappa_G^b \oint K \, dA = \kappa_G^b \langle K \rangle A \tag{1.7}$$

where $\langle K \rangle$ (< 0) is the average negative Gaussian curvature over the membrane area, A. So cubic phase formation is energetically favorable when $\kappa_G^b > 0$. Similarly, the formation of a toroidal pore in an intact lamellar membrane, produces $\Delta K = -4\pi$ change in Gaussian curvature, with a $\Delta E = -4\pi\kappa_G^b$ energy change from the Gaussian curvature contribution to the curvature energy [51]. (Since there is no guarantee that the toroidal pore interior will be a minimal surface, the mean curvature contribution to the energy must also be taken into account in order to get the full ΔF_c). However, the point is membranes with positive κ_G^b will produce porous phases, and those with barely negative κ_G^b will be more vulnerable to $\Delta K < 0$ topological transitions. An interesting consequence of $\kappa_G^b \propto -c_0$ is that membranes enriched in $c_0 < 0$ lipids should be more susceptible to pore formation.

1.2.9 Basic properties of cubic phases

Much of the work in this thesis is centered around bicontinuous cubic phases (Q_{II}) (Fig 1.8) and their underlying negative Gaussian surface curvature. Therefore, a brief description of

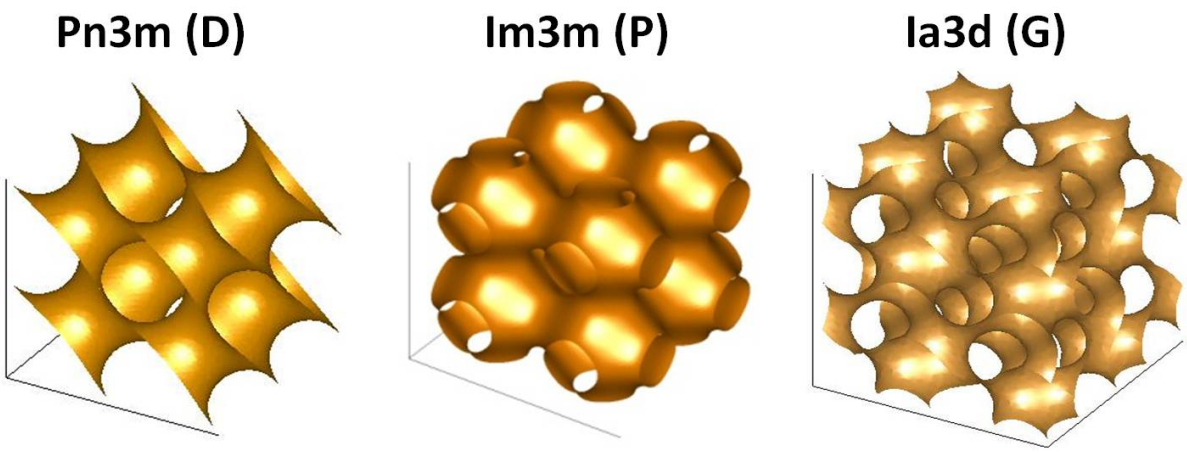

Figure 1.8: The three most commonly observed bicontinuous cubic phases in lyotropic systems. The Pn3m 'double-diamond' phase (left), the Im3m 'plumber's nightmare' phase (middle), and the Ia3d 'gyroid' phase (right) Images rendered using Matlab m-files created by the Gruner lab: `bigbro.biophys.cornell.edu/~toombes/Software/Minimal_Surfaces/`

them is necessary. Q_{II} phases display three dimensional periodicity, where their minimal surface divides space into two inter-linked but not intersecting regions. Physically, a lipidic cubic phase can be visualised where the membrane bilayer is 'draped' over the minimal surface, such that the lipid head groups remain hydrated by the two water channels. The center of the bilayer, where the hydrocarbon tail ends meet, traces the minimal surface.

While $H = 0$ along the minimal surface, this is not true for surfaces parallel to the minimal surface within the bilayer. For example, moving a distance ξ from the mid-bilayer minimal surface to a parallel surface, changes the principal curvatures from, $c_1 = -c_2 = 1/R$, to $c_1^\xi = 1/(R+\xi)$ and $c_2^\xi = -1/(R-\xi)$ on the parallel surface. The relations for surfaces parallel to the minimal surface are [41]

$$H^\xi = \frac{K\xi}{1+K\xi^2} \tag{1.8a}$$

$$K^\xi = \frac{K}{1+K\xi^2} \tag{1.8b}$$

$$dA^\xi = dA[1+K\xi^2] \tag{1.8c}$$

where dA is the area element of the surface. Since cubic phases have $K < 0$, the relations show that on the parallel surface both H^ξ and K^ξ are more negative than on the minimal surface. In fact while $H = 0$ on the minimal surface, on any parallel surface $H^\xi < 0$. Therefore, just like inverted hexagonal phases which have $H < 0$, cubic phases with $H^\xi \leq 0$ are often referred to as inverted phases.

So far no distinctions have been made between different bicontinuous cubic phases. While many cubic minimal surfaces exist [52] only the D, P, and G phases have been experimentally observed in lyotropic systems. By modelling the distribution of Gaussian curvature over 7 different bicontinuous cubic phases, Schwarz and Gompper [53] showed that the D, P, and G cubics have smaller widths in their Gaussian curvature distributions. Therefore, these three cubic phases experience smaller frustration which leads to their enhanced stability. With respect to their relationship with each other the D, P, and G phases are related by a Bonnet transformation, a one-to-one surface mapping which preserves the distribution of Gaussian curvature at all points on the surface [54]. Two consequences of the Bonnet transformation are: For the correctly chosen ratio of lattice parameters the three minimal surfaces will have same area per unit cell, and their curvature energy will be degenerate. The average Gaussian curvature, $\langle K \rangle$, for a minimal surface with Euler characteristic, χ, and surface area of a unit cell with sides of length 1, A_0, is [55]

$$\langle K \rangle = \frac{\int\limits_{unitcell} K \, dA}{\int\limits_{unitcell} dA} = \frac{2\pi\chi}{a^2 A_0} \tag{1.9}$$

where a is the lattice parameter of the cubic phase. The parameters for the three phases are shown in Figure 1.9. By equating $\langle K \rangle$ for the D, P, and G surfaces we find: $a_P/a_D = 1.279$ and $a_G/a_D = 1.578$ [55]. Coexisting cubic phases with lattice parameters at these 'Bonnet ratios' are often observed in lipid-water systems [41]. Comparison of the D, P, and G lattice parameters at Bonnet ratios reveals that for a given average Gaussian curvature, $\langle K \rangle$, the Pn3m has the smallest lattice parameter followed by the Im3m and then the Ia3d. Lastly,

Minimal Surface	Cubic Phase	χ	θ	A_0	a/a_{Pn3m}
D	Pn3m	-2	0	1.919	1
P	Im3m	-4	$\pi/2$	2.345	1.279
G	Ia3d	-8	0.66349	3.091	1.578

Figure 1.9: Characteristics of the 'genus-3' bicontinuous cubic phases

the morphologies of the three cubics differ in their porosity, or the number of water channels that split off at each junction. The Im3m 'plumber's nightmare' is the most porous with six vertices, while the Pn3m 'double-diamond' and Ia3d 'gyroid' phases have four and three vertices, respectively.

1.3 Wet Electrostatics

Almost all biomembranes display electric charge. The anionic lipid phosphatidylserine accounts for 10-20% of the lipid content in erythrocyte plasma membranes [56]. Bacteria cell membranes typically contain more negatively charged lipids. And in some cases, for example, Staphylococcus aureus whose cell membrane contains roughly a 50/50 mixture of phosphatidylglycerol and cardiolipin, essentially the entire membrane is composed of lipids with electronegative headgroups [57, 58]. Furthermore, biomembranes often contain other polyanionic molecules which affect their surface charge, such as heparin sulfate cell surface receptors [59, 60] in eukaryotic cells and lipopolysaccarides and lipoteichoic acids which decorate the surfaces of Gram-negative and Gram-positive bacteria [16], respectively. The presence of electric charge affects many of the physical characteristics of membranes. Structural properties including membrane rigidity, phase transition temperatures, and dynamics depend on membrane charge density [61]. Furthermore, membrane charge plays an impor-

tant role in the interactions between biomembranes and other molecules. This thesis is primarily concerned with peptide-membrane interactions. The purpose of this section is to provide a brief overview of the field of wet electrostatics and discuss its concepts within the context of anionic cell membranes and cationic antimicrobial peptides. The treatment below has been adapted from discussions of the Poisson-Boltzmann equation and Debye-Hückel theory in references [3, 62, 61].

When a macromolecule is dissolved in solution it often releases ions into the suspension and becomes charged. The charged regions on the macromolecule will attract oppositely charged counterions in the suspension, which localize around the charged macromolecule. The resulting 'cloud' of counterions forms a electrical double layer, perturbing or 'screening' the electrostatic potential of the macromolecule. At physiological conditions the large dielectric constant of water along with the electrical double layer of ions and dissociated salts strongly screen electric fields produced by macromolecules like AMPs and assemblies like lipid membranes. It is this electrical double layer that influences how a macromolecule interacts with its environment. Therefore, understanding the basic structure and properties of the double layer is important.

1.3.1 The Poisson-Boltzmann equation & Debye-Hückel theory, part I

Consider a charged flat surface (placed at $x = 0$) with negative surface charge density $-\sigma$, that is hydrated by an ionic solution with dielectric constant ϵ in the $x > 0$ region. At any point in the solution the (mean field) electrostatic potential, $\psi(z)$, is related to the charge distribution, $\rho(z)$, through the Poisson equation

$$\nabla^2\psi = \frac{\rho}{\epsilon} \tag{1.10}$$

For simplicity we assume there are only two types of mobile charges in the solution,

counterions and co-ions. The charge density is therefore: $\rho = ez_+n_+ + ez_-n_-$, where n_+ (n_-) are the number densities of the counterions (co-ions) and z_+ (z_-) are their valences. Within the mean field approximation the electrostatic potential energy of a counterion at position x is $e\psi(x)$. Since this allows the ions to be treated as acting independently of each other, the density of the ith ion is given by the Boltzmann distribution

$$n_i = n_0^i e^{\frac{-e\psi(x)}{k_b T}} \tag{1.11}$$

where e is the electric charge, k_B is the Boltzmann constant, T is the temperature, and n_0^i is a constant. To get a general idea of the size of the double layer we first assume the surface is submerged in pure water. With no additional electrolyte the only ions present are counterions, so $n_- = 0$, and we define $n_+ \equiv n$, and $n_0^+ \equiv n_0$ as a reference density where $\psi = 0$. To simplify matters we define a dimensionless rescaled potential $\bar{\psi}(x) \equiv e\psi(x)/k_B T$. Combining expressions (1.10) and (1.11) gives the Poisson-Boltzmann equation

$$\frac{d^2\bar{\psi}}{dx^2} = -4\pi l_B n_0 e^{-\bar{\psi}} \tag{1.12}$$

where

$$l_B \equiv \frac{e^2}{4\pi\epsilon k_B T} \tag{1.13}$$

is the Bjerrum length in water. The Bjerrum length is the distance between two like-charge ions where their electrostatic interaction energy equals the thermal energy $k_B T$. For monovalent ions in water at room temperature, $l_B = 0.71nm$. Generally speaking, Poisson-Boltzmann theory is a good approximation for most physiological conditions, especially in systems that contain mostly monovalent ions and surfaces with charge densities that are not too large.

The Poisson-Boltzmann equation is a non-linear differential equation. Typically closed

form solutions of these equations are not known, and the standard procedure is to either linearize them to get an approximate solution, or to solve them numerically. However, the geometry of an infinite flat surface renders this problem tractable. To solve a second-order differential equation with unspecified n_0 requires three boundary conditions. Setting $\psi(0) = 0$ turns n_0 into the concentration of counterions at the surface. Since the electric field should approach zero at distances far from the surface, $d\psi/dx \to 0$ out there. Finally, the surface form of the Gauss law gives

$$\frac{d\bar{\psi}}{dx}\Big|_{surface} = 4\pi l_B \frac{\sigma}{e} \tag{1.14}$$

Applying these conditions and integrating the Poisson-Boltzmann gives the potential, $\psi(x)$, in the aqueous solution ($x > 0$), and $n(x)$ is obtained from $\psi(x)$ via the Poisson equation. They are

$$\psi(x) = 2\frac{k_B T}{e} \ln(1 + x/b) \tag{1.15a}$$

$$n(x) = \frac{1}{2\pi l_B} \frac{1}{(x+b)^2} \tag{1.15b}$$

$$\text{where} \quad b = (2\pi l_B \sigma/e)^{-1} \tag{1.15c}$$

The variable, b, is the Gouy-Chapman length, and it is a rough measure of the thickness of the double layer of counterions that forms around the charged sheet. Rewriting the Gouy-Chapman length as $b = (\frac{2\epsilon}{e\sigma})k_B T$ allows us to see another interesting interpretation. An isolated counterion next to the charged surface, which has electic field $-\sigma/2\epsilon$, can be displaced a distance b by doing $k_B T$ amount of work. In other words the counterions 'borrow' some thermal energy from their environment in order to move approximately a distance b away from the surface. This occurs because the entropic gain is greater than the electrostatic penalty, which leads to a overall reduction of their free energy.

Another way to think about this k_BT energy per counterion is to picture the double layer as a planar sheet of charge held at a distance b from the surface. In this model we have a parallel plate capacitor which stores electrostatic energy $E = Q_{tot}^2/2C$, where over an area A on the capacitor $Q_{tot} = \sigma A$. The capacitance, C, of a parallel plate capacitor is $C = \epsilon A/b$. Combining the previous three equations gives an estimate of the amount of stored electrostatic energy per unit area for a charged surface in water: $E \approx k_BT(\sigma/e)$. Again a counterion borrows around k_BT energy from the environment. Recall that the cell membrane of Staphylococcus aureus is entirely composed of anionic lipids. This bacterium is roughly circular with a diameter of $1\mu m$. We approximate the area of a lipid as $0.7nm^2$ so $|\sigma/e| = 0.7nm^{-2}$. When submerged in water Staphylococcus aureus carries a stored free energy of $\approx 4\pi(0.5\mu m)^2 \times (0.7/nm^2)k_BT \approx 2e6k_BT$ in its plasma membrane.

1.3.2 The Poisson-Boltzmann equation & Debye-Hückel theory, part II

The purpose of the last subsection was to illustrate two ideas: Screening reduces the range of electrostatic interactions to roughly the Gouy-Chapman length, but this does not mean that electrostatic interactions are weak. However, the above results were for a charged surface submerged in pure water. Cells live in electrolyte solutions, so in biological conditions the bulk concentrations of both counterions and co-ions are non-zero. How does the presence of salt matter? Approximating the bulk electrolyte as a reservoir of monovalent ions such as NaCl the Poisson-Boltzmann equation becomes:

$$\nabla^2\bar{\psi} = \lambda_D^{-2}\sinh(\bar{\psi}) \tag{1.16}$$

Here λ_D, or the Debye screening length, is defined as

$$\lambda_D \equiv (\sum_i 4\pi l_B z_i n_i^\infty)^{-1/2} \tag{1.17a}$$

$$\lambda_D = (8\pi l_B n^\infty)^{-1/2} \qquad \text{For 1:1 salt like NaCl} \tag{1.17b}$$

where n_i^∞ is the bulk concentration of the ith ion. Under physiological solution conditions typical Debye lengths are less than a nanometer. For example for a 1:1 electrolyte such as NaCl at 100mM the screening length is 9.6 $\mathring{A}$.

The added salt Poisson-Boltzmann equation also can be solved in closed form. Using the same surface boundary condition (1.14), in addition to $\psi(x) \to 0$, & $\frac{d\psi}{dx} \to 0$ as $x \to \infty$ it can be shown that the resulting potential is

$$\psi(x) = -\frac{2k_BT}{e} \ln \frac{1+\gamma e^{-x/\lambda_D}}{1-\gamma e^{-x/\lambda_D}} \tag{1.18}$$

where

$$\gamma = \frac{b}{\lambda_D}(\sqrt{1+(\lambda_D/b)^2} - 1) \tag{1.19}$$

The surface potential $\psi_s = \psi(0)$ is

$$\psi_s = -\frac{4k_BT}{e} \operatorname{arctanh}(\gamma) \tag{1.20}$$

Therefore, while the surface potential was determined entirely by its charge density for a surface immersed in water, the potential of a surface in electrolyte is also affected by the bulk salt concentration. In the limit of high salt concentration (small λ_D) the surface potential becomes very small, and the electrostatic potential can be approximated as

$$\psi(x) = \psi_s e^{-x/\lambda_D} = -\frac{\sigma\lambda_D}{\epsilon} e^{-x/\lambda_D} \tag{1.21}$$

Under high salt the electrostatic properties of the surface are strongly screened and decay exponentially. The double layer of ions surrounding the surface is characterized by a thickness λ_D, typically around a nanometer at physiological solution conditions. Unlike the double layer in the no-salt case which had constant thickness, b, adding salt shrinks the Debye screening length. Therefore, increasing the concentration of salt decreases the size of the double layer. Furthermore, in the no-salt case as the surface charge density is reduced the Gouy-Chapman layer, b, grows without limit. This does not happen under the presence of added salt, it can only grow until it reaches the Debye screening length [63].

Why does the size of the double layer decrease when salt is added to the solution? Referring back to the original argument about the competition between electrostatic energy and entropy, a smaller double layer implies that counterions have less to gain entropically by distancing themselves from the surface. This makes sense because there is a non-zero concentration of counterions everywhere in solution.

Lastly is the short ranged behavior of electrostatic interactions something specific to surfaces? For charged surfaces we found that their counterions remained confined around the surface even upon infinite dilution (pure water solution). This phenomena is often referred to as counterion condensation. The counterions remain condensed within a Gouy-Chapman length of the surface. While lipid membranes are usually a (locally) flat 2D surface, many other biological macromolecules have different geometries. For example, the persistence length of double-stranded DNA is about 50nm, and cytoskeletal filaments like F-actin and microtubules have persistence lengths on the order of microns. The counterion condensation of 1D rod-like polyelectrolytes is more peculiar. Consider an isolated counterion (valence e) in the proximity of an infinite rod with radius a, and charge density ν. Approximating the polyelectrolyte as a stiff rod composed on ionized monomers of charge e, and spacing d, we write $\nu = e/d$. Releasing the counterion to a distance r away from the rod costs $\frac{e^2}{2\pi\epsilon d}\ln(r/a)$ electrostatic energy, while the entropic gain is $k_BT\ln(\frac{\pi r^2}{\pi a^2})$ [64]. Comparing electrostatic and entropic components of the free energy, we find that the charge density of

the rod determines the condensation behavior of the counterions, according to the value of the Manning parameter, ξ [64]

$$\xi \equiv \frac{e_2}{4\pi\epsilon k_B T}\frac{1}{d} = \frac{l_B}{d} \tag{1.22}$$

If $\xi < 1$ the counterions are released and fully dissociate into solution. However, for highly charged electrolytes Manning showed that the partition function for a 'condensed' ion diverges if $\xi > 1$. This implies that counterions must condense onto the rod until its surface charge density is renormalized to the point where the average spacing between charges, d equals the Bjerrum length, l_B. For example, DNA carries a large amount of negative charge. Since it has 20 phosphate groups per helical pitch of 3.41 nm, 76% of the anionic groups of DNA are neutralized by Manning condensation [65]. Moving down in dimension to 'point-like' molecules, as a consequence of their $\psi \propto 1/r$ electric potential it can be shown that upon infinite dilution all counterions are released. However, adding salt to the solution changes the entropic landscape. And in the presence of bulk electrolyte a charged macromolecule remains surrounded by an λ_D electric double layer of counterions according to Debye-Hückel theory [63].

In summary, electrostatic forces are short ranged due to the clustering of mobile ions which act to screen electrostatic fields to the range of around a nanometer. However, clustering ions reduces their accessible volume. Therefore, compared to the 'free ion' configuration, the electrical double layer configuration has reduced entropy. And built into the reduced entropy of ion configurations around charged macromolecules is the potential for strong inter-macromolecular interactions. In the case of antimicrobial peptide-lipid membrane interactions, overlap of the electronic double layers of a cationic AMP and an anionic membrane allows their opposite charge distributions to replace condensed counterions. The counterions are released from their bound state and into solution for a large entropic gain, which generates a strong attraction between the polymer and membrane.

1.4 Antimicrobial Peptides

The emergence of bacterial resistance to current antibiotic strategies is a global health problem. For example, methicillin-resistant [66] Staphylococcus aureus (MRSA) and Staphylococcus aureus with complete resistance to vancomycin [67], often referred to as the drug of last resort, first appeared in U.S. hospitals in 2002. A report by the WHO in 2008 showed that the number of cases of extensively drug resistant Mycobacterium tuberculosis [68] had reached the highest levels ever recorded. Rational treatment approaches such as improvements in the use of antimicrobials and precautions to reduce the transmission of resistant bacterial strains help slow the rate of emerging resistance. The use of antibiotics itself, however, exerts a strong selective pressure in favor of drug-resistant bacteria. Whats worse, the pharmacological development of antimicrobials tends to be expensive and slow, and present methods are not well adapted to the challenge of rapidly evolving bacterial resistance. Therefore, there is a significant need to have design rules that rationally guide the synthesis of new antimicrobials by reducing the large parameter space of molecular compositions.

Cationic antimicrobial peptides (AMP) are present in virtually every multi-cellular organism, and comprise an important part of the innate host defense [14, 15, 69, 70, 16, 71]. Collectively, AMPs display broad spectrum antimicrobial activity and have a rapid mechanism of action [14, 15, 16]. Despite being one of the oldest components of the host immune system, bacteria have not been able to evolve resistance and AMPs remain effective antimicrobial agents [14, 16]. Here we review the field of antimicrobial peptides, primarily, within the context of peptide-membrane interactions.

1.4.1 Structural features of natural and synthetic AMPs

To date over 1000 AMPs have been discovered. Despite the enormous structural diversity of AMPs most share a few broad structural features. AMPs are short (< 50 amino acids), have net positive charge (+2 to +9), and contain a significant proportion of hydrophobic amino

acids (> 30%) [14, 15, 69, 70, 16, 71]. Generally their cationic and hydrophobic residues spatially partition into discrete clusters to form an amphipathic secondary structure (Figure 1.11). AMPs are often classified by these folded structures (Figure 1.10). One subgroup consists of linear peptides such as magainins [72] from frogs, and LL-37 cathelicidins [73] from humans. These peptides adopt alpha helical structures when they partition into a membrane interface which segregates their polar and hydrophobic residues on opposite faces of the helix (Figure 1.10A). Another subgroup of AMPs includes peptides that consist of beta sheet structures stabilized by disulfide bonds from cysteine residues, such as protegrins [74] from pig, and defensins [75, 76, 77] (Figure 1.10B-D). Mammalian defensins include alpha defensins such as cryptdins [78] from mouse, beta defensins like the human beta defensins [76] and theta defensins [79] which are found only in old world monkeys (Figure 1.10B&C). A third subgroup is categorized by extended linear peptides with sequences dominated by a few amino acids, like the tryptophan-rich indolicidin [80] from cattle, and the arginine and proline-rich PR-39 [81] from pig (Figure 1.10E). Lastly there are peptides derived from proteolysis of proteins such as buforin II [82] from histone 2A which is expressed in frog, and lactoferricin B [83] from gastric pepsin digestion of bovine lactoferrin.

Based on the central hypothesis that the activity of many AMPs may depend more on their fundamental cationic and amphipathic properties (Figure 1.11) than on their precise amino acid sequences and secondary structures, a variety of synthetic antimicrobials have been designed using different chemistries. One method is to modify existing AMP sequences to maximize antimicrobial activity while also minimizing hemolytic activity to optimize therapeutic potential. Examples of synthetic AMPs which have been developed by modifying natural versions include MS-78 (pexiganan) [85], a variant of the AMP magainin from frogs, iseganan [86], a variant of protegrin from pigs, and omiganan [87], a cattle indolicidin variant. By using the positively charged amphipathic features as templates, synthetic AMP analogues have been constructed. These analogues include model antimicrobials based upon mimicking the peptide primary structure (peptidomimetics), and ones that use non-peptidic compounds

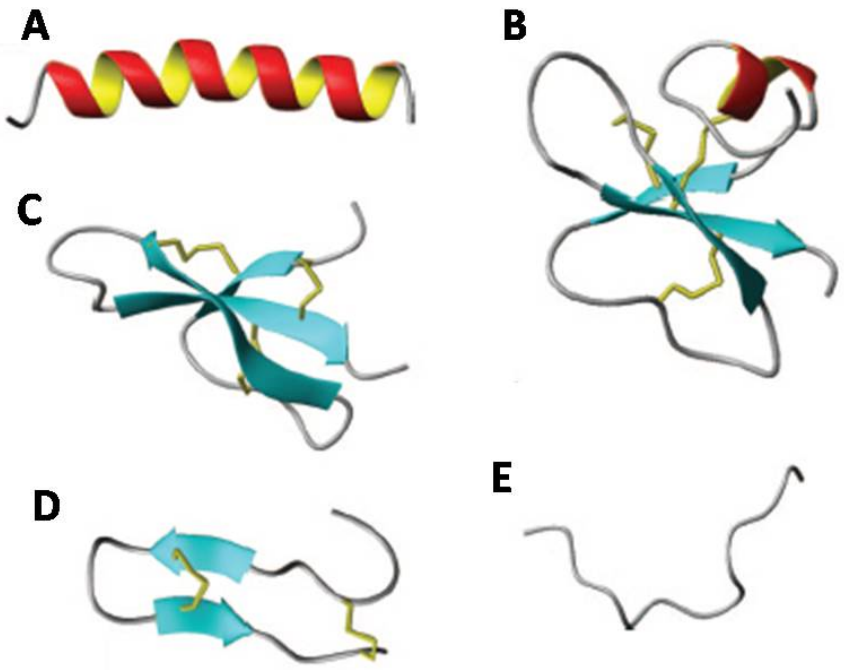

Figure 1.10: Common secondary structures of antimicrobial peptides. A. α-helical magainin-2 from frog. β-sheet AMPs: B. human β-defensin-2, C. rabbit kidney α-defensin-1 and D. polyphemusin from Japanese horseshoe crab. E. Linear bovine indolicidin. Disulfide bonds are colored yellow. Molecules were prepared with graphic program MolMol 2K.1. Adapted from ref [84]

.

[88, 89]. Peptidomimetic antimicrobials have been made using β-peptides [90, 91, 92] and peptoids [93]. These peptides folded into amphipathic structures and demonstrated potent *in vitro* anti-bacterial activity. Furthermore, unlike the α-peptide backbone of natural AMPs, both β-peptides and peptoids offer the additional advantage of being resistant to proteases. Non-peptidic compounds include facially amphipathic acrylamide polymers [94], phenylene ethynylene molecules [95], polymethacrylate derivatives [96], and polynorborene derivatives [97], which all displayed potent selective activity against Gram-positive and Gram-negative bacteria. Since these synthetic antimicrobials are also cationic and amphipathic, it is believed their mechanism of activity is similar to AMPs. Interestingly, random copolymers composed of amphiphilic polymethacrylate derivatives showed activity comparable to natural antimicrobials with low hemolytic activity [96]. And disulfide null analogues of α-defensin Crp4 [98] and human β-defensin-3 [99] showed in vitro bactericidal activities equal to or greater than the wild type peptides. Since removal of the tridisulfide array rendered Crp4 extensively susceptible to proteolysis, it was concluded that the purpose of disulfide arrangement in Crp4 is not to confer bactericidal activity but to offer protection against degradation [98, 100]. These last results suggest that prearranged amphiphilic structures are not necessarily required for antimicrobial activity.

1.4.2 Proposed mechanisms of selectivity

A general mechanism of AMP activity is destabilization of the physical integrity of cell plasma membranes leading to depolarization, leakage, and eventual cell death [14, 84]. Support for this comes from studies showing that AMPs composed of D amino acids showed identical antibacterial and hemolytic activities to their all-L natural versions, indicating specific interactions with chiral membrane receptors and enzymes are not responsible for activity [101, 102, 103, 101]. Therefore, membrane disruption is thought to be a consequence of non-specific interactions between the AMP and the cell membrane. Evidence that AMPs can directly target lipids, the principal components in cell membranes, comes from an extensive

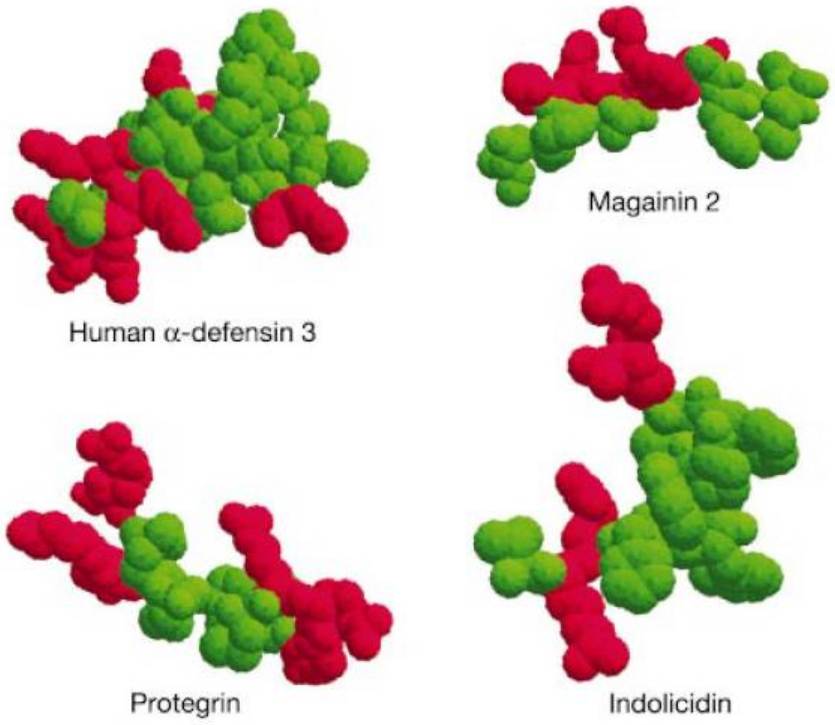

Figure 1.11: The fundamental structural motif of antimicrobial peptides. Partitioning of cationic amino acids (red) and hydrophobic amino acids (green) into distinct regions to produce an amphipathic molecule. Adopted from ref [14].

number of *in vitro* studies using distinct techniques including X-ray and neutron scattering, NMR, AFM, Raman spectroscopy, circular dicroism, differential scanning calorimetry, and flourescence experiments [15] (and references therein). These studies have established that AMPs strongly interact with and alter the intrinsic structure of lipid bilayers. Furthermore, numerous leakage assays on liposomes have demonstrated that AMPs can permeabilize lipid bilayers [15].

AMP selectivity is thought to be a consequence of compositional differences between bacterial cell membranes and the membranes of the host cells. Microbial cell surfaces are decorated with polyanionic molecules like lipopolysaccarides in Gram-negative bacteria, and lipoteichoic acids in Gram-positive bacteria [16]. Additionally, the outer leaflet of bacterial plasma membranes contains large amounts of anionic lipids such as those with phosphatidylglycerol (PG) and diphosphatidylglycerol (dPG, also called cardiolipin which is abbreviated as CL) head groups. For example, the membranes of the Gram positive bacteria S. aureus, and S. pneumoniae (Figure 1.12A) are composed primarly of PG and CL lipids. Phosphatidylethanolamine (PE) is the principle zwitterionic phospholipid found in Gram negative bacteria (Figure 1.12A) such as E. coli, P. aeruginosa, S. typhimurium and in the Gram positive genus Bacillus [57]. The lipid compositions of animal cell membranes (Figure 1.12B) are different from bacteria plasma membranes in at least three ways: First, they are more heavily populated by lipids with neutral zwitterionic head groups such as phosphatidylcholine (PC) and sphingomyelin (SM) [14, 56]. Second, their lipid compositions are asymmetrically distributed between the inner and outer bilayer leaflets. For example, the primary lipids in outer leaflet of human erythrocytes are PC and SM, while PE and the anionic lipids phosphatidylserine (PS), and phosphatidylinositol (PI) are segregated on the cytosolic side of the cell [14, 56]. Third, sterols such as cholesterol constitute a major component in mammal plasma membranes; 1:1 cholesterol:phospholipid by mole [17]. Indeed, numerous in vitro studies on both natural and synthetic cationic membrane-active antimicrobials have shown that the presence of anionic lipids increases membrane disruption and permeabilization [15].

Bacteria plasma membrane

A

Species	% CL	% PG	% PE
Gram-negative bacteria (with PE)			
Escherichia coli	5	15	80
Enterobacter cloacae	3	21	74
Yersinia kristensenii	20	20	60
Proteus mirabilis	5	10	80
Klebsiella pneumoniae	6	5	82
Pseudomonas aeruginosa	11	21	60
Gram-positive bacteria (no PE)			
Staphylococcus aureus	42	58	0
Streptococcus pneumonia	50	50	0
Gram-positive bacteria (with PE)			
Bacillus cereus	17	40	43
Bacillus polymyxa	8	3	60

Human RBC plasma membrane

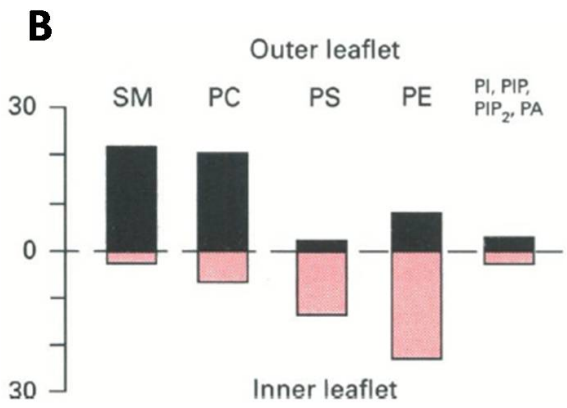

Figure 1.12: Plasma membrane compositions of bacteria and eukaryotic cells. A. On average the plasma membranes of bacteria cells contain higher amounts of anionic lipids and negative spontaneous curvature ($c_0 < 0$) lipids. B. Human erythrocyte cells have plasma membranes typical of eukaryotic cells. They contain less anionic and $c_0 < 0$ lipids and confine them to the inner leaflet of the plasma membrane. A is adapted from ref [57]. B is from ref [56].

Recently we have shown that the antimicrobial behavior of synthetic phenylene ethynylene antimicrobial oligomers (AMOs) correlates with their ability to selectively induce topological transitions to non-lamellar inverted hexagonal phases in membranes enriched in negative intrinsic curvature lipids, such as those with PE headgroups [104, 105] and cardiolipin [106]. Finally, membranes enriched with cholesterol are less susceptible to AMPs [107]. Taken together these results indicate membrane lipid composition plays an important role in AMP selectivity.

1.4.3 Proposed mechanisms of activity

From in vitro studies, amphipathic AMPs are inferred to disrupt membranes through a combination of non-specific electrostatic and hydrophobic interactions [14, 15, 69, 16, 108, 107, 109]. In this mechanism the cationic and hydrophobic moieties play complementary roles. Interaction between the anionic membrane and the cationic AMP leads to a strong electrostatic attraction and subsequent binding of the AMP to the membrane. Upon

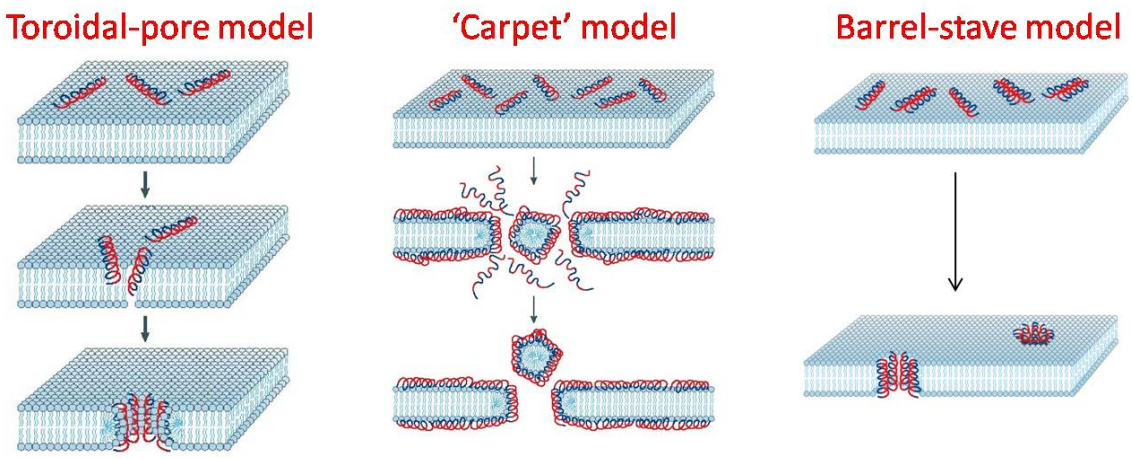

Figure 1.13: Proposed mechanisms for AMP membrane activity: The toroidal pore model (left), the carpet model (middle), and the barrel stave model (right). Cartoon adapted from [15]

adsorption to the membrane the hydrophobic portions of the AMP insert into the non-polar region of the bilayer leading to membrane destabilization and loss of barrier function [14, 15, 69, 16, 108, 107, 109]. Based on studies of AMPs with model membranes composed of single or mixed lipids three models have been previously proposed to describe the insertion of AMPs into the bilayer: the toroidal pore, carpet, and barrel-stave models [69, 15].

In the toroidal-pore model, (Figure 1.13, left) insertion of peptides into the membrane eventually induces a self-connection between the two monolayer leaflets, creating a pore that is lined with both lipid head groups and AMPs. Under specific experimental conditions toroidal pores have been observed for protegrin-1 [110], melittin [111], and magainin-2 [112, 110] with x-ray and neutron scattering techniques. Similar results were found for protegrin-1 [113], and the synthetic analog of magainin-2, MSI-78 [114], using NMR spectrometry. In the carpet model (Figure 1.13, middle) the peptides bind and cover the membrane surface until a threshold concentration is reached. The adsorbed peptides then disintegrate the membrane in a detergent-like manner into micelles [69]. This model has been used to explain the membrane activities of the dermaseptins [115, 116], and cecropins [117, 118] since they exhibit maximal permeation after coating the surfaces of liposomes. In the barrel stave

model (Figure 1.13, right) the peptides aggregate in the bilayer and then span it to form a transmembrane pore. The hydrophobic portions of the peptides face the non-polar interior of the bilayer and the hydrophilic portions are exposed to solution. Results from oriented circular dichroism [119], neutron scattering [111], and x-ray scattering [120] experiments suggest that alamethicin induces this type of membrane pore.

However, these three models do not exhaust the types of membrane disruptions that have been observed for membrane active antimicrobials. There are many ways in which AMPs can act against bacterial membranes. For example, SEM micrographs of pseudomonas aeruginosa after a few minutes of exposure to the sheep cathelicidin SMAP29 showed the presence of large blebs on the bacterial cell surface [15, 121, 122]. Electron microscopy on cross sections of E. coli after treatment with the antimicrobial parodixin showed significant surface vesicularization [123]. And electron micrographs show treatment of E. coli cells with protegrin-1 produces numerous microvilli in the bacterial membrane [124]. It was recently shown that the pore-forming peptide melittin can induce budding in vesicles by promoting lipid phase separation [125]. In particular, this last study illustrates that the specific form of membrane disruption depends on both the peptide and on the physiochemical properties of the membrane. Overall, the diversity of outcomes suggests that in addition to pore formation AMPs can destabilize membranes and compromise their barrier function through multiple processes including blebbing, budding, and vesicularization. Furthermore, the resultant membrane destabilization mechanism is due to interplay between the unique properties of both the AMP and membrane. Therefore, it is often the case that a specific type of membrane destabilization mechanism cannot be described as the membrane mechanism of activity for an AMP.

While membrane permeation is a general feature of AMP activity, there is emerging evidence that certain AMPs utilize other mechanisms of microbial killing, as a number of AMPs have been shown to bind to intracellular targets and consequently inhibit metabolic processes in bacteria. For example, some AMPs have been shown to directly bind DNA.

The arginine-rich AMP buforin II from frog was found to penetrate E. coli without lysing the cell membrane and inhibit cellular functions by binding to DNA and RNA [82]. Tachyplesin I from horseshoe crab, which is also arginine-rich, penetrates bacterial membranes without lysing them and directly interacts with the minor groove of the DNA duplex [126]. And the tryptophan, proline, and arginine-rich bovine AMP indolicidin also kills bacteria without lysing the cell membrane by binding DNA [126]. Indolicidin is also an inhibitor of nucleic acid and protein synthesis, and can induce filamentation in E. coli as a result of preferential inhibition of DNA synthesis [127]. Other AMPs have been shown to inhibit macromolecular synthesis. The proline and arginine-rich AMP PR39 from pig also halts synthesis of nucleic acids and proteins which leads to their degradation and bacterial cell death [128]. In addition to permeabilizing both the outer and inner membranes of E. coli, human α-defensins HNP-1 and -2 cease DNA, RNA, and protein synthesis [129]. And at their minimum inhibitory concentrations pleurocidin from flounder and pleurocidin-derived AMPs can translocate into bacterial cells and exhibit their antimicrobial activities by inhibiting macromolecular synthesis [130]. Even though membrane permeabilization is not a sufficient condition for full antimicrobial activity of certain AMPs, it is still a sufficient condition for their activity because the peptide must cross the cytoplasmic membrane in order to reach its internal target. Therefore, membrane interaction remains an important activity component of non-lytic AMPs, even if their membrane interactions differ from those of their lytic counterparts.

In addition to their direct antimicrobial abilities many AMPs play other indirect roles in the host immune response. Mammalian defensins and cathelicidins have been implicated as modifiers of the innate immunity and in bridging the innate and adaptive immune systems. HNP-1 and -2 are chemotactic in vitro for human monocytes [131] and T-cells [132], as well as naive T-cells and immature dendritic cells [133]. Human β-defensins also act as chemokines, as human β-defensin-2 promoted an adaptive immune response by recruiting immature dendritic cells and memory T-cells through interaction with human chemokine re-

ceptor 6 (CCR6) [134], and HBD-3 & -4 are chemotactic for monocytes [135, 136]. Similarly, the cathelicidins LL37 from human [137], indolicidin from bovine [138], PR39 from pig [139], and CRAMP from mouse [140] have all been shown to chemoattract various types of leukocytes. Neutrophil α-defensins from human, rat, guinea pig, and rabbit all induced histamine secretion from mast cells [141], as did HBD-2 and LL37 [142], indicating they can directly trigger inflammatory response. And HNPs [143, 144] and LL37 [145] stimulate release of cytokines such as interleukin 8 (IL-8) from epithelial cells and keratinoctyes, respectively. These results demonstrate that mammalian AMPs have a broad range of immune activation functions.

Differently, certain AMPs have been associated with the prevention of deleterious effects to the host from excessive inflammatory response. For example, LL37 partially protected mice against lethal endotoxic shock induced by high concentration lipopolysaccaride (LPS) [146]. Both indolicidin and LL37 inhibited LPS-induced tumor necrosis factor alpha (TNF-α) release in human macrophage/monocyte-like THP-1 cells indicating they have antiendotoxin ability [138]. Like other AMPs, both of these cathelicidins can directly bind to LPS [147], which may prevent proinflammatory cytokine secretion since the neutralized LPS is unavailable to pattern recognition receptors. However, similar studies showed LL37 and bovine cathelicidin BMAP-27 suppress proinflammatory transcriptional responses in human monoctyes to LPS [148], suggesting these peptides have multiple endotoxin-neutralizing activities. Finally, HNPs have been shown to assist cell division in epithelical cells and fibroblasts [149], induce epithelial cell proliferation [150], and enhance wound closure [151], suggesting these peptides have growth-promoting properties which help to counteract the destructive side-effects of inflammation.

1.4.4 Summary

From the above, it can be seen that there is abundant evidence that AMPs have multiple roles in host defense. They are generally microbicidal, but many also display specialized immune

modulation functions. It is known that collectively, AMPs share the fundamental structural motif of amphiphilicity. A number of natural questions emerge. How does this amphilicity connect the to specific activity of AMPs against bacterial membranes but not eukaryotic membranes? Moreover, it is not generally known whether there are additional systematic patterns in AMP sequences, and how these patterns relate to peptide-lipid interactions that enable membrane destabilization. Identification of such patterns can in principle lead to deterministic molecular engineering of AMPs. Finally, how can relatively short simple amino acid sequences such as those found in AMPs evolve such a broad range of functions? The purpose of this thesis is to sketch some drafts of answers.

Chapter 2

Small Angle X-ray Scattering for Probing the Interactions Between Macromolecules and Lipid Membranes

The focus of this thesis is the curvature deformations amphipathic molecules generate in lipid membranes. In order to resolve structural details the size of the probe must be at least on the order of the length scale of desired resolution. A typical copper rotating anode source which uses the $CuK_{\alpha 1}$ emission line produces x-ray radiation with wavelength $\lambda = 1.54045\ \mathring{A}$ [152]. Since the thickness of a lipid bilayer is, $t \sim 4nm$, x-ray scattering is an appropriate tool to characterize lipid membrane structural deformations. By quickly peeking into reciprocal space to determine the region of interest we see that $\lambda/2t \sim sin\theta \approx \theta$. This area of reciprocal space is often called the small angle regime, and the x-ray technique is called small angle x-ray scattering.

The liquid crystalline structures that result from self-assembly of biological materials are somewhat different than the crystalline structures commonly found in atomic solids such as solid state materials and metals. Liquid crystals are soft, in that the characteristic interaction energies between molecules are on the order of the thermal energy, k_BT. In atomic solids the inter-atomic interaction energies are usually much greater, and range up to electron volts for covalently bonded materials [153]. Thermal fluctuations substantially influence the structure of liquid crystalline systems and the crystals are usually more disordered than atomic solids. The reduced order in liquid crystalline systems means that the electron density distributions of the molecules often contribute significantly to the scattering spectra, and it is often easier to think of these systems in terms of partially ordered distributions of density as opposed to

discrete lattice vectors.

In this Chapter we first review x-ray scattering with an emphasis on small-angle x-ray scattering and its application to the structural characterizaton of biologial macromolecule self-assembly. The presentation and discussion of x-ray scattering is based on references [154, 155, 156, 157]. Next we summarize a few relevant studies where interactions between macromolecules and lipid membranes induced phase transitions and membrane curvature.

2.1 Small Angle X-ray Scattering

2.1.1 Formalisms of x-ray scattering

The simplest scattering structure, i.e. composed of more than one unit, is one composed of two electrons (Figure 2.1). One electron is centered at the origin and the other one is placed at position $\mathbf{r}$. A plane wave of radiation described by $\mathbf{A} = A_0\hat{\mathbf{x}}e^{i(\mathbf{k}\cdot\mathbf{r}-\omega t)}$ is incident on the structure. In the classical picture the electric field of the radiation exerts a force accelerating the electrons and causing them to radiate the signal in the form of a spherical wave. Here we assume the scattering is elastic so the emitted radiation has equivalent wavelength to the incident wave. We wish to determine the path length difference of the radiation from the two electrons at detector position $\mathbf{R}$.

Assuming the detector distance is very far away, $R >> \lambda$, the emitted spherical waves are essentially plane waves at the detector. The incident wave with wavevector, $\mathbf{k}$ where $|k| = \frac{2\pi}{\lambda}$, arrives at the electron at $\mathbf{r}$ after it has scattered from the electron at the origin. Therefore, the incident phase lag for the incident wave, ϕ_{in}, will be 2π multiplied by the ratio of z to the wavelength λ. Since z is the projection of $\mathbf{r}$ onto the incident wave, $\phi_{inc} = \mathbf{k}\cdot\mathbf{r}$. Differently, the scattered wave with wavevector, $\mathbf{k'}$, from the electron at $\mathbf{r}$ is ahead the scattered wave from the electron at the origin by an amount $\phi_{out} = \mathbf{k'}\cdot(\mathbf{R}-\mathbf{r})$ for large R. Since $|k| = |k'|$ this can be written $\phi_{out} = kR - \mathbf{k'}\cdot\mathbf{r}$, and the total phase difference is $\phi = \phi_{in} + \phi_{out} = kR + (\mathbf{k}-\mathbf{k'})\cdot\mathbf{r}$. The field at $\mathbf{R}$ is

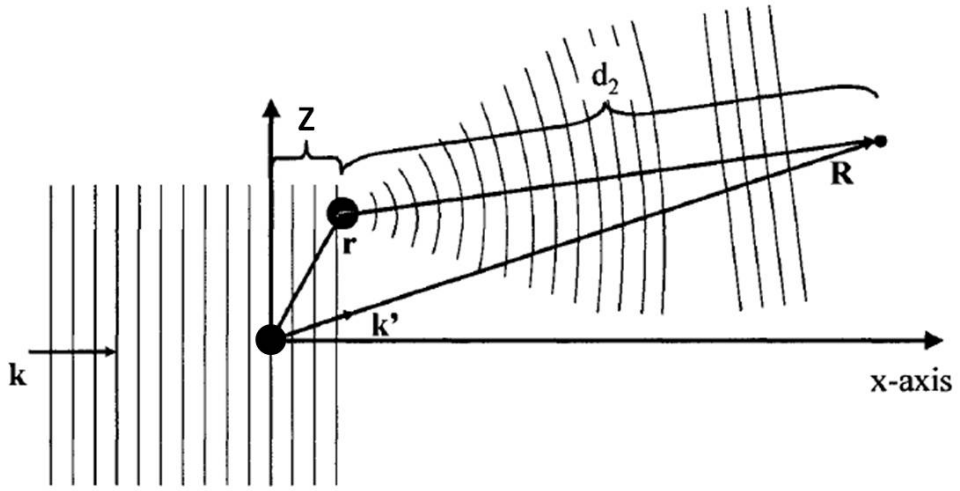

Figure 2.1: Schematic of scattering from two electrons. Scattered radiation is approximated as a spherical wave. For $R >> \lambda$ the radiation is a plane wave at detector position $\mathbf{R}$. Image adapted from [158].

$$A = A_0 e^{i(kR+(\mathbf{k}-\mathbf{k'})\cdot\mathbf{r}-\omega t)} \tag{2.1a}$$

$$A = A_0 e^{i(kR+\mathbf{Q}\cdot\mathbf{r}-\omega t)} \tag{2.1b}$$

where the momentum transfer vector, $\mathbf{Q} \equiv \mathbf{k} - \mathbf{k'}$. Calling the angle between $\mathbf{k}$ and $\mathbf{k'}$ 2θ we have $Q = \frac{4\pi}{\lambda}\sin\theta$.

This same procedure can be applied to systems with more than two electrons. However before proceeding we can tidy up this expression by dropping the phase factor $kR-\omega t$, since a real scattering experiment measures the intensity, which is proportional to the modulus squared of the complex electic field. Generalizing to an assembly of j electrons with positions $\mathbf{r_j}$ the elastic scattering amplitude may be written

$$A(\mathbf{Q}) = \sum_{\mathbf{r_j}} e^{i\mathbf{Q}\cdot\mathbf{r_j}} \tag{2.2}$$

However, in the above equations it is assumed that the positions of the electrons are known with certainty. Realistically, an electron is described by a (complex) wavefunction, $\Psi(\mathbf{r})$, where $|\Psi(\mathbf{r})|^2$ corresponds to the probability of finding the particle at position $\mathbf{r}$. Therefore an assembly of electrons is better described by a distribution specified by a number density $\rho(\mathbf{r})$. In this case the scattering amplitude becomes

$$F(\mathbf{Q}) = \int \rho(\mathbf{r}) e^{i\mathbf{Q}\cdot\mathbf{r}} d\mathbf{r} \tag{2.3}$$

In the limit $Q \to 0$ the different volume elements scatter completely in phase and $F(0) = Z$ where Z is the number of electrons. As Q increases the volume elements begin to scatter out of phase and $F(Q \to \infty) = 0$. Therefore, the scattering signal from a distribution of electric charge can be calculated from the Fourier Transform of the distribution.

2.1.2 Scattering from lipid bilayers and lamellar phases

Let's apply equation 2.3 to see what we might expect scattering from an isolated lipid bilayer to look like. Writing the electron density of a perfect plane as $1(x)1(y)\delta(z)$, the scattering amplitude in reciprocal space is a line, $\delta(Q_x)\delta(Q_y)1(Q_z)$. However, lipid bilayers have finite thickness so a more realistic 'slab' model for the electron density of a bilayer with thickness t may be written $\rho(x, y, z) = 1(x)1(y)(H(z) - H(z - t))$, where the Heaviside function $H(z)$, is one for $z > 0$ and zero otherwise. The scattering amplitude in this case becomes $\delta(Q_x)\delta(Q_y)\sin(Q_z t)/(Q_z t)$. Unlike the thin sheet, since the slab has finite thickness intramolecular scattering produces interference effects which are manifested in the modulation of the scattering amplitude. The scattering amplitude is zero when $Q_z = 2\pi n/t$, where $n = 1, 2, ...$, so the frequency of modulation decreases with decreasing thickness and in the limit that $t \to 0$ we recover the thin sheet profile.

Accurate fits of the scattering intensity require better models of the lipid bilayer electron density distribution. For phospholipids the head group is electron dense while the hydrocar-

bon tails are not; the hydrocarbon chain region in a phospholipid bilayer has less electron density than water. Therefore, the bilayer has a non-constant electron density distribution. A reasonable model for the bilayer electron density approximates the headgroup regions as two identical Gaussians, and the interior hydrocarbon region as a single Gaussian [159, 160]. The electron density for this 3 Gaussian model may be written:

$$\rho(z) = \Delta\rho_H e^{-(z-z_H)^2/2\sigma_H^2} + \Delta\rho_H e^{-(z+z_H)^2/2\sigma_H^2} + \Delta\rho_T e^{-z^2/2\sigma_T^2} \tag{2.4}$$

This corresponds to a symmetric bilayer centered at $z = 0$ with peak-to-peak thickness $t = 2z_H$. The $\Delta\rho_i$ where $i = H, T$ are the electron densities of the headgroup and tail regions relative to the solution, respectively, and the σ values are their widths. Since the bilayer electron density is centrosymmetric the Fourier transfrom can be replaced with just the cosine transform and the scattering amplitude is

$$F(Q) = \int \rho(z)\cos(Qz)\ dz = \\ (2\pi)^{1/2}(2\Delta\rho_H\sigma_H e^{-\sigma_H^2 Q^2/2}\cos(Qz_H) + \Delta\rho_T\sigma_T e^{-\sigma_T^2 Q^2/2}) \tag{2.5}$$

Typically our samples consist of liposomes so the scattering signal is effectively 'powder averaged'; all orientations of the bilayer to the incident beam are equally probable. The diffraction intensity will be proportional to

$$I(Q) \propto p(Q)l(Q)|F(Q)|^2 \tag{2.6}$$

The polarization factor, $p(Q) = (1 + \cos 2\theta/2) \approx 1$, for small angle x-ray scattering. Furthermore for powder samples the Lorentz factor, $l(Q) = \sin^2\theta\cos\theta$, is taken to be $1/Q^2$. Figure 2.2A shows the measured SAXS spectra for a solution of small unilamellar vesicles (SUVs) with lipid composition DOPS/DOPE = 20/80, along with the fit of the data based

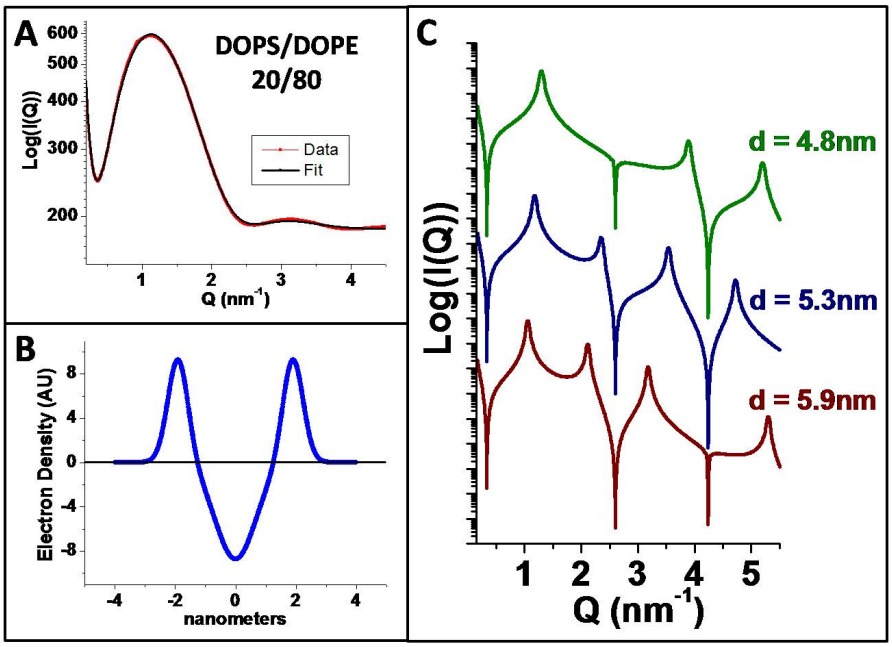

Figure 2.2: Electon density reconstruction of a single lipid bilayer from SAXS spectra of SUVs. A. Scattering from vesicles composed of DOPS/DOPE = 20/80 lipids shows a broad feature characteristic of the form factor from lipid bilayers (red curve). The scattering intensity is fit via nonlinear curve-fitting (Matlab) using the symmetric 3 Gaussian model plus a power law background: $Coefficient/Q^n + Constant$. B. Bilayer electron density from the 3 Gaussian model. The peak-to-peak thickness is $t_{pp} = 3.80nm$. C. Example lamellar phase SAXS spectra for various lattice spacings based on the DOPS/DOPE = 20/80 lipid bilayer fit from A. As d decreases the peaks shift outward and are modulated by the form factor. Complete cancellation of the second and fourth order reflections are seen for $d = 4.8nm$ and $d = 5.9nm$, respectively.

upon the 3 Gaussian model. Good agreement is seen between the data and fit. The bilayer electron density corresponding to the fit is shown in Figure 2.2B. As expected the headgroup electron densities are greater than the surrounding solution, while the electron density of the hydrocarbon region dips into negative values, indicating that the bilayer interior has less electron density. Finally the thickness of the bilayer, as measured from the peaks of the headgroup e-densities, is $t_{pp} = 3.80nm$, a typical value for a lipid bilayer.

Up to this point we have considered the scattering from isolated assemblies of electric charge, such as a single lipid bilayer. However, macromolecular assemblies like membranes often self-assemble into other crystalline phases. This is analogous to atomic solids where

atoms comprise a crystal. In the model of the diffraction pattern the scattering from an atomic crystal is built up from the electrons in the atom, then the atoms in the unit cell, and then finally the cells in the crystal. Since a crystal has translational symmetry, the position vector can be written as $\mathbf{r'_j} = \mathbf{R_n} + \mathbf{r_j}$, where $\mathbf{R_n}$ is a lattice vector specifying the location of a unit cell, and $\mathbf{r_j}$ is the position of an atom in that unit cell. The scattering amplitude is then

$$A(Q) = \overbrace{\sum_{\mathbf{r_j}} f_j e^{i\mathbf{Q}\cdot\mathbf{r_n}}}^{\text{unit cell}} \quad \overbrace{\sum_{\mathbf{R_n}} e^{i\mathbf{Q}\cdot\mathbf{R_n}}}^{\text{lattice structure factor}} \tag{2.7}$$

The first sum is the unit cell form factor. It describes the scattering from the atoms within the unit cell. The f_j's are 'weights' based upon the electron distributions of the j^{th} atom in the cell. The second sum is over the lattice sites of the crystal. Generally, this structure factor will be large only when $\mathbf{Q}$ coincides with a reciprocal lattice vector. Going back to our isolated membrane, the bilayer electron density corresponds to the unit cell form factor. The lattice structure factor turned out to be equal to 1 because the single bilayer occupied the only lattice site.

A commonly observed lyotropic phase is the L_α or lamellar phase. The L_α consists of stacks of lipid membranes. From a larger perspective the membranes composing the L_α can be thought of as the different layers in an 'onion' multi-lamellar liposome. The electron density for a lamellar phase with inter-bilayer spacing, d, and N lattice planes can be written

$$\rho_{L_\alpha} = \rho_{bilayer}(z) \otimes 1(x)1(y) \sum_{n=-N/2}^{N/2} \delta(z - nd) \tag{2.8}$$

where $\otimes$ is the convolution operator. Taking the Fourier transform of this expression, and noting that the Fourier transform of the convolution of two functions is the product of their Fourier transforms, we immediately get back a version of equation (2.7). The scattering amplitude will be

$$A_{L_\alpha}(Q) = F_{bilayer}(Q) \sum_{n=-N/2}^{N/2} e^{inQd} \tag{2.9a}$$

$$= F_{bilayer}(Q) \frac{\sin((N+1)Qd/2)}{\sin(Qd/2)} \tag{2.9b}$$

where the first term is the form factor for the bilayer, and the second term is due to the crystal lattice sites. The intensity can be written [155]

$$I \propto \frac{|F_{bilayer}(Q)|^2}{Q^2} \frac{\sin^2((N+1)Qd/2)}{\sin^2(Qd/2)} \tag{2.10a}$$

$$I \propto \frac{|F_{bilayer}(Q)|^2}{Q^2} (N + 2\sum_{k=1}^{N-1}(N-k)\cos(kQd)) \tag{2.10b}$$

Figure 2.2C shows some example spectra for different lattice spacings, d, using the bilayer electron density from the fit of the above DOPS/DOPE = 20/80 SUVs, and N = 20. The structure factor term, $\sin^2((N+1)Qd/2)/\sin^2(Qd/2)$, reaches a maximum when $Qd/2\pi = 1, 2, 3...$, and Bragg reflections are observed. These reflections are modulated by the form factor and the effect can be dramatic. For example, for $d = 5.9nm$, the minimum in the form factor completely extinguishes the fourth order reflection (Figure 2.2C), while the second order reflection is absent when $d = 4.8nm$. Modulation of the structure factor intensities by the form factor is the basis for electron density reconstruction of the unit cell, which in this case will be the lipid bilayer and intercalated solution. The integrated intensities of the reflections 'sample' the form factor signal. Their amplitudes can be used as coefficients in a Fourier series along with the correct choice of phases (± 1 for centrosymmetric cells), to reconstruct the unit cell (see [161, 162] for a more complete discussion).

2.1.3 Debye-Waller factor

Real molecules do not remain at a fixed spot, but instead experience diffuse motion about their average position due to thermal agitation. Therefore, the position of nth unit cell is $\mathbf{R'_n} = \mathbf{R_n} + \mathbf{\Delta x_n}$ where $\mathbf{\Delta x_n}$ is the displacement of the nth unit cell. Referring back to equation (2.9), we see that the structure factor portion of the scattering amplitude for the lamellar phase is now

$$S' = \sum_{n=-N/2}^{N/2} e^{inQd} e^{-iQ\Delta x_n} \tag{2.11}$$

Assuming the average displacements are small, the exponential containing $\mathbf{\Delta x_n}$ can be expanded as a series

$$e^{-iQ\Delta x_n} = 1 - iQ\Delta x_n - Q^2\Delta x_n^2/2 + ... \tag{2.12}$$

We are interested in the average of this quantity. The average of a quantity is the average of its terms. Since the nth bilayer jiggles around position $\mathbf{R_n}$, $\langle \Delta x_n \rangle = 0$. Neglecting higher order terms we write

$$\langle e^{-iQ\Delta x_n} \rangle = 1 - Q^2\langle \Delta x_n^2 \rangle/2 \tag{2.13}$$

Finally assuming the statistical behavior of the displacements of all the bilayers in the lattice are equivalent and uncorrelated, the subscript n can be dropped. The structure factor is now

$$S' = \sum_{n=-N/2}^{N/2} e^{inQd}(1 - Q^2\langle \Delta x^2 \rangle/2) \equiv S(1 - Q^2\langle \Delta x^2 \rangle/2) \tag{2.14}$$

This is generally used in the practically equivalent form

$$S' = Se^{-\langle \Delta x^2 \rangle Q^2/2} \tag{2.15}$$

So thermal agitation has the effect of reducing the diffracted intensity by an amount

$$D \equiv e^{-\langle \Delta x^2 \rangle Q^2/2} = e^{-M} \tag{2.16}$$

D is known as the Debye-Waller factor. Since D decreases with Q its effects are more apparent for higher order reflections. Furthermore, thermal agitation does not broaden diffraction lines, nor does it change their shape. The above treatment of thermal agitation was for a 1D lattice built from identical membranes. Generalization to 2 & 3 dimensions is straightforward [154]. However, in higher dimensions the Debye-Waller factors need not be isotropic, and the reflections which correspond to the crystal planes that are normal to the directions of greatest displacements will show the largest reduction in intensity. Finally if there are several different molecular species in the unit cell each of their Debye-Waller factors, e^{-M_j}, must be taken into account.

2.2 Previous SAXS Studies of Macromolecule-Induced Membrane Curvature

2.2.1 Interactions of DNA with phospholipid membranes

Self-assembled complexes of DNA and lipid membranes, so-called 'lipoplexes', have recently garnered much attention as potential gene delivery vectors. The introduction of anionic DNA to liposomes composed of cationic DOTAP (1,2-Dioleoyl-3-Trimethylammonium-Propane) and zwitterionic DOPC lipids produces a topological transition to a multi-lamellar structure, L_α^c, with DNA intercalated between adjacent lipid bilayers [65] (Figure 2.3). The average interaxial spacing between adsorbed DNA was shown to be directly controllable by the

membrane surface charge density. Upon dilution of DOTAP with DOPC the in-plane DNA separation continuously increased in a manner consistent with an expanding 1 dimensional lattice of DNA strands [65, 163]. The release of condensed counterions is responsible for the higher order of self-assembly. By forming a multi-lamellar structure, the DNA and lipid neutralize each other and release the 1D and 2D bound counterions in the bulk solution for a large entropic gain of $\sim 1k_BT$ per released counterion [164].

If the free energy of the cationic lipid-DNA system only depended on electrostatic interactions, the membrane would wrap around the DNA in order to maximize contact and thereby maximize counterion release. However, there is an energetic penalty associated with deforming a membrane away from its native state. The Helfrich elastic cost of wrapping a cylindrical membrane monolayer with radius of spontaneous curvature, R_0, and bending modulus, κ, around DNA with radius, R_{DNA}, is $f = \frac{1}{2}\kappa(1/R_0 - 1/R_{DNA})^2$ [37]. Therefore, it is expected that decreasing the bending modulus or enriching the monolayer with negative spontaneous curvature lipids should reduce the elastic resistance to membrane curvature. Koltover [37] showed that reduction of the bending modulus via addition of the cosurfactant molecule hexanol [165], or doping the membrane with $c_0 < 0$ DOPE lipids promoted a $L_\alpha^c \rightarrow H_{II}^c$ transition (Figure 2.3). Interestingly, the non-lamellar H_{II}^c complexes were more efficient at transfecting mammalian cells compared with their lamellar counterparts [37].

Lamellar to inverted hexagonal transistions have also been observed in anionic membranes complexed to DNA through interaction with divalent ions [38]. Unlike the attraction between cationic lipids and DNA which is mainly due to entropic forces from counterion release, anionic membrane-DNA complexes rely on multivalent ions to mediate complexation via direct electrostatic 'bridging' attractions [166]. In this system two different lamellar phases and one inverted hexagonal were observed (Figure 2.4) and the phase behavior was sensitive to divalent cation type and concentration as well as membrane charge density [38]. In DOPG/DOPC membranes, Ca^{2+} and Mg^{2+} ions promoted complexation of DNA into the L_α^c in membranes with lower anionic charge density, while high DOPG membranes expelled

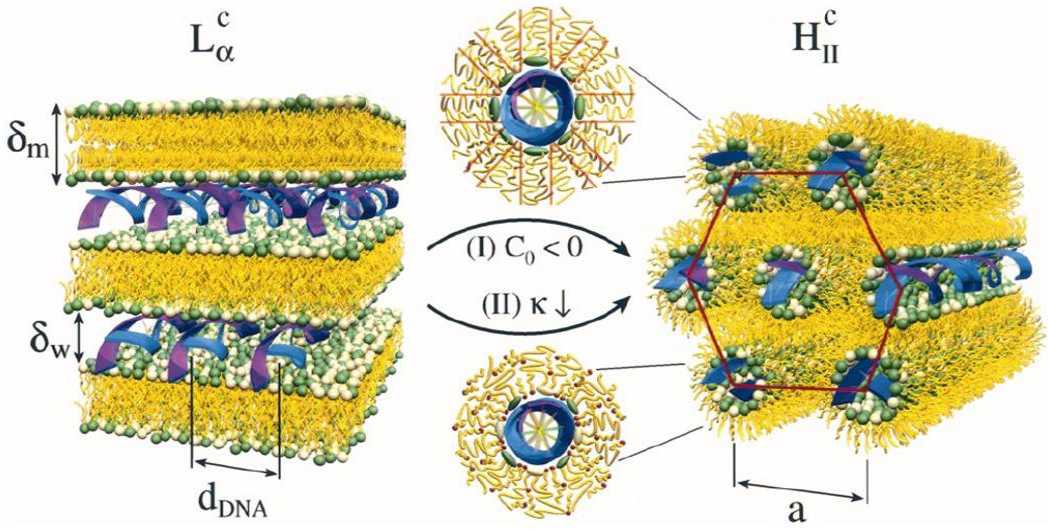

Figure 2.3: Self-assembled lamellar complexes of cationic lipids and DNA undergo a topological transition to an inverted hexagonal phase via two different pathways: Enriching the membrane with negative spontaneous curvature lipids (top), or decreasing the bending modulus by adding a membrane 'softening' surfactant (bottom). Figure adopted from [37].

the DNA and assembled into a lamellar phase consisting of membranes 'glued' together with the divalent ions [38]. Zn^{2+} ions, which are known to non-electrostatically coordinate lipids and produce membrane curvature, produced DNA-ion-membrane inverted hexagonal complexes at high Zn^{2+} concentrations [167]. Therefore, certain divalent ions can be used as an alternative method to produce membrane curvature.

2.2.2 Phenylene ethynylenes: synthetic antimicrobial compounds

The class of phenylene ethynylene oligomers (AMOs) display potent broad spectrum antimicrobial activity against both Gram positive and Gram negative bacteria [168, 169]. By increasing the oligomer hydrophobic content, homologues of these oligomers can be made inactive, specifically active against bacterial cells, or non-specifically active against both bacteria and red blood cells [104]. Previous reports have shown that their activity and selectivity correlates with an AMO-induced topological transition of small unilamellar liposomes into inverted hexagonal (H_{II}) phases [104]. A crucial membrane component was the con-

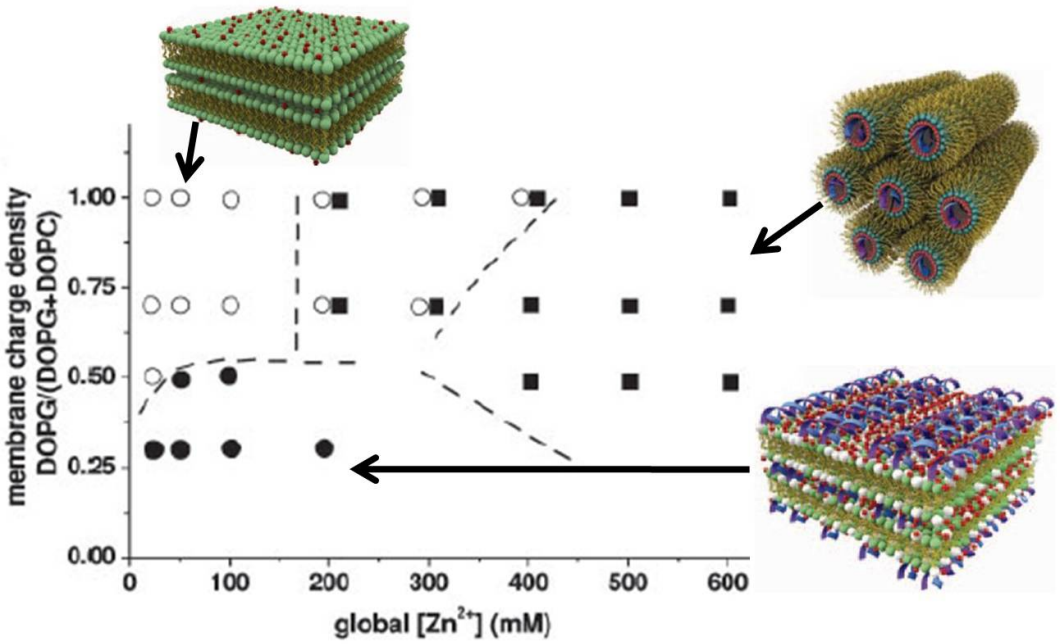

Figure 2.4: The phase behavior of DNA-Zn^{2+}-anionic lipid systems depends on membrane charge density and $[Zn^{2+}]$. At very high concentrations Zn^{2+} induces the H_{II}^{c} phase by altering the intrinsic curvature of the membrane. Figure adapted from [38].

centration of DOPE lipids. By using vesicles composed of ternary DOPG/DOPE/DOPC lipids at fixed anionic charge density, the threshold amount of DOPE necessary for H_{II} formation tracked with oligomer activity [104]. The inactive oligomer did not induce a topological transition over the entire range of tested membrane DOPE content (Figure 2.5A). The selectively active oligomer induced inverted hexagonal phases in membranes with high concentrations of DOPE only (Figure 2.5B), while drastically less membrane DOPE content was required for generation of the H_{II} phase by the non-specifically active oligomer [104] (Figure 2.5C). Since the cell membranes of Gram negative bacteria are composed of much greater amounts of DOPE than the plasma membranes of eukaryotic cells, these results imply there is a relationship between negative spontaneous curvature lipids such as DOPE, oligomer hydrophobic content, and selective antimicrobial activity. Moreover, the ability to generate non-lamellar membrane curvature is important to the mechanism of action for phenylene ethynylene antimicrobials. Similar results were observed in membranes enriched

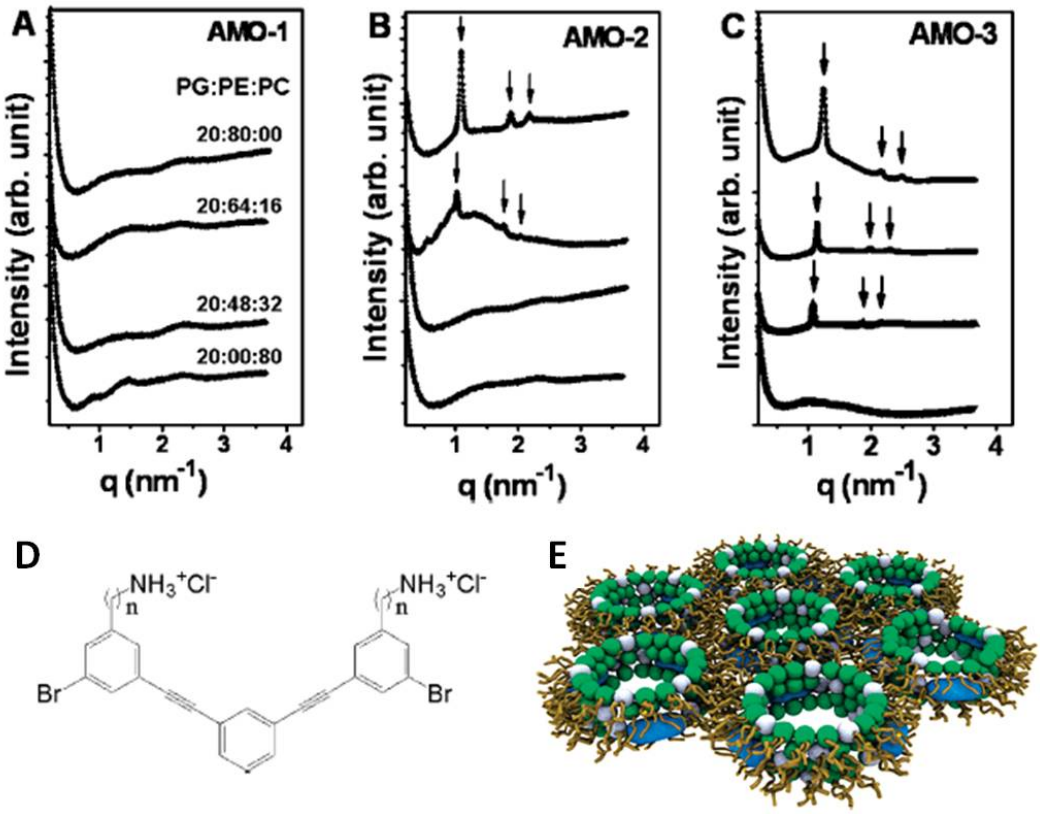

Figure 2.5: Generation of inverted hexagonal phases by antimicrobial phenylene ethynylene compounds correlates with their activity and selectivity. A. The inactive AMO-1 did not substantially restructure liposomes. B&C. The selectively active AMO-2 induced H_{II} phases in PE-rich membranes only, while the non-specifically active AMO-3 required much less membrane PE content to induce the H_{II}. D. AMO-n structures. Increasing hydrophobicity increases their potency. E. Cross section of the H_{II} phase. The AMOs are colored blue. Figure adapted from [104].

in cardiolipin, a major lipid component in the membranes of Gram positive bacteria, provided the solution contained low millimolar concentrations of biologically prevalent divalent Mg^{2+} or Ca^{2+} cations [106]. Since bound divalent cations can change the approximately zero spontaneous curvature of cardiolipin to negative values these results are consistent with the role of negative spontaneous curvature lipids in AMO activity [106].

A direct link between negative spontaneous curvature lipids and AMO bactericidal activity was shown via *in vitro* killing assays [105]. A PE-knockout mutant of E. Coli was much less susceptible to membrane-active phenylene ethynylenes than the wild-type bacte-

ria, but much more vulnerable when treated with the antibiotic tobramycin which is known to target the bacterial ribosomal machinery and is not membrane-active [105]. Since PE deletion is usually a lethal mutation, these results suggest one possible reason why bacterial resistance is more difficult to attain for this class of membrane-active antimicrobials than for conventional antibiotics [170, 169].

2.2.3 Prototypical arginine-rich cell-penetrating peptide: The TAT peptide

Cell-penetrating peptides are cognate to antimicrobial peptides. They comprise a class of short ($<$ 20 amino acid) cationic peptides that have the ability to traverse the cell membranes of many different types of mammalian cells. A wide variety of macromolecules have been attached to these peptides and subsequently internalized. Moreover, after uptake the cargo maintains its activity. The ability of cell-penetrating peptides to translocate biologically active molecules into cells makes these peptides promising candidates for drug delivery applications. While much controversy still surrounds their uptake mechanism, the emerging body of evidence suggests cell-penetrating peptides use multiple mechanisms to enter cells [171]. They can directly cross membranes [172, 173, 174, 175, 176]. They can also employ the cell's endocytotic machinery for translocation, as studies have shown uptake via clatharin-mediated endocytosis [177, 178, 179], caveolin-dependent endocytosis [180, 181], and macropinocytosis [182, 183, 184].

The most widely studied cell-penetrating peptide, the TAT peptide from the HIV transactivator protein is an 11 amino acid sequence peptide which has a net charge of +8 from 6 arginines and 2 lysines [185]. Arginine has an essential role in the translocation abilities of the TAT peptide. Substitution of any basic residue in the TAT peptide with a neutral alanine substantially reduces its activity while replacing one of the uncharged residues with alanine has no effect, indicating that the high positive charge of the TAT peptide is a neces-

sary for its activity [185, 186]. However, cationicity is not a sufficient condition. Polyarginine sequences with sufficient length display equivalent or better uptake compared with the TAT peptide [187, 188]. However, homopeptides of lysine, histidine, and ornithine with the same charge as the TAT peptide cannot enter cells.

Previous work has shown that the HIV TAT cell-penetrating peptide generates negative Gaussian membrane curvature, the type of membrane curvature found in pores, protrusions from macropinocytosis, invaginations from endocytosis [189]. Using synchrotron small angle X-ray scattering (SAXS), it was demonstrated that the TAT peptide (amino acid sequence: YGRKKRRQRRR) generates a cubic Pn3m 'double-diamond' phase (Figure 2.6A,C,&D) in membranes enriched with negative intrinsic curvature lipids [189]. Similar features are seen in the presence of 100 mM NaCl indicating that TAT peptide can generate these dramatic changes in membrane topology at physiological salt conditions (Figure 2.6A).

If the generation of negative Gaussian curvature is correlated with cell-penetrating peptide permeation ability, then peptides that are unable to penetrate cells should not induce membrane phases with negative Gaussian curvature. Experiments with polylysine, K_8, on membranes of identical composition to those used for TAT peptide, show interactions between the lipid head groups and polylysine induce wrapping of the membrane monolayers [189] (Figure 2.6B). The result is an inverted hexagonal phase where the much smaller columnar channels are filled with peptide and solution. This phase has negative mean curvature but zero Gaussian curvature. The absence of negative Gaussian curvature may explain the poor transduction ability of polylysine.

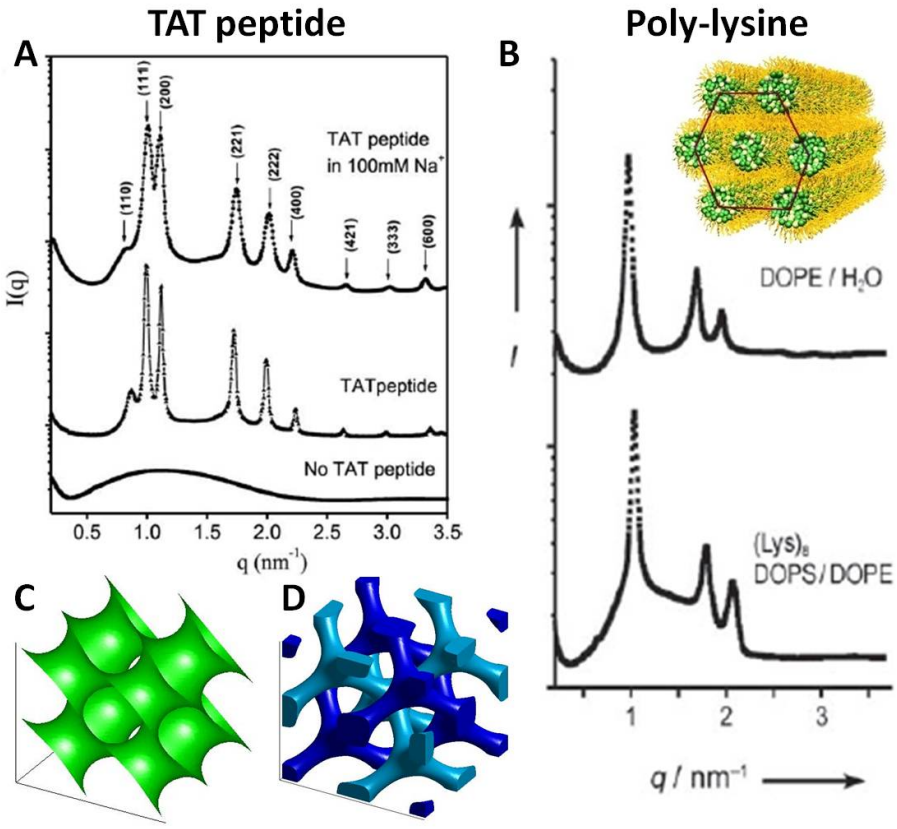

Figure 2.6: Generation of saddle-splay membrane curvature correlates with the uptake abilities of cell-penetrating peptides. A. The archetypal arginine-rich cell-penetrating peptide, the TAT peptide, generated a bicontinuous Pn3m cubic phase rich in saddle-splay curvature. B. Poly-lysine, which is known to have poor cell-penetrating ability, generated only inverted hexagonal phases which have negative mean curvature but zero Gaussian curvature. Illustrations of the minimal surface, C, and the non-intersecting water channels, D, of the Pn3m cubic phase. Figure adapted from [189, 171].

Chapter 3

Criterion for Amino Acid Composition of Defensins and Antimicrobial Peptides Based on Geometry of Membrane Destabilization

3.1 Introduction

Antimicrobial peptides (AMPs) comprise an important component of the innate host defense system. Collectively, AMPs have broad spectrum antimicrobial activity [14, 15, 69, 84]. Although AMPs are diverse in sequence and structure, most share two general structural features: they are amphipathic and cationic [14, 15]. From in vitro studies, AMP amphipathicity is inferred to disrupt membranes through a combination of electrostatic interactions of the cationic AMP with the anionic membrane followed by insertion of hydrophobic patches into the non-polar interior of the bilayer [14, 15, 69, 108, 107, 109]. Membranes can be disrupted by AMPs via a diverse range of processes, including pore formation, blebbing, budding, vesicularization [14, 15, 69, 84, 108, 107, 109, 77, 75, 76, 191, 123]. This diversity of outcomes has impeded the development of a detailed, molecular understanding of how AMPs destabilize bacterial membranes specifically. Such knowledge can in principle provide design rules that impact development of synthetic antimicrobials.

Mammals produce two main types of membrane active AMPs: defensins, [77, 75, 76] and cathelicidins [191]. Defensins comprise a potent class of membrane disruptive AMPs with well-characterized broad spectrum and selective microbicidal effects. Defensins are

[0]Much of this chapter is also discussed in: Schmidt, et al. JACS (2011) **133**, 6720, or [190]

synthesized by varied epithelia and by phagocytes, and function as a biochemical line of defense against microbial infection [77]. Vertebrate defensins share general features, including cationic charge, MW of 2-5 kDa, distinctive tridisulfide arrays, and β-strand structures constrained by the disulfide pairings [75, 76]. They can be separated into three subfamilies, α-defensins, β-defensins, and θ-defensins [75]. Since many aspects of defensin biology are known, this is an ideal prototypical family of AMPs to investigate the detailed molecular mechanisms responsible for selective activity against bacterial but not mammalian membranes.

In the first part of this chapter we use synchrotron small angle x-ray scattering (SAXS) to map out the fundamental curvature deformation modes induced in model cell membranes by defensins, and elucidate causative relationships between curvature deformations and membrane disruption processes. Mammalian defensins are systematically investigated, using members from the three defensin subfamilies, including rhesus monkey θ-defensin-1 (RTD-1), baboon θ-defensin-7 (BTD-7), mouse Paneth cell α-defensin cryptdin-4 (Crp-4), human β-defensin-2 (HBD-2), and human β-defensin-3 (HBD-3). The bactericidal activity of these defensins is correlated with the induction of saddle-splay (equivalently negative Gaussian) membrane curvature. All peptides restructured vesicles into porous bicontinuous phases rich in saddle-splay curvature when lipid compositions mimic those of bacterial membranes, but not when the lipid compositions are more representative of mammalian membranes. These results are shown to be consistent with vesicle leakage assays. A key parameter for activity is the concentration of negative intrinsic curvature ($c_0 < 0$) lipids, such as those with PE headgroups, which exist at significantly higher concentrations in bacterial cytoplasmic membranes compared to eukaryotic membranes. Existence of homologous behavior in synthetic antimicrobials, [104, 105, 106] suggests a common root mechanism for selective membrane permeation. A mechanism of action based on saddle-splay membrane curvature generation is broadly enabling, since it is a necessary condition for processes such as pore formation, blebbing, budding, vesicularization, all of which destabilize the barrier function of cell mem-

branes [192]. In general, AMPs destabilize membranes via a diverse range of processes, many of which involve saddle-splay curvature.

Saddle-splay membrane curvature generation places constraints on the amino acid composition of membrane disruptive peptides. In the second part of this chapter we show that the topological requirement for membrane destabilization implies that a decrease in arginine content in an AMP can be offset by an increase in both lysine and hydrophobic content. This criterion for amino acid compositions of AMPs based on the generation of saddle-splay curvature is consistent with trends in the amino acid composition of 1,080 known cationic AMPs. Lastly we demonstrate the consistency of this 'design rule' by showing that α-helical peptides with little homology to defensins also generate saddle-splay membrane curvature.

3.2 Experimental Section

3.2.1 Preparation of peptides

Recombinant Crp4 was expressed and purified as His6-tagged fusion proteins as described [193, 194, 195]. Expression of recombinant fusion proteins was induced by adjusting exponentially growing E. coli BL21-CodonPlus (DE3)-RIL cells to 0.1 mM isopropyl-β-D-1-thiogalactopyranoside and incubating at $37°C$ for 6 h in Terrific Broth as described in earlier reports. Cells were lysed by sonication in 6 M guanidine-HCl, 100 mM Tris (pH 8.0), and the suspension was clarified by centrifugation. His6-tagged fusion proteins purified by nickel-nitrilotriacetic acid resin affinity chromatography (Qiagen, Valencia, CA) were cleaved with cyanogen bromide and purified by analytical C18 reverse phase high pressure liquid chromatography (RP-HPLC). Peptide homogeneity was confirmed in analytical acid-urea polyacrylamide gel electrophoresis (AU-PAGE), a highly sensitive measure of defensin foldamers. Molecular masses were verified by matrix-assisted laser desorption ionization-time of flight mass spectrometry (MALDI-TOF MS) and peptides were quantified using extinction coefficient calculations at 280nm performed at ExPASY [196]. θ-defensins RTD-1 and BTD-7

were produced by solid phase synthesis, purified and characterized as described previously [197, 198]. HBD-2 and HBD-3 are expressed and purified as described in [199, 200].

3.2.2 Liposome preparation for x-ray measurements

DOPC (1,2-dioleoyl-sn-glycero-3- phosphocholine), DOPE (1,2-dioleoyl-sn-glycero-3- phosphoethanolamine), DOPG 1,2-dioleoyl-sn-glycero-3-[phospho-rac-(1-glycerol)] (sodium salt), and DOPS 1,2-dioleoyl-sn-glycero-3-phospho-L-serine (sodium salt), lyophilized lipids from Avanti Polar lipids were used without further purification. For x-ray experiments we prepared Small Unilamellar Vesicles (SUVs) by sonication. DOPG, DOPS were dissolved in chloroform/methanol, and DOPC, DOPE were dissolved in chloroform for stock solutions. Mixtures of DOPG and DOPE were prepared at 1:4 mass ratio to approximate bacterial lipid compositions, while DOPS, DOPC, and DOPE at 1:4:0, and 1:2:2 mass ratios were used to approximate the membranes of eukaryotic cells. Lipid mixtures were dried under N_2, dessicated overnight under vacuum, and resuspended at a final concentration of 20 mg/ml in Millipore H_2O. Solutions were incubated at $37°C$ overnight and then sonicated until clear. SUVs were obtained via extrusion (0.2 μm pore Nucleopore filter).

3.2.3 SAXS experiments

Defensin and lipid solutions were thoroughly mixed at specific peptide to lipid ratios (P/L) and sealed in quartz capillaries. All samples were prepared in 100-150 mM NaCl to simulate physiological salt conditions. For SAXS experiments at the Stanford Synchrotron Radiation Laboratory (BL4- 2) and at the Advanced Photon Source (BESSRC-CAT BL-12IDC), monochromatic X-rays with energies of 9-11 and 12 keV, respectively, were used. Scattered radiation was collected using a MAR Research CCD area detector (pixel size, 79 μm). Samples were checked for consistency by multiple measurements with different x-ray sources. No radiation damage was observed for the incident beam intensities and the exposure times

used. 2D SAXS powder patterns were integrated using the Nika 1.2 package [201] and FIT2D [202].

3.2.4 Vesicle dye leakage experiments

Giant Unilamellar Vesicles (GUVs) were prepared using the swelling method. Stock solutions of lipids DOPS, DOPE, and DOPC in chloroform were deposited (100μl at 20mg/ml) at the desired mass ratios onto roughened, cleaned Teflon, along with dye DiO (10mul at 1mg/ml). After drying under vacuum the Teflon was hydrated with moist nitrogen gas for 30min, and then 5ml swelling solution was added (100 mM sucrose plus 20μM Alexa 633 maleimide), and incubated for 2 days at 37°C. After swelling, the GUV suspension was diluted 40x into 200mM glucose. 200μl of this dilution was placed on a coverslip soaked in 1% BSA, and Crp4 (10μl at 1 mg/ml) was added. A Leica SP2 laser scanning confocal microscope was used.

3.2.5 Analysis of data from the antimicrobial peptide database

Data was obtained via the online antimicrobial peptide database [203, 204]. Comparison of helical peptides with defensins: Eligible peptides were required to be active against Gram-negative or Gram-positive bacteria. A pool of 299 peptides with helix structure is compared with a pool of 143 defensins. "Average% of AMP composition" is the number of times an amino acid is found in a pool divided by the total number of amino acids in that pool.

Lysine/arginine ratio versus %Hydrophobicity: Eligible peptides were required to have a net positive charge and be active against either Gram-negative or Gram-positive bacteria. Percentage of lysine, %K, and percentage of arginine, %R, were read off from the sequence information for a set hydrophobic bin. Here %K (%R) = Number of lysines (arginines) found in the bin/Total number of amino acids in the bin. Note that %K/%R = N_K/N_R (defined below). Lysine/arginine ratio versus $\langle Hydrophobicity \rangle$: Eligible peptides were required to

have a net positive charge and be active against either Gram-negative or Gram-positive bacteria. These criteria retrieved a pool of 1,080 peptides. For a given peptide, j, its average hydrophobicity is defined by:

$$\langle Hydrophobicity \rangle_j \equiv \frac{1}{n} \sum_{i=1}^{n} \omega_i \tag{3.1}$$

Where n = number of amino acids in the peptide, ω_i = the hydrophobicity of the ith amino acid in the peptide. This value is set by the particular hydrophobicity scale used. To facilitate easier comparison across scales, the value of the apparent free energy of membrane insertion for an amino acid, ΔG^{aa}_{app}, based upon the Wimley-White biological scale was reversed in sign, i.e. $\Delta G^{aa}_{app} \rightarrow -\Delta G^{aa}_{app}$. The published hydrophobicity values were used for all other scales. To partition each peptide into a bin the hydrophobic extremes for the pool were determined and used to set the range of hydrophobicity scale. The range was divided into 100 equal bins. For the M peptides in a given bin, we define:

$$\frac{N_K}{N_R} \equiv \frac{\sum_{j=1}^{M} (\text{number of K})_j}{\sum_{j=1}^{M} (\text{number of R})_j} \tag{3.2}$$

N_K/N_R versus $\langle Hydrophobicity \rangle$ is plotted for each of the 100 bins.

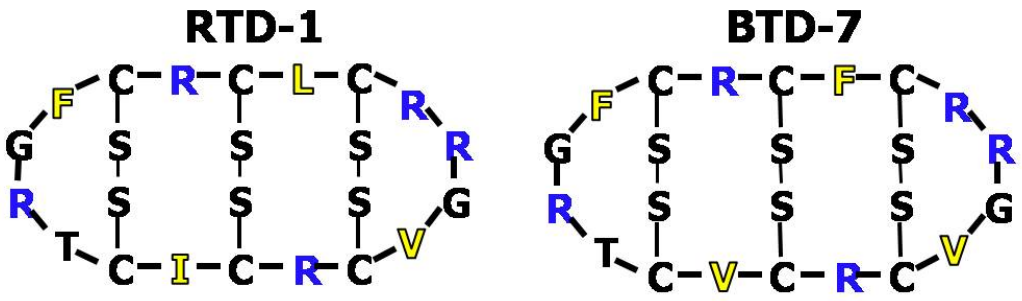

Figure 3.1: The θ-defensins used in this study: rhesus θ-defensin-1 (left) and baboon θ-defensin-7 (right). Cationic arginines are colored blue, and the hydrohobic amino acids are colored yellow.

3.3 Results

3.3.1 θ-Defensins generate saddle-splay curvature in model bacterial membranes with high PE concentrations but not in model eukaryotic membranes with low PE concentrations

θ-defensins are short 18 amino acid circularized peptides expressed only in old world monkeys and orangutans [77]. Previous in vitro studies have shown both rhesus θ-defensin-1 (RTD-1) and baboon θ-defensin-7 (BTD-7) (Figure 3.1) have activity against Gram-positive and Gram-negative bacteria, and fungi [197, 79]. Moreover, RTD-1 has antiviral activity against HIV-1 [205], and the herpes simplex virus [206]. Both θ-defensins are amphipathic and contain five arginine residues.

Small Unilamellar Vesicles (SUVs) with phospholipid compositions characteristic of Gram-negative bacteria (DOPG/DOPE = 20/80) were incubated with specific defensins to study the induced structural changes. Synchrotron SAXS profiles from lipid solutions only showed a broad characteristic feature consistent with a single lipid bilayer form factor expected for unilamellar vesicles (see Supporting Information, Figure S1). When exposed to RTD-1 or BTD-7 (Figure 3.2A&B), the vesicles underwent a drastic structural transition and displayed

characteristic correlation peaks with ratios, $\sqrt{2} : \sqrt{3} : \sqrt{4} : \sqrt{6}$, which indicate the formation of a cubic Pn3m double-diamond lattice. By fitting the slopes of the measured Q-values at every peak we calculate lattice parameters, $a_{BTD-7} = 16.00$ nm, and $a_{RTD-1} = 15.98$ nm, for BTD-7 and RTD-1, respectively[1]. The Pn3m (Figure 3.2C) is a bicontinuous cubic phase where two non-intersecting water channels are separated by a lipid bilayer [53]. The center of the bilayer traces out a minimal surface with negative Gaussian curvature at every point. Although bilayer saddle-splay curvature is different than the self-connected monolayer saddle-splay curvature seen in a toroidal pore (Figure 3.2D), it should be noted that each constituent monolayer in a bicontinuous phase also possesses negative Gaussian curvature at every point, and is equally accessible by AMPs. On such saddle-shaped surfaces (Figure 3.2C), the surface curves upwards in one direction and downwards in the perpendicular direction. For example, saddle-shaped surfaces are found inside toroids, which have a single hole each. This type of curvature is not found on the surfaces of spheres, which lack holes. Furthermore, protrusions such as buds and blebs (Figure 3.2D), require bilayer saddle-splay curvature at their base. Saddle-splay curvature is required for membrane poration, as well as for formation of different AMP-induced destabilization mechanisms depicted in Figure 3.2D.

To examine the role of membrane intrinsic curvature on induced saddle-splay curvature we constructed ternary lipid membranes of constant anionic charge (DOPG = 20%) but with varying ratios of DOPE ($c_0 < 0$) and DOPC ($c_0 \approx 0$). In contrast to effects on PE-rich membranes, RTD-1 and BTD-7 did not restructure vesicles that mimic eukaryotic membranes with low concentrations of PE. Phases rich in saddle-splay curvature were not induced by RTD-1 or BTD-7 in membranes with DOPG:DOPE:DOPC = 20:40:40 (Figure 3.2A&B), as indicated by the absence of their characteristic correlation peaks. The diffraction data

[1]While coexisting phases (such as lamellar and inverted hexagonal phases) are sometimes observed at specific lipid compositions the observed reflections cannot be accounted for without the presence of a Pn3m cubic phase. The strong induced formation of cubic phases like the Pn3m which are rich in saddle-splay curvature is a generic feature in the full phase diagram of defensin-lipid structures.

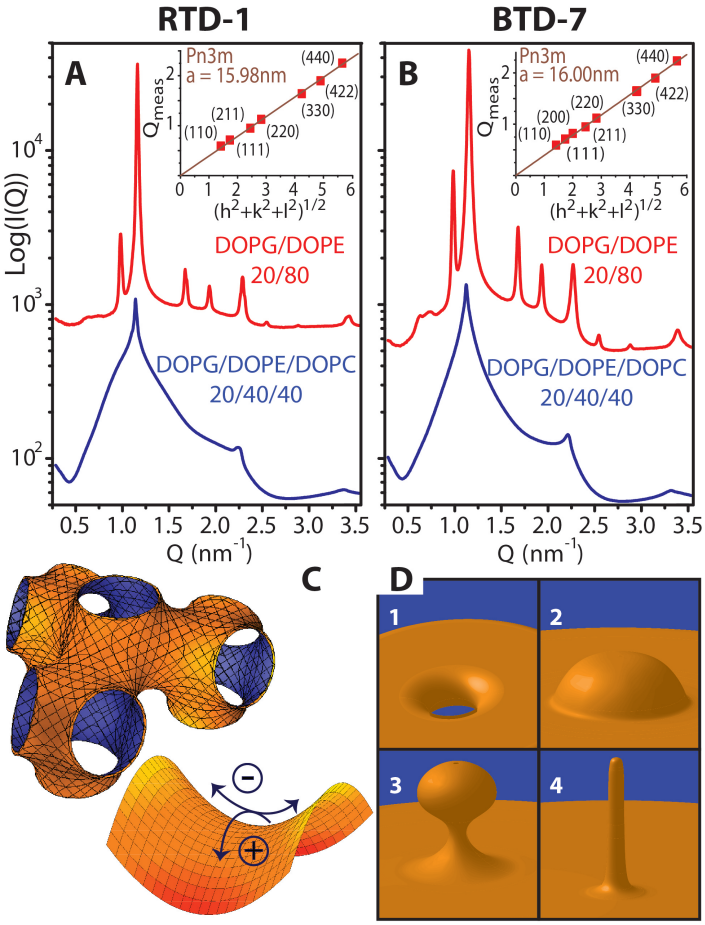

Figure 3.2: Generation of negative Gaussian curvature by θ-defensins is dependent on membrane PE concentration. At peptide to lipid molar ratio, P/L = 1/30, both RTD-1 (A) and BTD-7 (B) θ-defensins, induced a Pn3m cubic phase in SUVs with lipid compositions mimicking the cell membranes of Gram-negative bacteria, DOPG/DOPE = 20/80, but not in membranes with reduced amounts of negative intrinsic curvature lipids, DOPG/DOPE/DOPC = 20/40/40. Insets in A&B show indexation of the Pn3m cubic phase by agreement between the measured peak Q positions and the Miller indices h, k, l, with relationship $Q_{meas} = 2\pi\sqrt{h^2 + k^2 + l^2}/a$, for a cubic phase with lattice parameter, a. (C) (upper left) Illustration of the Pn3m cubic phase. The surface at the mid-plane between bilayer leaflets has zero mean curvature and negative Gaussian curvature at every point. (lower right) Negative Gaussian curvature requires positive curvature (+) in one direction and negative curvature (−) in the perpendicular direction to locally produce a saddle shape. (D) Diagrams of different manifestations of saddle-splay curvature in the interior of a pore (1) and at the base of blebs (2), buds (3), and rod-like projections (4). Figure adopted from [190].

showed a combination of broad form factor scattering characteristic of isolated bilayers and a lamellar phase with a periodicity of $d_{RTD-1} = 5.67$ nm and $d_{BTD-7} = 5.67$ nm for RTD-1 and BTD-7, indicating that weak inter-membrane attraction is induced, although curvature is not.

It is important to discriminate between necessary and sufficient conditions for saddle-splay curvature generation. Alamethicin [207], gramicidin S [208], and protegrin-1 [209], form cubic phases in pure PE lipids under specific processing conditions such as temperature cycling. The above results on defensins allow us to assess systematically the roles played by different lipid species. It has been previously proposed that anionic lipids in bacterial membranes are important for AMP function. We agree with this assessment. However, while anionic PG lipids and high curvature PE lipids in the target membrane are both necessary conditions for induction of saddle-splay curvature, neither by itself is a sufficient condition (see Supporting Information, Figure S2). Our data suggests that AMPs target distributions of lipids rather than individual lipid species.

3.3.2 Arginine-rich α-defensins also generate saddle-splay curvature in membranes enriched with PE and selectively permeate PE-rich GUVs

To investigate whether other arginine-rich defensins exhibit similar behavior we conducted similar experiments on mouse cryptdin-4 (Crp-4) (Figure 3.3), a 32 amino acid α-defensin expressed in mouse Paneth cells with in vitro microbicidal activity against Gram-negative and Gram-positive bacteria [210, 211]. Crp-4 is amphipathic and 7 of the 10 cationic amino acids in Crp-4 are arginine residues [212]. Like the θ-defensins, the α-defensin Crp-4 generated saddle-splay curvature in model bacterial membranes with high PE but not in model eukaryotic membranes with low PE. Incubation of Crp-4 with SUVs of high PE lipid composition produced a Pn3m cubic phase with lattice parameter, a = 11.1 nm (Figure 3.4A),

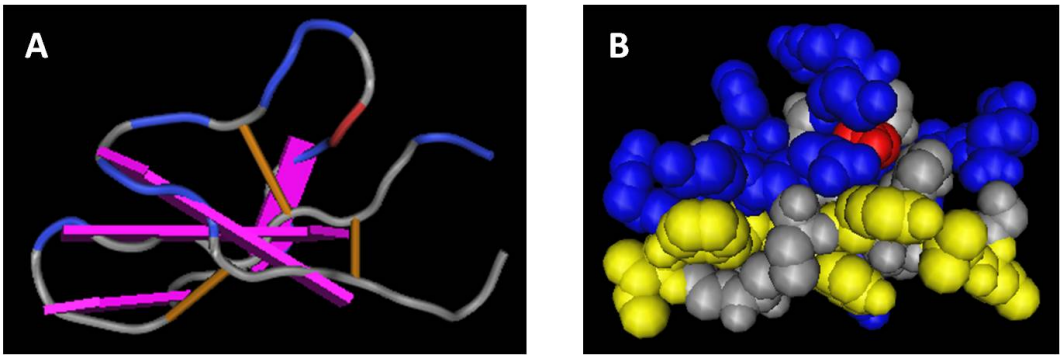

Figure 3.3: Solution structure of mouse Paneth cell alpha-defensin Crp-4 (protein data bank ID 2GW9) obtained by NMR. Crp4 sequence: GLLCYCRKGHCKRGERVRGTCGIRFLY-CCPRR. A. Structure shown in worm rendering. The three disulfide bonds from 6 cysteines are displayed in orange, and β-sheets are represented by purple arrows. Blue regions denote cationic amino acids (arginine, lysine, and histidine), while the anionic glutamic acid is red. B Space filled structure illustrates the cationic (blue) and hydrophobic (yellow) patches of amphipathic Crp-4. Neutral residues are colored grey. From [213].

while reduction of membrane DOPE content led to the disappearance of the Pn3m cubic phase.

Interestingly, previous work suggests that negative intrinsic curvature lipids can promote pore formation through modification of the Gaussian modulus [51, 50]. As discussed in section 1.2.8, the Gauss-Bonnet theorem shows the formation of a toroidal pore in a membrane changes the Gaussian curvature, K, in the membrane by an amount $\Delta \int K \cdot dA = -4\pi$, so the free energy change from pore formation is $\Delta E = \kappa_G \Delta \int K \cdot dA = -4\pi\kappa_G$. Typically the bilayer Gaussian curvature modulus, κ_G^b, is negative, which exacts a free energy penalty for pore formation. In section 1.2.8 it was shown (equation 1.5) that κ_G^b is

$$\kappa_G^b = 2(\kappa_G - 4\kappa c_0 d) \tag{3.3}$$

Here κ_G (< 0, from the lateral stress profile of the monolayer) is the Gaussian curvature modulus of the monolayer, κ (> 0) is the monolayer bending modulus, c_0 is the spontaneous curvature of the monolayer, and d (> 0) is the distance from the middle of the bilayer to the monolayer pivot point [50]. Usually the negative value of the monolayer Gaussian curvature

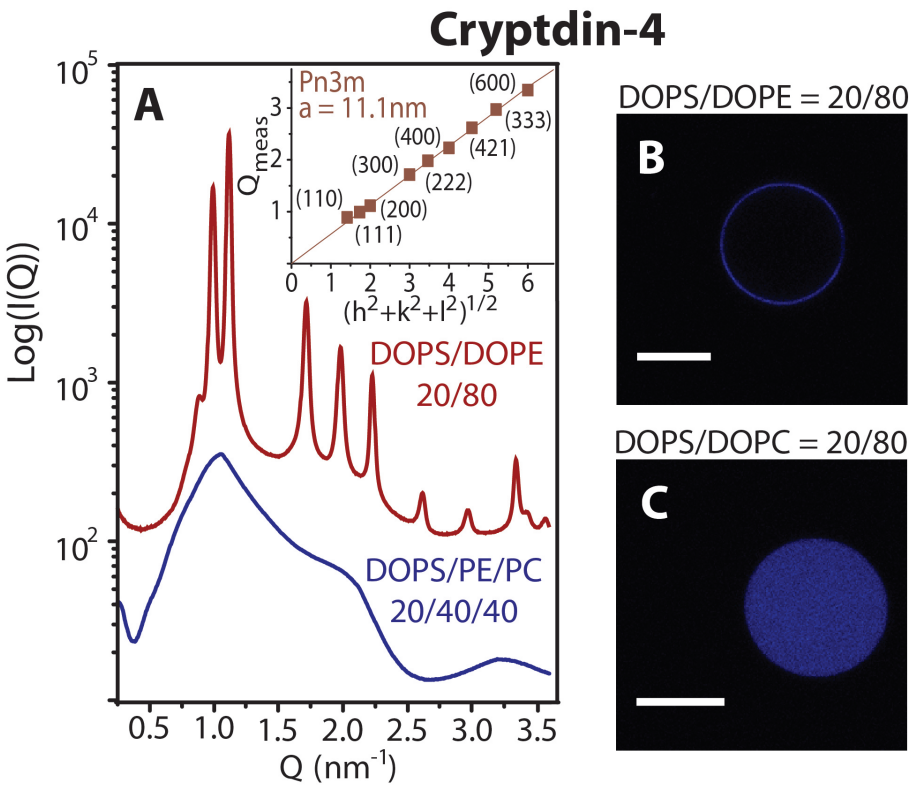

Figure 3.4: The α-defensin Crp-4 showed similar phase behavior to θ-defensins which suggests a general mechansim for selectivity by defensins rich in arginine. At P/L = 1/45, Crp-4 induced a Pn3m cubic phase in DOPS/DOPE = 20/80 membranes, but induced a lamellar phase with lattice spacing, a = 6.0nm in DOPS/DOPE/DOPC = 20/40/40 membranes. Figures B and C show representative GUVs after treatment with Crp-4. Dye leakage occurred in vesicles enriched with DOPE (B), but not in vesicles enriched with DOPC (C), consistent with the relationship between membrane PE content and the creation of porous phases by defensins. White scale bars are 10μm. Figure from [190].

modulus ensures that κ_G^b remains negative, and pore formation is energetically unfavorable. However, negative intrinsic curvature lipids ($c_0 < 0$) such as PE change the bilayer Gaussian curvature modulus toward positive values [51]. The decreased free energy barrier to changes in membrane topology toward porous phases is consistent with our observation that membranes rich in negative intrinsic curvature lipids are more susceptible to pore formation.

Our x-ray experiments measure AMP-induced curvature deformations in a 3D lipid system, which has the freedom to connect into bulk phases such as the Pn3m. Both eukaryotic and prokaryotic cells have quasi-2D membranes, where induced saddle-splay curvature de-

formations can take the form of pores, blebs, or buds. To determine how peptide-induced saddle-splay curvature is manifested in 2D membranes we investigated the effect of Crp-4 on giant unilamellar vesicles (GUV) by confocal microscopy. Liposomes with lipid compositions mimicking the membranes of bacteria (PS/PE = 20/80) and of eukaryotic cells (PS/PC = 20/80) were loaded with maleimide dye and incubated with Crp-4 (molar ratio P/L=1, see Experimental Section). Dye leakage was evident in PE-rich membranes after peptide exposure (Figure 3.4B), consistent with Crp-4 induced pore formation in the intact vesicles. In contrast, negligible dye leakage was observed in PC-rich vesicles (Figure 3.4C). Selective permeation of GUVs rich in PE but not PC is consistent with the observation of pore-enabling Crp-4 induced saddle-splay curvature (Figure 3.4A) from SAXS experiments. Taken together, these results indicate Crp-4 preferentially creates pores in membranes with negative intrinsic curvature lipids.

3.3.3 Generality of mechanism for defensins and relation of curvature generation to antimicrobial peptide sequence: HBD-2 and HBD-3 as examples

We hypothesized the selective induction of saddle-splay curvature in model bacterial membranes is a generic feature among defensins. We used human β-defensin-2 (HBD-2, DEFB4) and human β-defensin-3 (HBD-3, DEFB103A) [214], to test this hypothesis (Figure 3.5). HBD-2 is a 41AA amphipathic peptide [215], which is predominately effective against Gram-negative bacteria [199]. HBD-3 is 45AA, amphipathic, and is generally more potent than HBD-2 [214, 216]. Unlike the other two defensin subfamilies which strongly favor arginine over lysine, β-defensins have intermediate arginine to lysine ratios [76]. In HBD-3 the cationic residues consist of 7 arginines and 6 lysines, and HBD-2 has 2 arginines, 5 lysines, and 1 histidine.

Figure 3.6 shows the SAXS spectra of model bacterial and model eukaryotic membranes

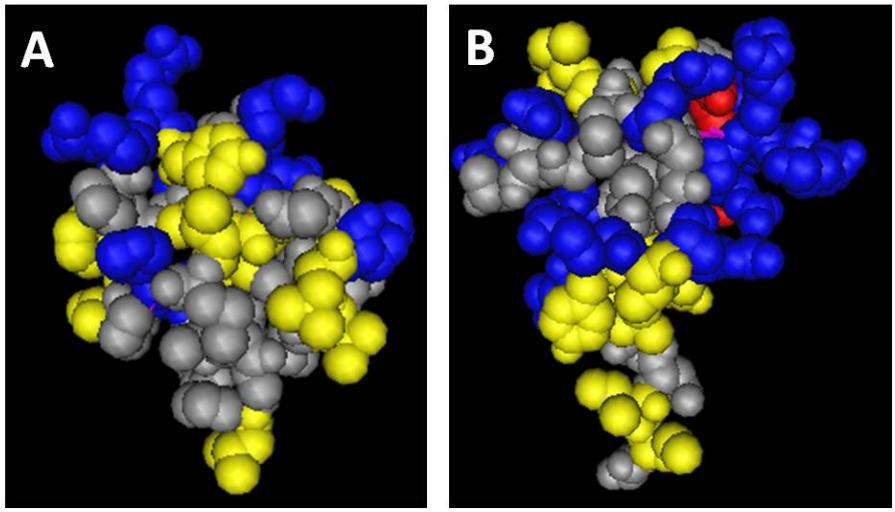

Figure 3.5: Structures of human β-defensin-2 (protein data bank ID 1E4Q), and human beta defensin-3 (protein data bank ID 1KJ6). HBD-2 with sequence: GIGDPVTCLKSGAICHPVFCPRRYKQIGTCGLPGTKCCKKP, is shown on the left. HBD-3 with sequence: GIINTLQKYYCRVRGGRCAVLSCLPKEEQIGKCSTRGRKC-CRRKK, is on the right. Cationic amino acids are colored blue, anionic amino acids are red, hydrophobic amino acids are yellow, and neutral residues are gray. Images rendered using the macromolecular structure viewer Cn3D, from website: http://www.ncbi.nlm.nih.gov/Structure/CN3D/cn3d.shtml

after exposure to HBD-2 and HBD-3. The capacity for membrane-specific saddle-splay curvature generation is observed, and is consistent with behavior of θ-defensins and α-defensins. Both β-defensins showed weak interactions with membranes enriched with DOPC, and produced lamellar phases in membranes with intermediate amounts of PE/PC (Figure 3.6A&B). In DOPS/DOPE = 20/80 membranes, HBD-2 generated a Pn3m cubic, with lattice parameter a = 13.8 nm (Figure 3.6A). HBD-3 also generated saddle-splay curvature in DOPS/DOPE = 20/80 membranes, which is exhibited in reflections with ratio, $\sqrt{6} : \sqrt{8} : \sqrt{14} : \sqrt{16}$, characteristic of the cubic Ia3d 'gyroid' phase with a = 18.0 nm (Figure 3.6B). Like the Pn3m, the Ia3d is a bicontinuous cubic phase consisting of two non-intersecting water channels separated by a single lipid bilayer which has saddle-splay curvature everywhere on its minimal surface [41].

3.3.4 Average induced saddle-splay curvature, $\langle K \rangle$, from SAXS measurements allows quantitative comparison of different antimicrobial peptides

Our previous work on cell penetrating peptides [189, 171], has shown lysine and arginine generate different types of membrane curvatures. Since lysine and arginine are cationic they both induce wrapping by anionic membranes. As explained in the Wet Electrostatics section (1.3), this is due to the entropy of counterions condensed on both the charged membrane and on the short charged polymers. Electrostatic compensation between a cationic polymer [217] and an anionic membrane [63] leads to the release of condensed counterions into the bulk solution and a corresponding large entropy gain, which results in strong polymer-membrane binding. This has been observed in a large number of systems [65, 218, 219]. Since maximal contact between the peptide and membrane leads to maximal counterion release, the membrane will tend to wrap around the peptide generating negative curvature [220, 37]. The guanidine group of arginine supports multi-dentate hydrogen bonding, which can organize

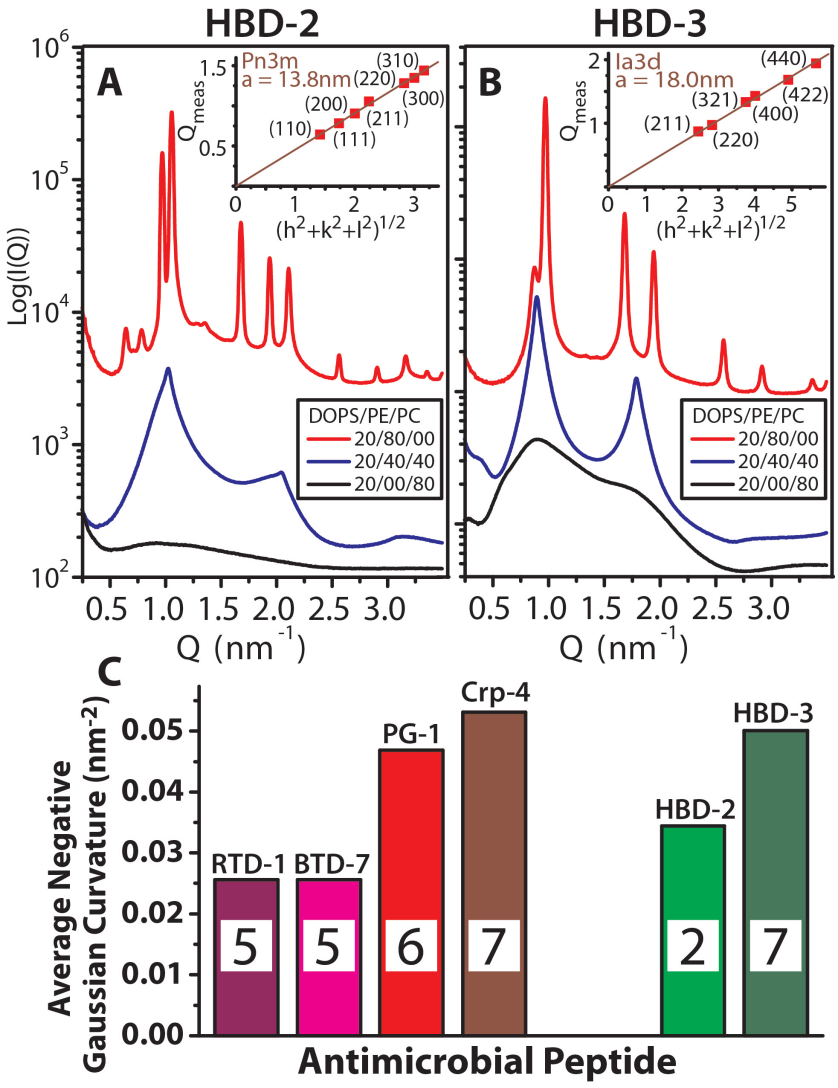

Figure 3.6: β-defensins with intermediate arginine/lysine ratios also generated negative Gaussian curvature. Neither HBD-2 (A) or HBD-3 (B) produced cubic phases in membranes with low PE concentrations. In DOPS/DOPE/DOPC = 20/40/40 membranes, HBD-2 and HBD-3 restructured SUVs into lamellar phases with lattice spacings d = 6.2nm and 7.0nm, respectively, and DOPS/DOPC = 20/80 membranes showed only weak interaction with both β-defensins. Conversely, in DOPS/DOPE = 20/80 membranes HBD-2 induced coexisting Pn3m and inverted hexagonal (lattice spacing a = 7.5nm) phases, while HBD-3 induced an Ia3d cubic phase. P/L = 1/35 for HBD-2, and 1/55 for HBD-3. (C) Comparision of the average negative Gaussian curvature, $\langle K \rangle$, produced in 80% PE membranes by AMPs rich in arginine (left group) and by AMPs with both lysines and arginines (right group) around the peptide to lipid isoelectric point. The inset in each bar graph corresponds to the number of arginines in the AMP. Figure from [190].

bulky lipid head groups to generate positive curvature in the perpendicular direction, resulting in saddle-splay curvature (Figure 3.7). In contrast, the amine group of lysine can only hydrogen bond to one lipid head group at a time [221, 222]. Consistent with this, polylysine induces negative mean curvature on membranes to form inverted hexagonal phases, while polyarginine can also induce saddle-splay curvature to form cubic phases. Clearly more work, experimental, theoretical, and computational, is required for a full understanding of these effects. Extant theoretical studies [223, 224, 225] suggest the anisotropy associated with saddle-splay curvature deformations may also provide AMPs with a way to communicate and organize cooperatively.

The Pn3m, Ia3d, and Im3m cubic phases are related by a Bonnet transformation, so their average Gaussian curvatures can be quantitatively compared [53, 41]. Recall (equation 1.9) that the average Gaussian curvature is $\langle K \rangle = \frac{2\pi\chi}{a^2 A_0}$, where a is the cubic lattice constant, χ is the Euler characteristic, and A_0 is the surface area per unit cell. Figure 3.6C shows the $\langle K \rangle$ values extracted from the diffraction data for arginine-rich defensins (RTD-1, BTD-7, Crp-4) and protegrin-1 (PG-1) [74], (see Supporting Information, Figure S3). A correlation exists between negative Gaussian curvature and arginine content in structurally similar peptides. HBD-2 and HBD-3, which have ∼50% lysines and ∼50% arginines, clearly deviate from this curve, although $\langle K \rangle$ is more negative for HBD-3 compared with HBD-2, consistent with the greater number of arginines in HBD-3.

3.3.5 The requirement of saddle-splay membrane curvature generation places strong constraints on amino acid composition of antimicrobial peptides: the saddle-splay curvature selection rule

Defensins can generate pores [75, 77, 76], but AMPs have been observed to disrupt membranes via processes that do not involve pores. Generation of the required saddle-splay

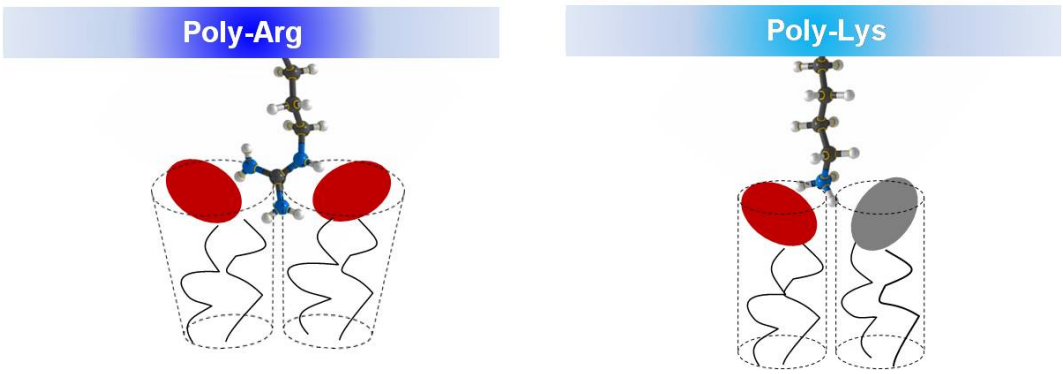

Figure 3.7: Illustration of the hydrogen bonding abilities of arginine and lysine with lipid headgroups. The guanidinium group of arginine (left) can form multiple hydrogen bonds with lipid headgroups leading to positive curvature generation. The amino group of lysine (right) can only hydrogen bond to a single lipid headgroup at a time and, therefore, cannot generate positve curvature.

membrane curvature for these processes places strong constraints on the amino acid composition and composite hydrophobic and cationic components of membrane disruptive peptides. Hydrophobic amino acids generate positive curvature [108, 107, 226]. Non-polar components of the amphipathic peptide are inserted into the membrane, which increases the hydrophobic volume of the perturbed lipid monolayer and thereby creates positive curvature strain. Differences in lipid headgroup chemistry will not drastically affect this mechanism.

Cationic amino acids work differently. We have demonstrated lipid head group organization by arginine and lysine generates distinct types of membrane curvature deformations. These interactions provide an AMP with complementary curvature producing mechanisms. Arginine generates negative Gaussian curvature (positive and negative curvatures along the two perpendicular principal directions), whereas lysine generates negative curvature along one direction only (Figure 3.7). Mechanisms of curvature generation based on head group re-organization are inherently sensitive to head group chemistry, therefore such mechanisms will be conducive to mediating specific peptide-lipid interactions.

Based on the above, a series of rules governing the amino acid content of membrane

disruptive antimicrobial peptides can be proposed. A decrease in arginine content in a peptide sequence will imply that less negative Gaussian curvature can be generated. This can in principle be compensated for by an increase in both lysine and hydrophobic content. This 'exchange rate' concept between arginines and lysines/hydrophobes is illustrated in a comparison between the amino acid content[2], of β-sheet bonded defensins and that of α-helical AMPs (Figure 3.8A&B). The average arginine composition of α-helical AMPs is $\sim$50% that of defensins, but the proportion of most hydrophobic amino acids in α-helical AMPs is $\sim$200% that found in defensins (Figure 3.8A). Likewise, whereas most of the hydrophilic amino acids are found in similar proportions for α-helical AMPs and defensins, the proportion of lysines in α-helical AMPs has drastically increased by $\sim$300% relative to that in defensins (Figure 3.8B). Thus, there is a unifying conceptual link between α-helical AMPs and β-sheet AMPs: β-sheet AMPs generally rely more on arginines to generate curvature, while α-helical AMPs rely more on lysines and hydrophobes to do so. In both cases, the end result is the generation of saddle-splay curvature.

Within a more general compass, a strong manifestation of this 'saddle-splay curvature selection rule' for amino acid content can be observed in the compositions of AMPs. We test this selection rule against 1,080 known cationic peptides with activity against Gram positive or Gram negative bacteria [203]. Figure 3.9A shows a plot of N_K/N_R (the ratio of the number of lysines to the number of arginines) vs %Hydrophobic (% of hydrophobic amino acids in peptide, see Experimental Section), in which all AMPs have been binned into 7 histograms. A strong increasing trend consistent with the saddle-splay curvature selection rule can be discerned. Figure 3.9B-D shows a similar analysis of AMP amino acid sequences using more sophisticated measures to quantify peptide hydrophobicity, using three established scales (Kyte-Doolittle [227], Eisenberg consensus [228], Wimley-White biological [229]), in which

[2]In Figure 3.8 we exclude the amino acids cysteine, proline, and glycine which primarily influence AMP tertiary structure and are not directly involved in the cationicity or hydophobicity of AMPs. Also we consider only arginine and lysine in our exchange rate concept since they constitute the vast majority (89%) of cationic AA found in the 1,080 AMPs.

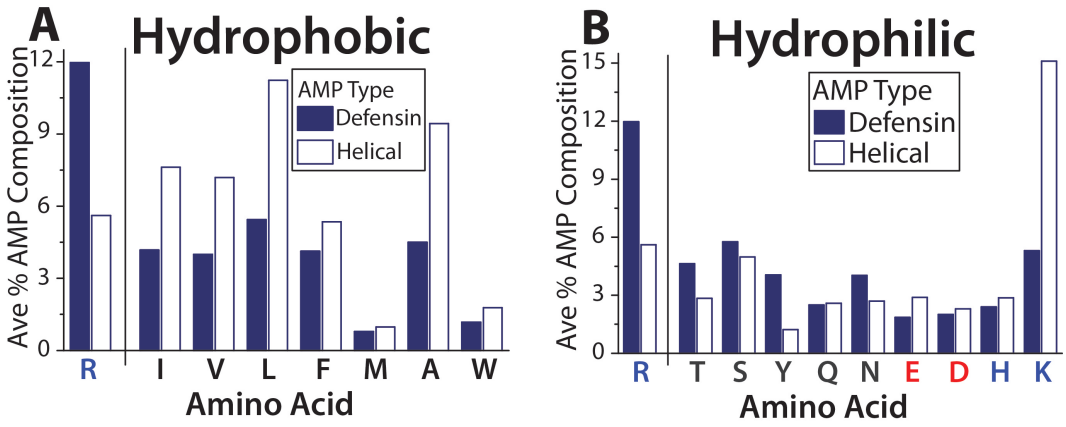

Figure 3.8: The exchange of R with K and hydrophobicity is illustrated by comparing β-sheet defensins with α-helical AMPs. (A) On average defensins contain much greater amounts of R than α-helical AMPs, and utilize less of each type of hydrophobic amino acid. (B) Overall, the proportion of hydrophilic amino acids is comparable in defensins and α-helical AMPs. The exception is K, which is more commonly found in α-helical AMPs. Blue denotes basic amino acids, while negatively charged amino acids are colored red. Figure from [190].

all AMPs have been partitioned into 100 bins. A strong positive correlation is observed between hydrophobicity and $\log N_K/N_R$. Even though we do not account for effects due to proximate amino acids, sequence, and peptide conformation in our simple approach, there is strong exponential-like dependence between hydrophobicity and N_K/N_R, consistent with the saddle-splay curvature selection rule.

3.3.6 Demonstration of the generality of curvature generation by antimicrobial peptides: α-helical AMPs melittin and magainin-2 generate saddle-splay curvature

To test the consistency of the saddle-splay curvature selection rule similar SAXS studies were performed on the α-helical AMPs melittin and magainin-2. Melittin is a 26 amino acid peptide expressed in the European honey bee [230, 231]. It is the principle component of bee venom and displays potent membrane-lytic activities against both eukaryotic and bacteria cells [231, 232, 233]. Magainin-2 is a 23 amino acid host-defense peptide isolated from the skin

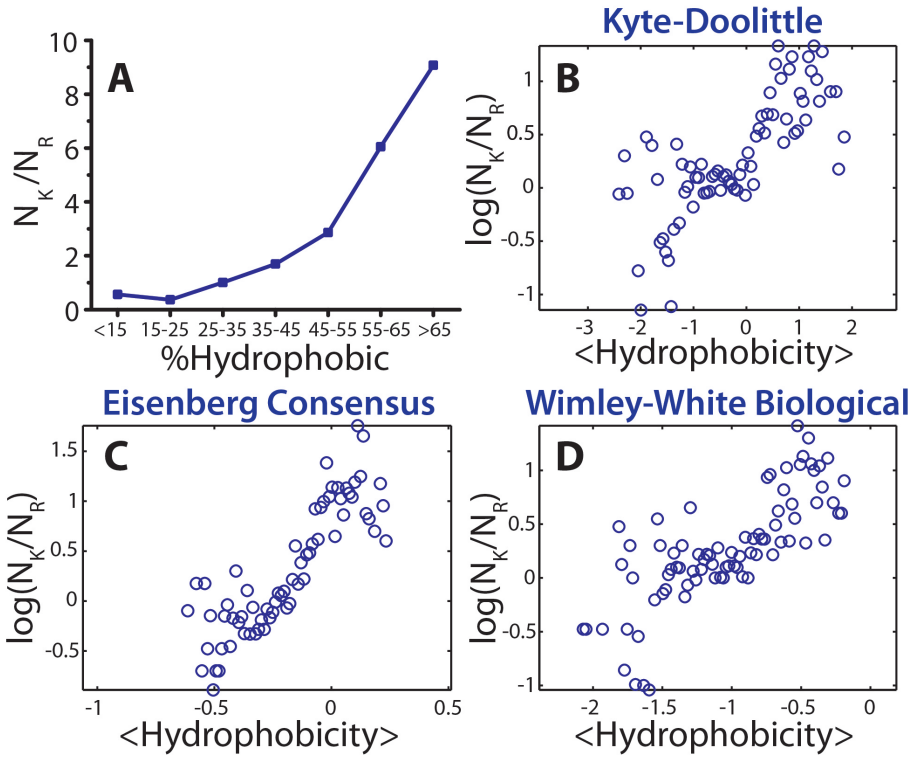

Figure 3.9: Demonstration of the exchange between R, with K and hydrophobicity based upon 1,080 cationic AMPs in the antimicrobial peptide database. (A) By organizing all 1,080 AMP sequences into 7 histogram bins, a strong positive dependence between the peptide lysine to arginine ratio and peptide hydrophobicity percentage can be observed. More robust calculations of hydrophobicity based upon the widely used Kyte-Doolittle (B), Eisenberg Consensus (C), and Wimley-White (D) hydrophobicity scales show the same relationship between the exchange of arginine with lysine and hydrophobicity consistent with the saddle-splay curvature selection rule. See Experimental Section for details and binning schemes in B-D. Figure from [190].

of the African clawed frog [72]. Magainin-2 exhibits broad spectrum antimicrobial activity against numerous species of Gram postive and Gram negative bacteria and fungi, and is non-hemolytic at microbicidal concentrations [72, 234]. Circular dichroism experiments on both melittin [235] and magainin-2 [236] have shown that while they are unstructured in solution, both peptides adopt α-helical conformations upon contact with membranes. The α-helical secondary structure partitions their cationic and hydophobic residues onto opposing faces of the helix rendering them amphipathic. Melittin is highly hydrophobic (46% by %Hydrophobic) and has 3 lysines and 2 arginines that are mostly clustered at the peptide C-terminal. Magainin-2 is less hydrophobic (39% by %Hydrophobic) than melittin and has 4 lysines and a histidine. In line with expectations both melittin and magainin-2 induced saddle-splay curvature in model bacteria membranes. Melittin generated a Pn3m cubic phase with lattice parameter a = 18.2nm, and magainin-2 generated a Pn3m cubic phase with lattice parameter a = 17.9nm. Therefore, α-helical antimicrobials with little homology to the β-sheet defensins can also induce saddle-splay membrane curvature.

3.4 Conclusions

The saddle-splay curvature selection rule is consistent with different mechanisms of barrier disruption such as budding, blebbing, pore formation, vesicularization. However, as described in section 1.4.3, many AMPs have additional antimicrobial functions other than membrane permeation. For example, indolicidin [237], buforin [82], and tachyplesin [126] are also known to bind internal targets in bacteria such as DNA. Mammalian α- and β-defensins, and cathelicidin LL-37 play other important functions in host defense including modulation of the innate immune response and wound repair [76, 238]. A necessary and sufficient condition for membrane disruption is not a necessary and sufficient condition for full antimicrobial activity, which may involve other mechanisms such as DNA binding. (They may share related amino acid requirements, since both membrane activity and DNA bind-

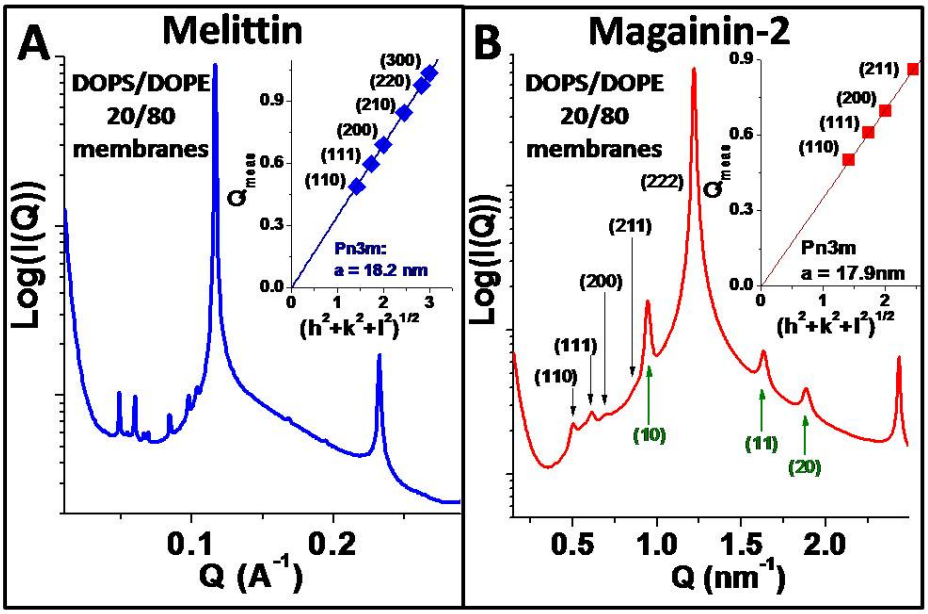

Figure 3.10: α-helical antimicrobial peptides can generate negative Gaussian curvature. In DOPS/DOPE = 20/80 membranes both melittin (A) and magainin-2 (B) restructured SUVs into cubic phases. At P/L = 1/40 melittin induced the Pn3m phase, while coexisting Pn3m and inverted hexagonal (indexes in green, lattice spacing 7.7nm) phases were induced by magainin-2 at P/L = 1/60.

ing require high cationic charge density.) It should be noted however, that AMPs which kill bacteria by binding to interior elements must first permeabilize the cytoplasmic bacterial membrane to reach the target. Since negative Gaussian curvature is topologically required for pore formation we expect the saddle-splay curvature selection rule should also apply to non-lytic AMPs provided that membrane permeation is necessary for their function, even if it isn't a sufficient condition for full activity.

In a more general context, the saddle-splay curvature selection rule we propose does not strongly restrict the amino acid content of an AMP, since it affects only the arginine, lysine, and hydrophobic residues. Membrane destabilizing AMPs therefore inherently have significant sequence flexibility for beneficial mutations. Consistent with this observation, it is known that AMP amino acid sequences are fairly non-conserved and labile across species [14]. However, when they acquire specific functions, such as Fe homeostasis activity in the hepcidins [239], their sequences tend to stabilize. That 1080 known AMPs are consistent with the saddle-splay curvature selection rule suggests that they all have some degree of membrane curvature generating activity, but since the selection rule under-determines the full sequence, there is potential for AMPs to acquire new functions, such as optimized DNA binding.

The saddle-splay curvature selection rule ultimately originates from geometry, so the amino acid composition trends are expected to be general for a broad range of membrane-active peptides. For example, the fusion protein M2 from the influenza virus induces in vitro cell membrane budding and scission. It contains a 17 residue amphipathic helix with comparable amino acid content to AMPs and is capable of inducing budding in GUVs [240]. During virion release M2 localized to the neck of budding virions, the region of maximal negative Gaussian curvature [171, 240]. This suggests other membrane-active peptides and proteins utilize similar strategies to generate curvature in membranes.

In summary, we show that a broad range of defensins and α-helical peptides selectively permeate bacterial membranes by inducing saddle-splay membrane curvature in a manner

that depends on target membrane lipid composition. Since the presence of saddle-splay curvature is necessary for membrane-disrupting processes, generation of saddle-splay membrane curvature by AMPs is a versatile mechanism of action. A saddle-splay curvature selection rule that places strong constraints on the amino acid composition of membrane disruptive peptides is deduced. We believe this rule can guide the rational design of antimicrobials.

3.5 Acknowledgements

We thank Michael M. Kozlov, Karl Lohner, Tom Ganz, and William DeGrado for useful discussions and suggestions. X-ray work was performed at the Stanford Synchrotron Radiation Lab (SSRL), the Advanced Photon Source (APS), and at the Fredrick Seitz Materials Research Laboratory (FS-MRL, Urbana, IL). SSRL is supported by DOE and NIH. Use of the APS is supported by DOE DE-AC02-06CH11357. This work is supported by NIH grants R01DK044632 and R01AI059346 (A.J.O.), NIH grants R37AI022931, RO1AI058129, and RO1DE15517 (MES), NIH grants P50 HL-61234 and P01 HL-091842 and the Roy J. Carver Charitable Trust (PBM), NIH grant 1UO1 AI082192-01 and NSF grants DMR-0409769 and WaterCAMPWS (GCLW).

3.6 Supporting Information

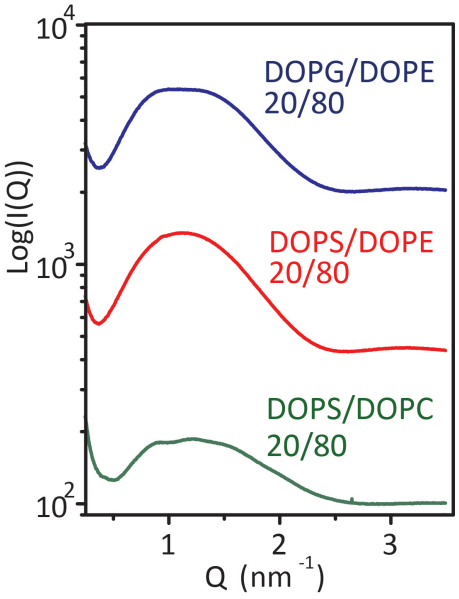

Figure S1: SAXS measurements on membranes used in this study show broad features consistent with the form factor from lipid bilayers indicating the presence of SUVs. Samples are in 100mM NaCl solution. Figure from [190].

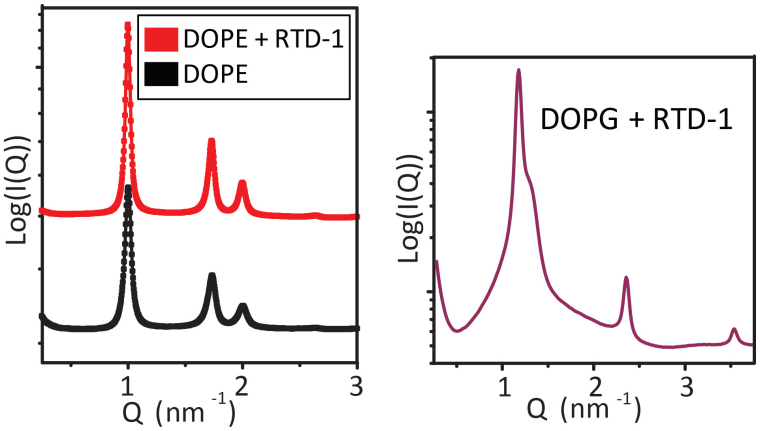

Figure S2: RTD-1 interacts differently with different lipid species. Virtually identical scattering profiles for DOPE only and DOPE+RTD-1 demonstrate RTD-1 weakly interacts with DOPE, and does not drastically reorganize DOPE lipids. RTD-1 strongly interacts with DOPG, and mediates adhesion between DOPG membranes into a Lα lamellar phase with d = 5.3nm. Replacement of DOPG with DOPS gives similar results. Since RTD-1 generates a Pn3m cubic phase only in composite DOPG:DOPE membranes this indicates both lipids play an essential role in curvature generation. Figure from [190].

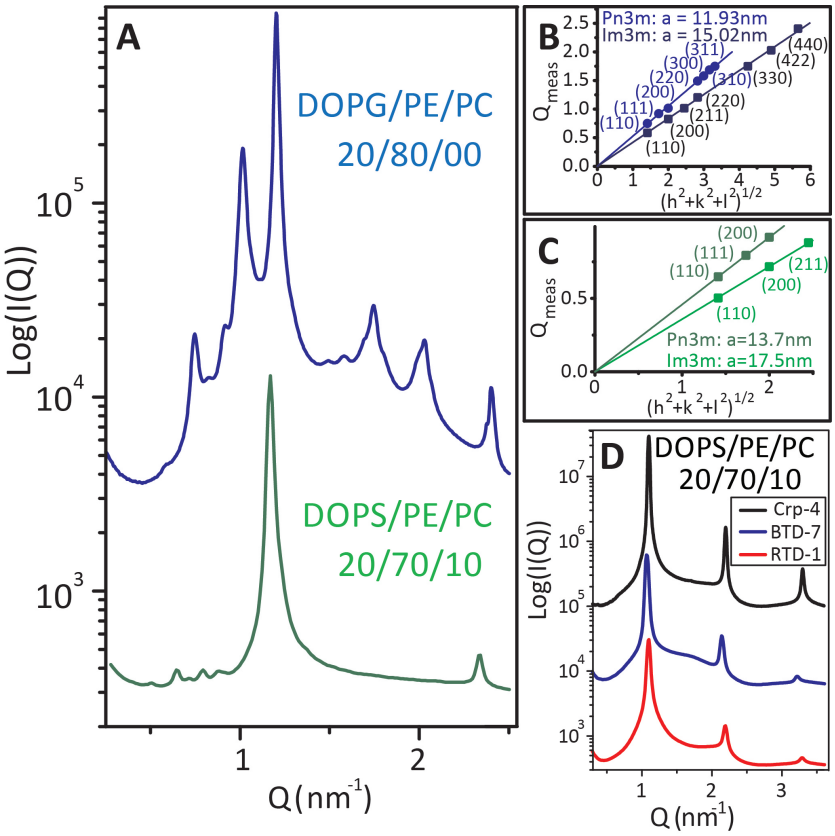

Figure S3: Generation of negative Gaussian curvature by protegrin-1 requires less membrane PE content. Protegrin-1 (PG-1) is an 18 amino acid amphipathic cathelicidin which resembles θ-defensins both sequentially and structurally. All six of its cationic residues are arginine, and its sheet structure is largely conferred from two intra-disulfide bonds from four cysteine residues. (A) PG-1 restructures vesicles with high amounts of PE, DOPG/DOPE = 20/80, and reduced amounts, DOPS/DOPE/DOPC = 20/70/10, into coexisting Pn3m and Im3m cubic phases. For the 80% PE condition (B), a_{Pn3m} = 11.91 nm and a_{Im3m} = 15.02 nm, with ratio $a_{Pn3m}/a_{Im3m} = 1.26$, which is close to the Bonnet ratio of 1.279 for coexisting cubic phases, and (C) a_{Pn3m} = 13.7 nm and a_{Im3m} = 17.5 nm, for the 70% PE condition (C). The calculated lattice parameters, a, for the coexisting cubic phases show a increases with decreasing PE. Since a is inversely related with the amount of negative Gaussian curvature, K, this implies large K is easier to produce in PE rich membranes. (D) None of the defensins measured at DOPS/DOPE/DOPC = 20/70/10 induced a cubic phase. Crp-4, BTD-7, and RTD-1 generate lamellar phases, d = 5.7nm, 5.9nm, and 5.7nm, respectively, with zero Gaussian curvature in membranes with reduced PE. The lower threshold PE concentration necessary for PG-1 to generate cubic phases may explain its reduced specificity compared with defensins. P/L = 1/30, for PG-1, RTD-1, and BTD-7, and 1/45 for Crp-4. Figure from [190].

Chapter 4

Saddle-Splay Curvature Generation Tracks With Antimicrobial Activities of R→K Variant α-Defensins

4.1 Introduction

Mammalian α-defensins are an important mediator of the host innate immune response. Their common characteristics include ∼4kDa size, a β-sheet secondary structure conferred by three invariant disulfide bonds via cysteine residues, cationic net charge and amphipathic character [77, 76, 75]. Activity assays have demonstrated that, *in vitro*, α-defensins display collective broad spectrum microbicidal activity against a variety of pathogens including Gram-positive and Gram-negative bacteria [241, 211, 242], fungi [243], protozoa [244] and enveloped viruses [194]. While some α-defensins have adopted additional indirect roles in the immune response [131, 132, 141], most are directly antibacterial. An established mechanism for the direct antibacterial effects of α-defensins is selective membrane disruption [245, 246, 247] which leads to permeation, depolarization, leakage, and eventual cell death.

In Chapter 3 it was shown that the membrane curvature deformations produced by defensins were sensitive to lipid composition. Defensins selectively generated membrane destabilizing saddle-splay curvature only in model bacteria membranes. Furthermore, arginine, lysine, and hydrophobicity are the curvature generating ingredients in a defensin. Therefore, membrane curvature depends on both the biophysical properties of the membrane and the cationic and hydrophobic properties of the defensin. Defensin sequences have been naturally engineered to produce disruptive mechanisms such as pore formation in the membranes of deleterious microbes. The idea of a 'sweet spot' for membrane disruption necessarily implies

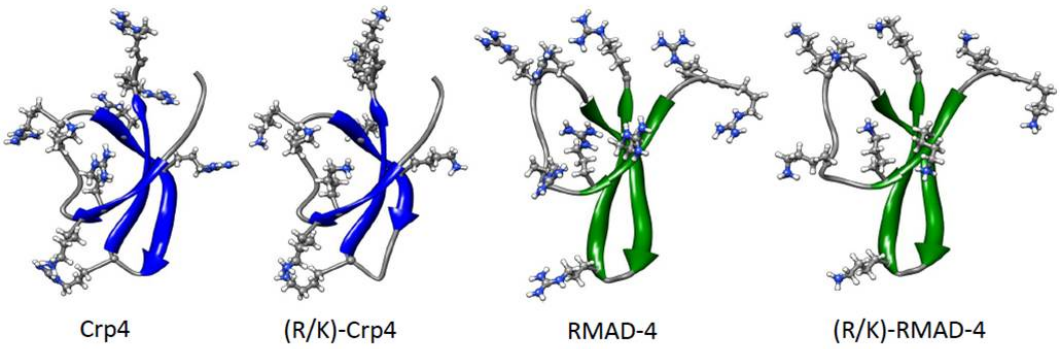

Figure 4.1: Ribbon model of the α-defensins used in this study. Wild type Crp4 and (R/K) Crp4 are shown on the left, and RMAD4 and (R/K) RMAD4 are on the right. Cationic amino acids are depicted using ball and stick form. Used with permission from K. Tai.

sequence optimization by tailoring the destabilizing curvature deformations produced by a defensin to coincide with microbial membrane compositions. It is therefore expected that certain alterations of defensin sequence and structure will shift the sweet spot for maximal membrane disruption.

In a recent study Llenado *et al* [211] showed that lysine for arginine substitutions in two different broad spectrum antimicrobial α-defensins, crytpdin-4 (Crp4) from mouse and rhesus myeloid α-defensin-4 (RMAD4), had different effects on their *in vitro* microbicidal profiles. In Crp4, R$\rightarrow$K replacements generally attenuated activity, while the effects of analogous substitutions in RMAD4 ranged from having a neutral effect to modestly improving activity against certain bacteria. Since both α-defensins are known to permeabilize lipid membranes, these results provide a baseline to understand how well variations in defensin bactericidal activity are tracked by the curvature deformations these peptides induce in model membranes.

In this chapter we use synchrotron small-angle x-ray scattering (SAXS) to characterize the lyotropic liquid crystalline phases that wild type and R$\rightarrow$K variants of α-defensins Crp4 and RMAD-4 induce in model liposomes. By varying the biophysical properties of the membrane through changes in lipid composition we probe the curvature deformations produced

by each α-defensin as a function of both the membrane properties and peptide arginine and lysine content. The resulting defensin-lipid membrane phase diagrams are then compared with microbicidal assays to examine the relationship between the molecular length scale curvature deformations defensins generate in membranes and their killing abilities. We show the curvature deformations induced by both defensins agree with their bactericidal activities. In Crp4, R→K substitutions drastically changed the phase behavior, whereas R→K substitutions in RMAD4 had little effect on curvature generation. Our results provide an explanation for the differences that lysine for arginine substitutions have on the killing abilities of these α-defensins.

4.2 Results

4.2.1 R→K substitution in Crp4 drastically shifted cubic phase generation to membranes with reduced DOPE content

Small unilamellar vesicles were prepared with membranes composed of negatively charged DOPS and zwitterionic DOPE and DOPC lipids and then incubated with α-defensins. Since the spontaneous curvatures (c_0) of both DOPS and DOPC are approximately zero, while DOPE has $c_0 < 0$, ternary mixtures of these lipid types allow the membrane anionic surface charge density and monolayer spontaneous curvature to be independently varied. It is believed that distribution differences of the lipids found in the membranes of microbes compared with host cells, such as increased amounts of both anionic lipids and negative spontaneous curvature lipids in bacterial plasma membranes, allow defensins to specifically target microbial membranes [14].

Representative spectra of the WT Crp4 and the lysine for arginine substituted Crp4 mutant defensin (R/K) Crp4, are shown in Figure 4.2A. Both Crp4 and (R/K) Crp4 induced a variety of structure factor correlation peaks indicating both peptides substantially

restructured DOPS/DOPE/DOPC membranes. Furthermore, the observed liquid crystalline phases strongly depend on membrane lipid composition. In DOPS/DOPE/DOPC = 20/60/20 membranes (Figure 4.2A) Crp4 induced reflections with peak Q positions at ratio 1:2, indicating Crp4 reorganized 60% DOPE liposomes into multi-lamellar phases with lattice spacing d = 5.80nm. Multi-lamellar phases consist of stacks of locally flat membranes in which the Crp4 is likely intercalated between adjacent bilayers. In membranes with increased amounts of negative spontaneous curvature lipids, DOPS/DOPE = 20/80, two additional sets of correlation peaks appear with ratios $1 : \sqrt{3} : \sqrt{4} : \sqrt{7}$ and $\sqrt{2} : \sqrt{3} : \sqrt{4} : \sqrt{6} : \sqrt{8}$, indicating the presence of coexisting inverted hexagonal and Pn3m cubic phases. By relating the measured Q peak positions to their Miller indices h, k, l, for each phase, $Q^{Hex}_{meas} = (4/\sqrt{3})\sqrt{(h^2 + k^2 + hk)}/a$, and $Q^{Cube}_{meas} = 2\sqrt{(h^2 + k^2 + l^2)}/a$, the lattice parameters are calculated via linear trendline fit to be $a_{Hex} = 7.68$nm and $a_{Pn3m} = 16.40$nm for the inverted hexagonal and Pn3m cubic phases, respectively.

The Pn3m is a bicontinuous 'double-diamond' cubic phase where the lipid bilayer divides space into two non-intersecting tetrahedral water channels. The center of the bilayer, where the tail regions of the constituent lipid monolayers meet, traces out a minimal surface which has zero mean curvature and negative Gaussian curvature at every point. In other words, any point on a minimal surface has principle axes of curvature $c_1 = -c_2$, so the mean curvature, $H = \frac{1}{2}(c_1 + c_2) = 0$, while the Gaussian curvature, $K = c_1 c_2 < 0$. Geometrically, the surface will curve upwards in one direction and downwards in the perpendicular direction, locally giving it the shape of a saddle. Negative Gaussian (or equivalently saddle-splay) curvature is found in the interior of a toroidal pore, at the 'neck' of membrane budding events, as well as at the base of membrane blebs and other protrusions. Since it is topologically necessary for different membrane destabilization processes, generation of negative Gaussian curvature by Crp4 is a potent mechanism to disrupt the barrier function of cell membranes. Like the Pn3m, the inverted hexagonal, H_{II}, is also a non-lamellar phase. The H_{II} is a two dimensional lattice of hexagonally coordinated cylindrical tubes. Each tube consists of a

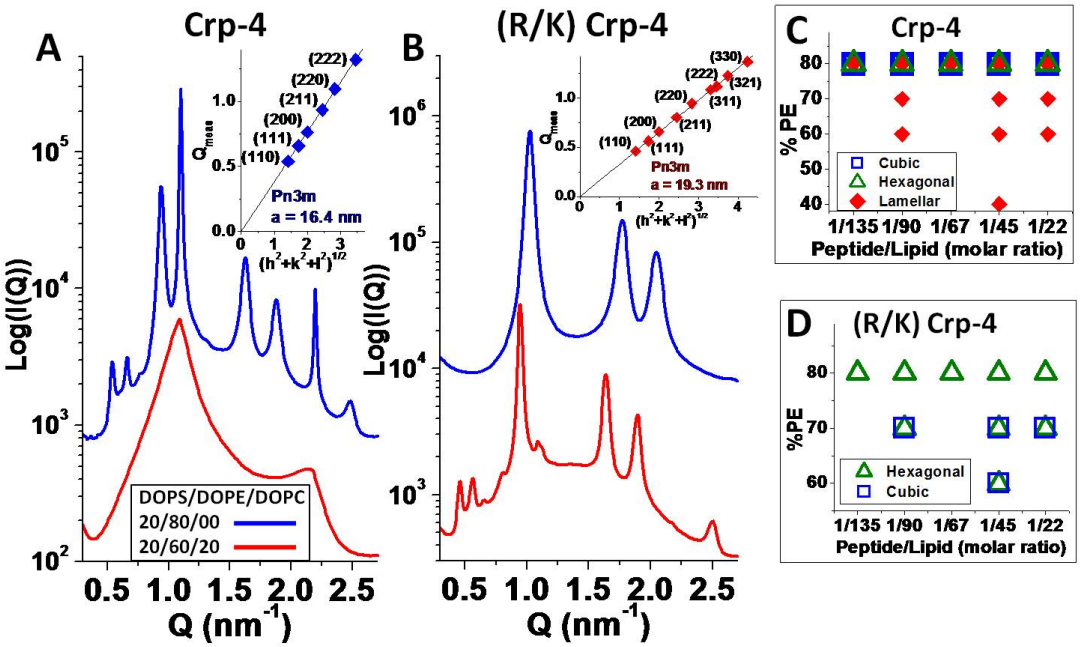

Figure 4.2: Small-angle x-ray scattering showed substitution of lysine for arginine in the α-defensin cryptdin-4 (Crp-4) substantially changed phase behavior. A. Crp-4 induced non-lamellar cubic (a = 16.4nm) and inverted hexagonal (a = 7.74nm) phases in PE-rich DOPS/DOPE = 20/80 membranes, but not in membranes with reduced amounts of negative intrinisic curvature lipids B. (R/K) Crp-4 generated a pure inverted hexagonal phase (a = 7.09nm) at DOPS/DOPE = 20/80, and coexisting cubic (a = 19.3nm) and inverted hexagonal (a = 7.68nm) phases in DOPS/DOPE/DOPC = 20/60/20 membranes. Scattering spectra in A & B are at peptide/lipid = 1/45 molar ratio except for Crp-4 at DOPS/DOPE which is at P/L = 1/67. The insets show indexation of the Pn3m cubic phases. C and D. DOPS/DOPE/DOPC = 20/x/(80-x) phase diagrams where x = %DOPE, for Crp-4 and (R/K) Crp-4, respectively. Replacing arginine with lysine in Crp-4 decreased the threshold PE concentration necessary to produce non-lamellar cubic and inverted hexagonal phases.

central water channel that is wrapped by a lipid monolayer. The monolayer is oriented such that the lipid headgroups remain hydrated. Since the lipid monolayer bends toward the water along the direction of wrapping, $c_1 < 0$, and is flat along the tube axis, $c_2 = 0$, H_{II} phases have negative mean curvature and zero Gaussian curvature at every point.

Figure 4.2B shows the analogous scattering spectra for (R/K) Crp4. In membranes with lipid composition DOPS/DOPE = 20/80, (R/K) Crp4 induced a pure inverted hexagonal phase with lattice parameter a = 7.09nm, indicating that the lysine-rich variant peptide generated only negative mean curvature in membranes enriched in negative spontaneous curvature lipids. When the membrane DOPE content was decreased to DOPS/DOPE/DOPC = 20/60/20, coexisting Pn3m cubic, a = 19.3nm, and inverted hexagonal phases, a = 7.68nm, were observed. Therefore, (R/K) Crp4 generated negative Gaussian curvature in membranes with reduced amounts of negative spontaneous curvature lipids.

Comparisons of the phase diagrams of Crp4 (Figure 4.2C) and (R/K) Crp4 (Figure 4.2D) reveal the drastic effect replacement of arginine with lysine has on the curvature generating abilities of Crp4 α-defensin. For Crp4, non-lamellar cubic and inverted hexagonal phases are observed only at the highest membrane 80% DOPE composition, consistent with previous reports on its phase behavior [190]. At lower PE content flat membrane multilamellar phases are seen, indicating > 70% DOPE is necessary to induce non-zero curvature phases. Conversely, (R/K) Crp4 generated both negative Gaussian curvature and negative mean curvature in membranes with DOPE as low as 60%. While coexisting cubic, inverted hexagonal, and multi-lamellar phases are present at 80% DOPE for Crp4, (R/K) Crp4 induced only an inverted hexagonal phase. In ternary DOPS/DOPE/DOPC = 20/x/(80-x) membranes the phase progression produced by Crp4 with increasing x = DOPE% is $L_\alpha \rightarrow Q_{II} \rightarrow H_{II}$, similar to that found in temperature studies on lyotropic systems [248, 249, 250, 50]. The effect of R→K substitution in Crp4 is to reduce the amounts of negative spontaneous curvature lipids that are required for topological transitions to non-lamellar phases.

4.2.2 R→K replacements in RMAD4 did not substantially change phase behavior

To see if lysine for arginine replacements have similar effects on other α-defensins we performed comparable experiments on the α-defensin RMAD4. Representative spectra for wild type RMAD4 are shown in Figure 4.3A. Coexisting Pn3m, a = 13.3nm, and Im3m, a = 17.0nm, cubic phases in addition to an inverted hexagonal phase, a = 7.44nm, were generated at DOPS/DOPE = 20/80 membrane compositions demonstrating that RMAD4 also induces negative Gaussian curvature and negative mean curvature in membranes rich in PE. Like the Pn3m, the Im3m 'plumber's nightmare' is a bicontinuous cubic phase where the lipid bilayer mid-plane traces out a minimal surface which divides space into two non-intersecting water channels. However, their morphologies differ. For example, in the Im3m the water channel junctions have six vertices, different from the tetrahedrally coordinated (four vertices) water channel junctions of the Pn3m. The ratio of the Im3m and Pn3m lattice parameters $a_{Im3m}/a_{Pn3m} = 1.278$, is close to the theoretically predicted Bonnet ratio of 1.279, indicating both cubic phases have identical negative Gaussian curvature distributions on their surfaces which is expected for coexisting phases. When the membrane negative spontaneous curvature lipid composition is reduced to DOPS/DOPE/DOPC = 20/60/20, the non-lamellar phases disappear and are replaced by a multi-lamellar phase with lattice spacing d = 6.99nm (Figure 4.3A). Therefore, like Crp4, RMAD4 only generates negative Gaussian curvature and negative mean curvature in membranes with elevated levels of DOPE.

The spectra for (R/K) RMAD4 closely resemble the wild type peptide (Figure 4.3B). In DOPS/DOPE = 20/80 membranes (R/K) RMAD4 generated coexisting Pn3m, a = 18.2nm, and inverted hexagonal, a = 7.42nm, phases. The Pn3m cubic phase lattice parameter for RMAD4 is smaller than for (R/K) RMAD4 (13.3nm versus 18.2nm). Since the average negative Gaussian curvature, $\langle K \rangle$, is inversely proportional to the square of the lattice parameter,

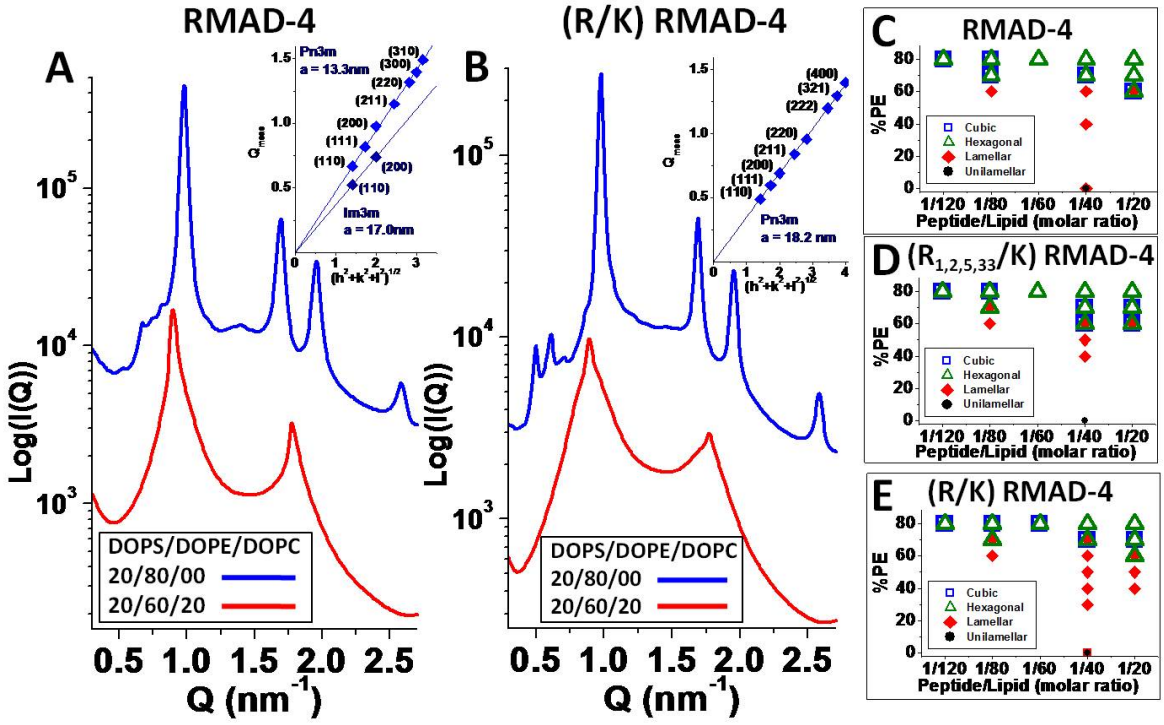

Figure 4.3: Lysine for arginine substitutions in the α-defensin RMAD4 did not significantly affect phase behavior. A. Small angle x-ray scattering spectra showed that RMAD4 generated coexisting non-lamellar cubic (Pn3m a = 13.3nm, Im3m a = 17.0nm) and inverted hexagonal (a = 7.42nm) phases in DOPS/DOPE = 20/80 membranes but not in membranes with reduced amounts of DOPE. B. (R/K) RMAD4 also generated non-lamellar cubic (Pn3m a = 18.2nm) and inverted hexagonal (a = 7.42nm) phases in PE-rich membranes just like wild type RMAD4. Spectra in A & B are at peptide/lipid = 1/80 molar ratio, and the insets show indexation of the cubic phases The phase diagrams of RMAD-4, C, (R/K) RMAD4, E, and an α-defensin with intermediate R→K, ($R_{1,2,5,33}/K$) RMAD-4, D, are very similar. This indicates that, unlike Crp-4, replacement of arginine with lysine in RMAD-4 has little effect on the curvature generating abilities on RMAD4. Phase diagrams in C, D, & E, are DOPS/DOPE/DOPC = 20/x/(80-x) where x = %DOPE.

this indicates that R→K substitution decreased the amount of negative Gaussian curvature generated by RMAD4. However, the phase behavior of the two peptides is very similar; they both induce negative Gaussian and negative mean curvature in PE-rich membranes. Furthermore, multi-lamellar phases with lattice spacing, d = 7.04nm are observed for (R/K) RMAD4 and DOPS/DOPE/DOPC = 20/60/20 membranes (Figure 4.3B), similar to WT RMAD4. These results indicate that substitution of lysine for arginine has much less effect on the membrane curvature deformations produced by RMAD4 than for Crp4.

Figure 4.3C-E shows the phase diagrams for RMAD4, (R/K) RMAD4, and a peptide with partial R→K substitutions in sequence positions 1, 2, 5, and 33, ($R_{1,2,5,33}/K$) RMAD4. Like in the Crp4 and (R/K) Crp4 phase diagrams, the general phase progression of $L_\alpha \rightarrow Q_{II} \rightarrow H_{II}$ with increasing DOPE membrane content is also seen for the RMAD4 peptides. Moreover, the peptide to lipid (P/L) ratio also affects phase behavior as increasing the P/L tends to promote non-lamellar cubic and hexagonal phases. However, in striking contrast to Crp4 peptides, R→ K substitutions do not significantly affect the phase behavior of the RMAD4 peptides. For all three peptides, the presence of non-zero curvature phases begins around 60% DOPE content. Cubic and inverted hexagonal phases rich in negative Gaussian curvature and negative mean curvature, respectively, dominate at 70% and 80% DOPE. Taken together, the x-ray data show that while R→K substitutions drastically change the membrane curvature deformations induced by Crp4, similar cationic residue substitutions in RMAD4 have little effect on its membrane curvature generating abilities.

4.3 Discussion and Conclusion

All the defensins examined in this study induced non-lamellar cubic phases and inverted hexagonal phases specifically in membranes enriched in PE lipids, compositions that resemble bacterial cell membranes. Since negative Gaussian curvature is topologically required for a number of membrane destabilization processes, generation of negative Gaussian curvature

membrane deformations is a potent way to disrupt cell membranes. Negative mean curvature is a necessary condition but not a sufficient condition for negative Gaussian curvature. However, negative mean curvature membrane deformations are also topologically active, which implies these curvature deformations likely assist in membrane disruption. Indeed, previous studies have shown a correlation between the antibacterial activity of synthetic and natural membrane active antimicrobials and their ability to induce inverted hexagonal phases in liposomes [104, 105, 106]. By specifically generating membrane destabilizing negative Gaussian curvature and negative mean curvature in model bacterial membranes, Crp4 and RMAD4 and their R→K variants exploit innate compositional differences between the membranes of bacteria and eukaryotic cells that render bacteria membranes more vulnerable to disruption.

How might the observed changes in the curvature deformations from R→K substitutions in Crp4 lead to attenuated bactericidal activity? An important function of Crp4 in innate host defense is selective membrane disruption, so its composition is likely under positive selection for potent membrane activity against bacterial membranes. Altering the Crp4 sequence with R→K substitutions necessarily alters how it deforms membranes because arginine and lysine generate different types of membrane curvature. The curvature producing abilities of (R/K) Crp4 are not matched with bacterial membranes so they are no longer able to optimally destabilize them. The negative Gaussian curvature generation 'sweet spot' has shifted out of the bacterial membrane region to lower amounts of membrane PE. In the membrane lipid compositions where Crp4 generated negative Gaussian curvature, (R/K) generates negative mean curvature. The result is a peptide which retains activity yet is attenuated compared to the wild type.

The shift of non-lamellar phase generation by (R/K) Crp4 to membranes with reduced amounts of negative intrinsic curvature lipids is due to the differing curvature generating tendencies of arginine and lysine. Arginine can generate negative Gaussian curvature while lysine can only generate negative mean curvature. The effect of R→K substitution in Crp4 is to remove positive curvature. Therefore, inverted hexagonal phases are observed instead

of cubic phases in PE-rich bacterial membranes for (R/K) Crp4. Since PE is a negative spontaneous curvature lipid it reduces the energetic penalty of wrapping membranes into inverted hexagonal phases. Less membrane PE content makes it harder to wrap, which is why cubic phases appear at lower membrane PE concentrations. The differences between the dependence of Crp4 on arginine for generating negative Gaussian curvature, and the indifference of RMAD4 to R→K substitutions is likely due to how the molecules present their cationic charge when interacting with membranes. The surface distribution of the arginines in Crp4 is confined to one face of the molecule that runs along the major axis, while the arginines in RMAD4 are mostly confined to one face along the minor axis (Figure 4.1). If the interaction of the guanidine group of arginine with lipid headgroups is sufficiently obstructed, its bidentate hydrogen bonding ability may diminish to the point that it behaves like lysine.

In summary our results establish a connection between the killing abilities of α-defensins and the curvature deformations they induce in membranes. The changes in phase behavior due to R→K substitutions in Crp4 and RMAD4 track with their *in vitro* microbicidal profiles. Replacement of lysine for arginine generally attenuated Crp4 bactericidal activity. X-ray characterization of Crp4 and (R/K) Crp4 showed that the lysine-rich mutant generated topologically active curvatures over a different range of lipid compositions compared to the wild type, implying its curvature generating abilities are no longer optimized for killing bacteria. Differently, the bacterial killing abilities of RMAD4 and (R/K) RMAD4 ranged from being the same to slightly better for the lysine-rich version. The phase diagrams of RMAD4, (R/K) RMAD4, and ($R_{1,2,5,33}/K$) RMAD4 are highly similar indicating that R→K substitutions have minor effect the membrane curvature deformations produced by this α-defensin. Since variations in α-defensin bactericidal activities show good correspondence with their phase behaviors, we believe the curvature generating tendencies of membrane active antimicrobials are useful predictors of AMP activity.

4.4 Materials and Methods

4.4.1 Liposome preparation for x-ray measurements, and SAXS experiments

Liposomes were prepared as described in section 3.2.2. X-ray samples were prepared and measured as described in section 3.2.3 except for the following changes. All samples were prepared in 100mM NaCl solution. SAXS experiments were collected at Stanford Synchrotron Radiation Laboratory (BL4-2). The scattered radiation was collected using a Rayonix MX225-HE detector (pixel size, 73.2μm).

Chapter 5

Investigation of the Membrane Activities of Guanidine-Rich Molecular Transporters and Antimicrobials Based Upon Saddle-Splay Curvature Generation

5.1 Introduction

Utilization of arginine to help confer strong interactions with cell membranes is found in a number of membrane-active peptides and proteins. For example, hydrophilic arginine-rich cell penetrating peptides (CPP) such as the TAT peptide from the HIV transactivator protein TAT can efficiently translocate across cellular membranes [185, 188, 251, 222, 252, 253]. And certain classes of antimicrobial peptides (AMPs) like amphipathic α- and θ- defensins from mammals, which display potent in vitro activity against bacteria via membrane permeabilization, overwhelmingly use arginine over lysine [75, 76, 77]. Due to their biological relevance and complex interactions with cell membranes much scientific effort has gone into understanding the observed structure-function relationships between arginine-rich peptides and biomembranes.

There is substantial evidence that the unique membrane interacting properties of arginine are due to its guanidine side chain. In cell penetrating peptides, previous studies have shown that cationic charge is a necessary but not a sufficient condition for activity. While poly-arginine can enter cells similar length lysine, histidine, and ornithine peptides all showed poor transduction ability [187, 186, 188]. Heptamers of cationic citrulline, an isotere of arginine with a single oxygen for nitrogen replacement in the guanidine group also cannot enter

cells [187]. Identification of a guanidinium functional group as the essential part of arginine for cell-penetrating ability initiated development of a variety of synthetic guanidinium-rich oligomers, many of which display better uptake than their peptidic relatives. Oligoarginine peptoids were more efficient at entering cells than oligoarginine peptides [186]. Faster uptake was observed for guanidinium-rich oligocarbamates than TAT peptide [254]. Polyguanidino dendrimers based on diamino acid monomeric units were also taken up by cells [255], and carbohydrate-based polymers like guanidinylated neomycin can penetrate cells and deliver bioactive macromolecules [256]. These results not only implicate the importance of the guanidinium group, they also demonstrate that synthetic oligomers containing guanidinium have a rich potential for applications such as drug delivery vectors and antibiotics.

Chapters 2&3 discussed how arginine is unique in its ability to generate destabilizing membrane curvatures. The strong electropositive charge along with the planer Y-shape structure of guanidine [221] equips arginine with the ability to generate complementary types of membrane curvature. Multivalent cations such as poly-arginine generally promote electrostatic wrapping of anionic membranes, while the structure of guanidine supports multi-dentate hydrogen bonding with multiple lipid headgroups [257, 221]. Membrane wrapping in concert with lipid headgroup organization via multi-dentate hydrogen bonding produce the requisite negative and positive curvature strains, respectively, to permeabilize membranes by generating topologically active negative Gaussian (equivalently saddle-splay) curvature.

Since positive curvature strain by lipid headgroup organization depends on the spatial arrangement and coordination of the guanidinium groups, varying these parameters should affect the curvature generating abilities of guanidine-rich molecules. The first part of this chapter investigates saddle-splay curvature generation by guanidine homopolymers of different lengths and average monomer spacings. We use small-angle x-ray scattering to characterize the membrane curvature deformation modes produced by polyguanidine-oxanobornene homopolymers (PGONs) (Figure 5.1), a synthetic class of molecular transporters with similar features to arginine-rich cell-penetrating peptides [258]. The presentation of the guanidinium

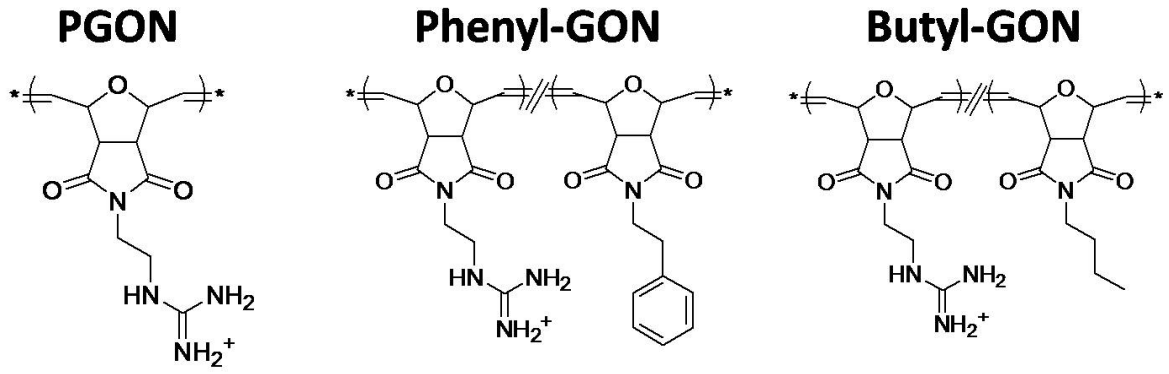

Figure 5.1: The polymers used in this study. Left: the polyguanidine-oxanobornene homopolymer (PGON). Middle: phenyl-guanidine random copolymer (phenyl-GON). Right: butyl-guanidine random copolymer (butyl-GON). Used with permission from M. Lis.

groups in PGON polymers and poly-arginine CPPs differ owing to their different backbones. We conduct a detailed investigation on the polymer length dependence of saddle-splay curvature generation by PGON and compare the trends with similar experiments on poly-arginine. We find that both polymers generate maximum saddle-splay curvature at intermediate degree of polymerization, and the number of repeating units required for maximal saddle-splay curvature depends on inter-guanidine spacing.

Amphipathic arginine-rich peptides are commonly deployed as antimicrobial agents in the host defense. Collectively, the sequences of antimicrobial peptides follow the saddle-splay curvature selection rule (see Chapter 3): the functional requirement of generating saddle-splay curvature constrains the arginine, lysine, and hydrophobic content in the form of a compositional trade-off between the relative amounts of arginine and lysine plus hydrophobicity used in a peptide. The amino acid compositions of cell penetrating peptides also follow the saddle-splay curvature selection rule (Figure 5.2) [259]. However, on average the antimicrobials use greater amounts of hydrophobicity. This implies that a cell-penetrating peptide can be turned into an antimicrobial by systematically increasing its hydrophobicity. The second part of this chapter investigates how the inclusion of hydrophobic residues into a guanidine-rich polymer affects its curvature generating abilities. Amphiphilic phenyl-

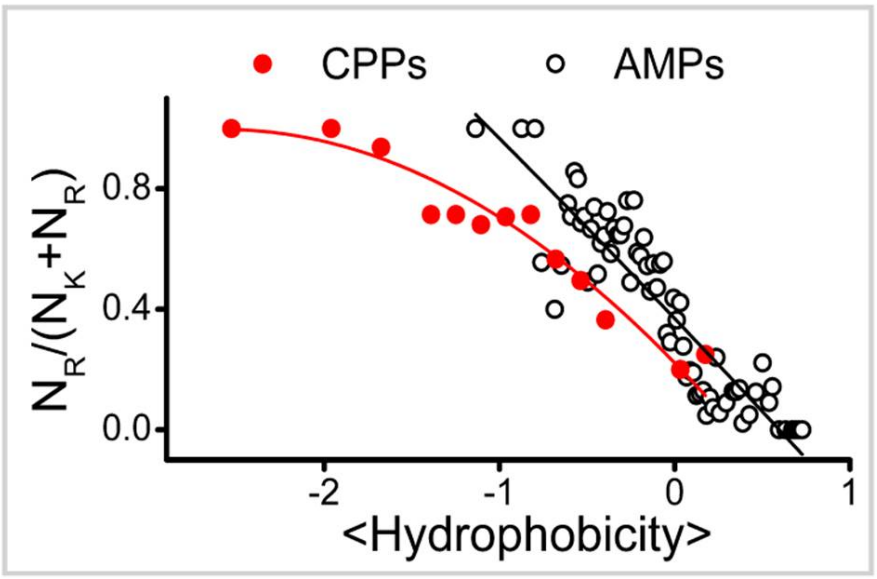

Figure 5.2: The saddle-splay curvature selection rule, the trade-off between arginine with lysine plus hydrophobicity in a peptide, is observed in the sequences of both cell-penetrating peptides and antimicrobial peptides. In general, as the average hydrophobicity, $\langle Hydrophobicity \rangle$, of a membrane-active antimicrobial or cell-penetrating peptide increases the number of arginines it uses, N_R, decreases relative to the number of lysines, N_K. The cell-penetrating peptides are less hydrophobic than the antimicrobial peptides. Figure adapted from [259]

guanidine and butyl-guanidine random copolymers (Figure 5.1) were chosen since their membrane activities depend on degree of polymerization and on the ratio of monomeric species instead of their precise arrangement. Therefore, they are an ideal choice for examining the net effects of adding hydrophobicity to polyguanidine polymers. Small angle x-ray scattering is used to compare the membrane curvature deformations produced by amphiphilic phenyl- and butyl-guanidine polymers with those produced by PGON polymers of similar lengths. In general, incorporation of hydrophobicity into a guanidine-rich polymer enhances its saddle-splay curvature generating ability.

5.2 Results and Discussion

5.2.1 PGONs generate negative Gaussian curvature in a manner dependent on polymer degree of polymerization

PGON polymers were incubated with small unilamellar vesicles (SUVs), lipid composition DOPS/DOPE = 20/80, to mimic the rich anionic and negative spontaneous curvature lipid content of Gram-negative bacterial plasma membranes. PGON remodeled the SUVs into strongly scattering liquid crystalline structures as indicated by the appearance of multiple structure factor correlation peaks. Representative spectra for PGON polymers with average degree of polymerization $\langle N \rangle$ = 7, 18, 50 are shown in Figure 5.3A. For each polymer the scattering spectra contain peaks with Q positions at ratio $\sqrt{2} : \sqrt{3} : \sqrt{4}$, indicating the presence of Pn3m 'double-diamond' cubic phases. The Pn3m is a bicontinuous cubic phase where two non-intersecting tetrahedral water channels are separated by the lipid bilayer. The midpoint of the bilayer traces out a minimal surface which has zero mean curvature and negative Gaussian curvature at every point. Geometrically, minimal surfaces locally have the shape of a saddle; the surface will curve maximally upward and downward in perpendicular directions. Negative Gaussian curvature is ubiquitous in membrane destabilization processes. It is present in the interior of toroidal pores, as well as at the base of blebs and the 'neck' of budding events, all processes which destabilize and disrupt the barrier function of cell membranes. By relating the measured peak Q positions to their Miller indices h, k, l, for each reflection using the equation for a powder averaged cubic phase, i.e. $Q_{meas} = 2\pi\sqrt{(h^2+k^2+l^2)}/a$, we calculate lattice parameters $a_{\langle N \rangle=7}$ = 15.98nm, $a_{\langle N \rangle=18}$ = 14.98nm, and $a_{\langle N \rangle=50}$ = 17.99nm. Cubic phases were observed in PE-rich membranes for PGONs with $\langle N \rangle$ = 7, 9, 14, 18, 27, and 50, implying that generation of negative Gaussian curvature is a general feature of PGON polymers with $\langle N \rangle$ = 7-50.

The relationship between PGON length and cubic phase lattice parameter is non-monotonic (Figure 5.3A&B). A similar trend was previously seen for poly-arginine [259]. Since the

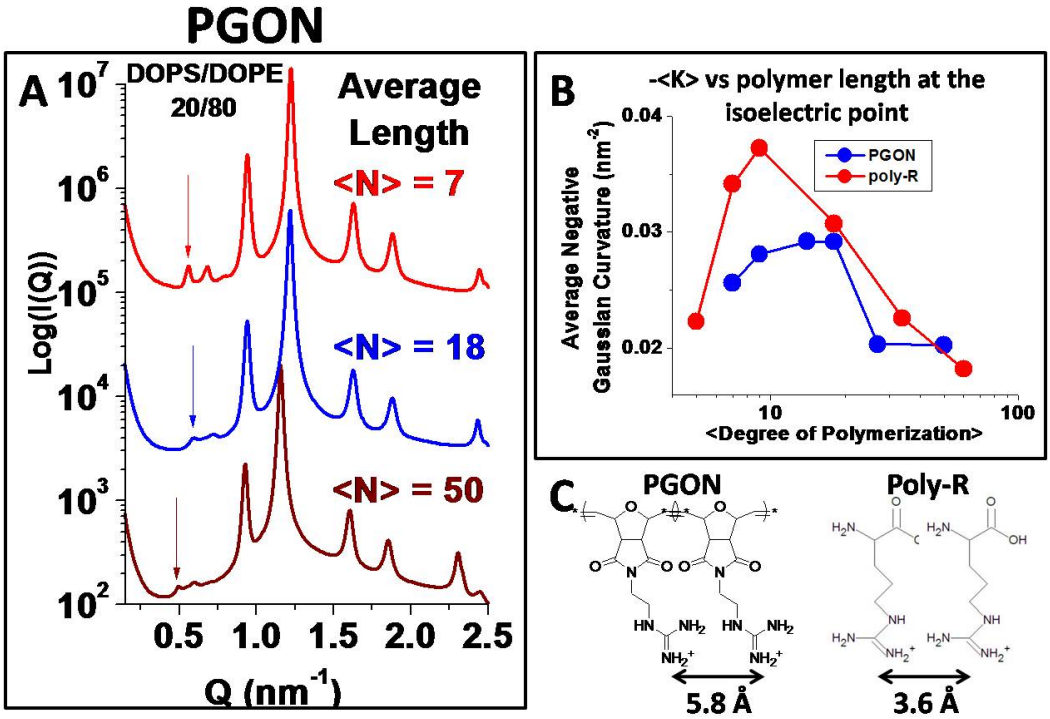

Figure 5.3: PGON polymer generation of negative Gaussian curvature depends on average polymer length and average spacing between monomers. A. Representative scattering spectra of PGONs with degree of polymerization 7, 18, & 50 (top to bottom) with DOPS/DOPE = 20/80 membranes at the polymer to lipid isoelectric point. Arrows indicate the first order reflection of the Pn3m cubic phase. A first order reflection at higher Q indicates the generation of greater negative Gaussian curvature. B. Plots of polymer-induced average negative Gaussian curvature generation, $-\langle K \rangle$, versus polymer length for both PGON and poly-arginine at the isoelectric point. The maximum amount of $-\langle K \rangle$ occurs around Arg_9 for poly-arginine, while for PGON it is around an average degree of polymerization of 14. C. Schematic showing structural features of PGON and poly-arginine, and effective spacing between guanidine groups.

minimal surface of a cubic phase has average negative Gaussian curvature (equation 1.9) $\langle K \rangle = 2\pi\chi/a^2 A_0$, where a is the cubic lattice parameter, χ is the Euler characteristic, and A_0 is the surface area per unit cell, the measured cubic lattice parameters can be used to extract the $\langle K \rangle$ values for PGON polymers of different lengths. The results are plotted in Figure 5.3B, along with the data from a similar analysis for poly-arginine. Both PGON and poly-arginine generate maximum $-\langle K \rangle$ at intermediate polymer lengths. However, the polymer length where maximum $-\langle K \rangle$ occurs for poly-arginine is around Arg_9, whereas for PGON the maximum is shifted outward to an average degree of polymerization of about 14. Since both PGON and poly-arginine consist solely of guanidine side-chains the differences in $\langle K \rangle$ versus polymer length must originate from the different structural properties of their backbones which necessarily influence how the guanidinium groups interact with membrane lipids.

Figure 5.3C shows the structures of PGON and poly-arginine. Polymerization of guanidinylated oxanorbornene monomers produces a guanidinium spacing of $5.8\mathring{A}$, approximately 60% larger than the $3.6\mathring{A}$ spacing in poly-arginine. The larger spacing in PGON along with its more shape-persistent scaffold compared to poly-arginine reveal that the average distance between guanidine side chains will be greater in PGON than poly-arginine [258]. As stated above saddle-splay curvature generation by guanidinium groups is the product of membrane wrapping to produce negative curvature and membrane buckling from multi-dentate hydrogen bonding with lipid headgroups to produce positive curvature. Membrane buckling occurs from the cooperative effort of multiple guanidinium groups. Increasing the average distance between guanidinium groups has the effect of relieving some of the membrane positive curvature strain. Since negative Gaussian curvature requires both positive and negative curvature a reduction in positive curvature will also reduce the amount of negative Gaussian curvature a polymer can generate. In principle, this can be compensated by increasing the polymer length, so that more guanidinium groups are concentrated in the area. However, the ability of the guanidinium groups to organize and coordinate lipid headgroups to coopera-

tively produce positive membrane curvature eventually breaks down. Indeed, polymers with lengths greater than the optimum value for negative Gaussian curvature generation appear to antagonize their efforts, since the amount of curvature generated decreases. Therefore, the stiffer PGON polymer with larger inter-guanidinium spacing requires more repeating units to maximize its negative Gaussian curvature generation compared with the more flimsy poly-arginine with its smaller spacing between guanidinium groups.

5.2.2 Incorporation of hydrophobicity into guanidinium-rich polymers increases the amount of negative Gaussian curvature they induce in membranes

To examine the effects adding hydrophobicity to guanidinium-rich polymers similar SAXS experiments were conducted with random copolymers consisting of guanidinium groups with either hydrophobic butyl or phenyl side chains. A general feature in the scattering spectra for both butyl-GON (Figure 5.4A) and phenyl-GON (Figure 5.4B) is the strong induction of the Pn3m cubic phase. At peptide/lipid, P/L = 1/60 molar ratio, sharp correlation peaks at Q positions with ratios, $\sqrt{2} : \sqrt{3} : \sqrt{4} : \sqrt{6} : \sqrt{8} : \sqrt{9} : \sqrt{10} : \sqrt{11} : \sqrt{12}$, are observed for both butyl-GON and phenyl-GON. By fitting the measured peak Q positions to their respective reflections via trendline fit (Figure 5.4C&D), we calculate Pn3m cubic lattice parameters a = 19.40nm for butyl-GON and a = 20.42nm for phenyl-GON at P/L = 1/60. When the polymer concentration is doubled to P/L = 1/30, similar spectra are observed (Figure 5.4 A&B). However, the cubic phase reflections have shifted to higher Q values, indicating greater polymer concentrations induce smaller cubic lattices. At P/L = 1/30 the lattice parameters shrunk to a = 14.38nm for butyl-GON (Figure 5.4C) and a = 15.42nm for phenyl-GON (Figure 5.4D). The cubic phase lattice parameter is inversely proportional (see above) to its average negative Gaussian curvature. Therefore, increasing the polymer concentration increases the amount of membrane negative Gaussian curvature,

as expected for polymers which generate such curvature. By plotting the average negative Gaussian curvature over a range of peptide to lipid ratios for polymers with similar lengths and net charge (Figure 5.4E), their abilities to generate curvature can be directly compared. Interestingly, $-\langle K \rangle$ seems to increase linearly with polymer concentration over the range tested. Furthermore, while roughly equivalent amounts of $-\langle K \rangle$ were generated by butyl-GON and phenyl-GON, both amphiphilic polymers consistently generated more $-\langle K \rangle$ than the $\langle N \rangle = 7$, and 9 PGON polymers. Therefore, the net effect of adding hydrophobicity to guanidinium-rich polymers is to increase the amount of negative Gaussian membrane curvature they induce.

5.2.3 Incorporation of hydrophobicity into guanidinium-rich polymers broadens the range of lipid compositions where they induce negative Gaussian curvature

Our previous results on defensins showed that negative Gaussian curvature generation was highly sensitive to lipid compositions, specifically the concentration of negative spontaneous curvature lipids in the membrane. To test the effects of reducing membrane DOPE content on the curvature generating abilities of guanidinium-rich polymers we constructed ternary DOPS/DOPE/DOPC vesicles. By changing the relative amounts of zwitterionic DOPC (spontaneous curvature, $c_0 = 0$) and DOPE ($c_0 < 0$) while holding constant the amount of anionic DOPS ($c_0 = 0$) the amount of negative spontaneous curvature lipids in the membrane can be varied at constant membrane charge density. The results are summarized in Figure 5.5. In DOPS/DOPE/DOPC = 20/70/10 membranes at P/L = 1/30 both butyl-GON and phenyl-GON generated Pn3m cubic phases with lattice parameters a = 20.51nm and a = 20.02nm, respectively (Figure 5.5A). These cubic lattices are larger than the ones observed for both polymers in 80% PE membranes, demonstrating that negative Gaussian curvature is more difficult to generate in membranes with lowered concentrations of DOPE

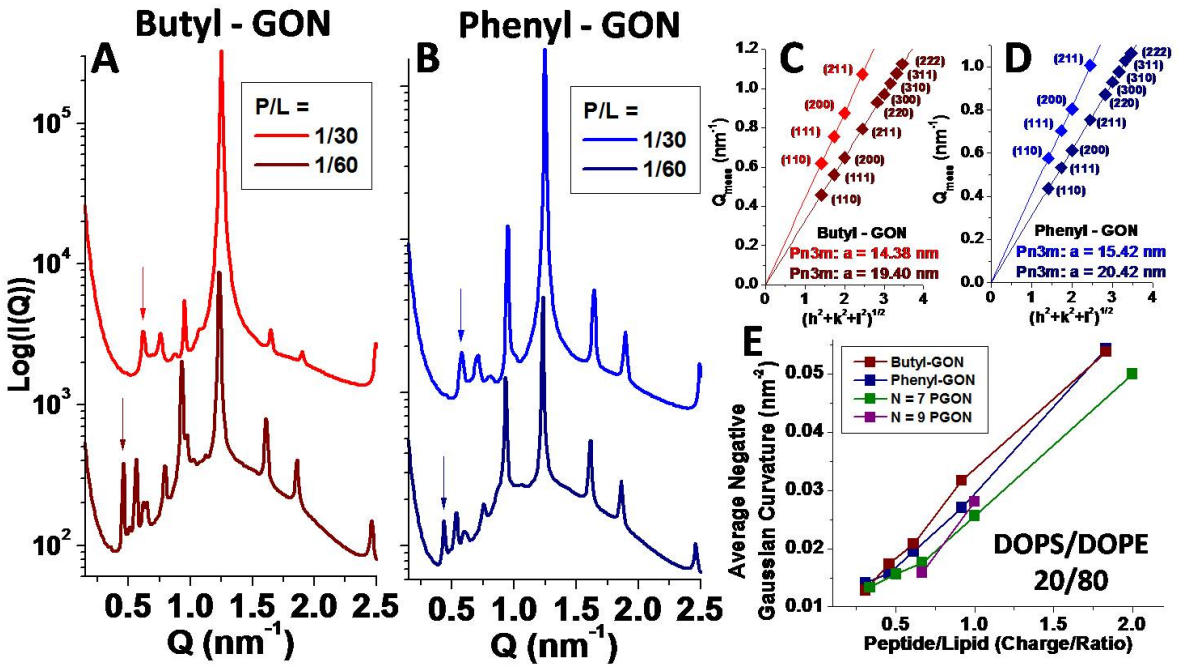

Figure 5.4: Hydrophobicity increases the amount of negative Gaussian curvature generated by guanidinium-rich polymers. A. The butyl-GON polymer, $\langle N \rangle = 11$, butyl/guanidine molar ratio = 6/5.5, generated Pn3m cubic phases in DOPS/DOPE = 20/80 membranes at peptide/lipid = 1/60 & 1/30 molar ratios. The arrow points to the first (110) reflection of the Pn3m, which shifts to higher Q for greater P/L ratios. B. A similar trend is observed for phenyl-GON polymer, $\langle N \rangle = 11$, phenyl/guanidine molar ratio = 5.5/5.5. C. & D. Indexation of the Pn3m phase lattice parameters for butyl-GON and phenyl-GON. Smaller lattices are seen for greater P/L ratios, indicating that increasing polymer concentrations produce greater amounts of negative Gaussian curvature. At a given P/L the lattice parameter for butyl-GON and phenyl-GON are close in size. E. Average negative Gaussian curvature, $-\langle K \rangle$, generated versus polymer/lipid charge ratios for polymers of similar charges and sizes. An approximately linear increase in $-\langle K \rangle$ with increasing polymer concentration is observed for each polymer. The hydrophobic butyl-GON and phenyl-GON tend to induce greater $-\langle K \rangle$ than the hydrophilic PGONs.

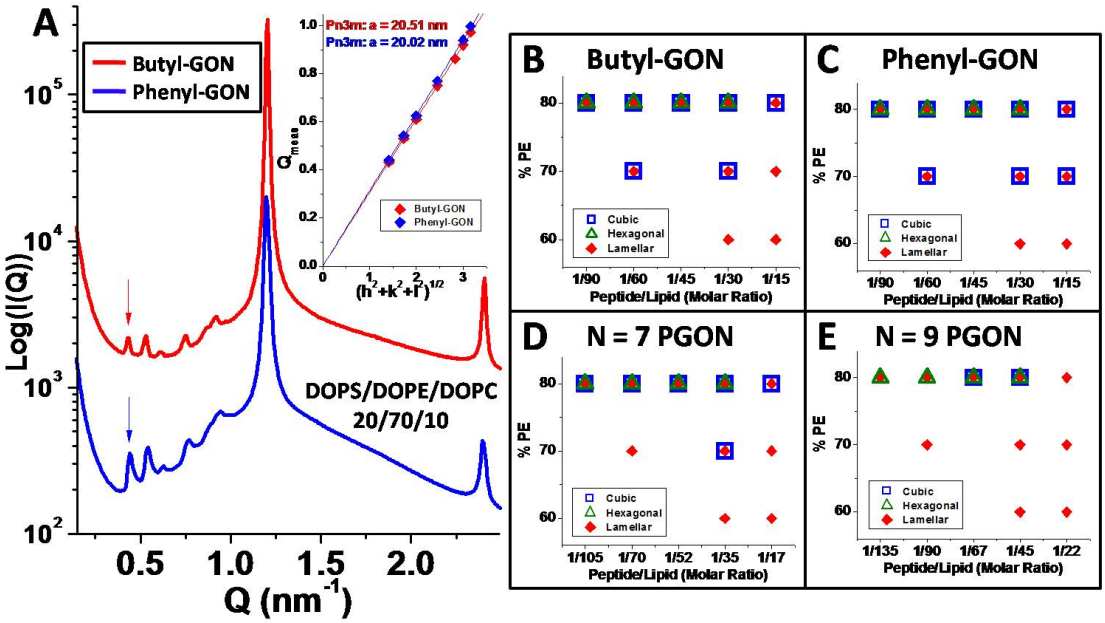

Figure 5.5: Hydrophobicity broadens the range of lipid compositions where guanidinium-rich polymers induce negative Gaussian curvature. A. Amphiphilic butyl-GON and phenyl-GON polymers both generated Pn3m cubic phases in membranes with reduced amounts of negative spontaneous curvature lipids, DOPS/DOPE/DOPC = 20/70/10. Inset shows indexation of the Pn3m cubic for both polymers. The lattice parameters for butyl-GON, a = 20.51nm, and phenyl-GON, a = 20.02nm, are approximately equivalent. B-E. Phase diagrams for guanidinium-rich polymers over a range of lipid compositions, DOPS/DOPE/DOPC = 20/x/(80-x) where x = %DOPE, and peptide/lipid ratios. The amphiphilic butyl-GON and phenyl-GON polymers generate cubic phases over a larger region of the phase diagram compared with the hydrophilic PGON polymers.

lipids. Further reducing the amount of negative spontaneous curvature lipids to 60% DOPE quashes cubic phase generation for both amphiphilic polymers (Figure 5.5B&C). Instead, pure lamellar phases are observed, which consist of stacks of flat membranes with zero curvature. Comparison of the phase diagrams for butyl-GON (Fig 5.5B) and phenyl-GON (Figure 5.5C) with the phase diagrams for $\langle N \rangle$ = 7 and 9 PGON (Figure 5.5D&E) reveal that, in general, the addition of hydrophobicity into guanidinium-rich polymers promotes saddle-splay curvature generation. Cubic phases are observed over a wider region of the phase diagram for the amphiphilic polymers, and they require less membrane PE content to generate negative Gaussian curvature.

Why does adding hydrophobicity to guanidinium-rich polymers enhance their negative Gaussian curvature generation abilities? The saddle-splay curvature selection rule states that the arginine content of a peptide can be replaced by a combination of lysine and hydrophobicity. The guanidino group of arginine generates negative Gaussian curvature while the amino group of lysine generates negative curvature only and hydrophobicity generates positive curvature. However, while poly-guanidinium polymers generally induce both positive and negative curvature, the amounts of each type of curvature may not be equivalent. Since incorporating hydrophobicity into PGON polymers enhances their generation of saddle-splay curvature, this implies PGON polymers induce less positive curvature than negative curvature. Adding hydrophobicity effectively makes up the difference resulting in an amphiphilic polymer with better membrane destabilizing activity. In the extreme case of positive curvature starved polymers such as poly-lysine which generate negative mean curvature only, even greater amounts of hydrophobicity are required. Therefore, while multi-dentate hydrogen bonding by poly-guanidinium polymers is a sufficient mechanism to buckle membranes and contribute to saddle-splay curvature generation, its effect is weaker than the positive curvature strain produced by hydrophobicity.

5.3 Conclusion

In summary we have shown that synthetic polyguanidine-oxanobornene homopolymers, (PGONs), and amphiphilic phenyl-guanidine and butyl-guanidine random copolymers all generate negative Gaussian curvature in membranes enriched with anionic lipids and negative spontaneous curvature lipids. The amount of curvature generated by PGON polymers was shown to be length dependent with maximal negative Gaussian curvature generation occurring at intermediate polymer lengths, similar to the trend observed for poly-arginine. The polymer length that maximizes negative Gaussian curvature generation for PGON is longer than poly-arginine. The larger spacing between guanidine side chains in PGON and

its stiffer backbone lessen the positive curvature strain due to multi-dentate hydrogen bonding so more guanidinium groups are necessary to compensate. Incorporation of hydrophobic butyl and phenyl groups into guanidinium-rich polymers increased the amount of negative Gaussian curvature they generate as well as broadened the range of lipid compositions over which it was observed. This implies that adding hydrophobicity to guanidinium-rich polymers enhances their negative Gaussian curvature generating abilities by supplying additional positive curvature to help balance the unequal amounts of positive and negative curvature produced by the guanidinium groups. For 1:1 guanidine:hydrophobe polymers negligible differences between the curvature generating abilities of the hydrophobic butyl and phenyl moieties were observed. We believe these results will help guide the design of cell-penetrating peptides and membrane-active antimicrobials.

5.4 Materials and Methods

5.4.1 Liposome preparation for x-ray measurements, and SAXS experiments

Liposomes were prepared as described in section 3.2.2. X-ray samples were prepared and measured as described in section 3.2.3 except for the following changes. All samples were prepared in 100mM NaCl solution. SAXS experiments at synchrotron sources were collected at Stanford Synchrotron Radiation Laboratory (BL4- 2), the Advance Light Source (ALS) (beamline 7.3.3). The scattered radiation was collected using a Rayonix MX225-HE detector (pixel size, 73.2μm) at SSRL and a Pilatus 100k detector (pixel size, 172μm). Samples were also measured at the CNSI at UCLA using an *in house* setup. A compact SAXS light source (Forvis Technologies, Inc.) was used in conjunction with a mar345 image plate detector (pixel size, 150μm).

Chapter 6

Outlook

6.1 Introduction

This thesis has focused on the types of curvature antimicrobial peptides generate in lipid membranes. Since a general mechanism of action for antimicrobial peptides is membrane disruption their fundamental structural motif, cationicity and hydrophobicity, is constrained by the topological requirement that they induce saddle-splay membrane curvature. The global trend in the arginine, lysine, and hydrophobic content of antimicrobial peptides and cell-penetrating peptides is the result of this constraint. The saddle-splay curvature selection rule provides a detailed molecular explanation for the observed trend.

Are there trends within the global trend? The complementary curvature generating abilities of lysine and hydrophobicity implies there is a positive correlation between them. However, could their be a more intricate relationship between the commonly classified hydrophobic amino acids: leucine, isoleucine, valine, methionine, alanine, phenylalanine, tryptophan, and the cationic amino acids lysine and arginine? In the first section of this chapter we sketch a possible answer.

Is it possible that the cationic and hydrophobic structural motif is employed in other biological systems to generate membrane curvature? This appears to be the case. A brief review of other cationic amphipathic molecules that generate membrane destabilizing curvatures is provided in the opening part of the second section. Are there other structural motifs which render molecules membrane-active? Again the answer is yes. A brief discussion of our

current research on an amphipathic motif distinct from the one found in AMPs concludes the second section. This different motif generates a different type of membrane curvature.

6.2 Correlations between amino acids in AMPs

Sample Pearson product-moment correlation coefficients, ρ's, are calculated to determine the degree of association between two different amino acids in AMPs sequences (see Materials and Methods). The results are shown in Figure 6.1. Lysine shows positive correlations with the hydrophobic amino acids alanine, leucine, isoleucine, and methionine, whereas arginine is anti-correlated with them (Figure 6.1A). While the negative correlation between arginine and hydrophobic amino acids may be a partial consequence of the larger negative correlation between lysine and arginine (Figure 6.1C), the message is unchanged: the presence of lysine over arginine tends to be accompanied by a greater proportion of hydrophobic amino acids, in agreement with the saddle-splay curvature selection rule. The significant exception is for the aromatic amino acid phenylalanine which is positively correlated with arginine and negatively correlated with lysine (Figure 6.1A). Furthermore, arginine is also positively correlated with tyrosine, another aromatic, while lysine shows a negative correlation with this amino acid (Figure 6.1B). Despite the small overall correlations, probably due to the great sequence diversity of membrane active AMPs, notable trends emerge.

Interestingly, studies in the complementary field of transmembrane proteins have shown that the energetically most favorable position for aliphatic residues alanine, leucine, isoleucine, and valine is at the center of the membrane, while the aromatic residues tyrosine and tryptophan prefer the membrane-water interface [229, 260], in agreement with amino acid distributions in transmembrane α-helices from integral membrane proteins [261]. Therefore, there may be a correspondance between AMPs that use aliphatic or aromatic amino acids and how deep they embed into the non-polar region of the bilayer. A future direction of this research will be to investigate the significance of the co-correlations between lysine and aliphatic

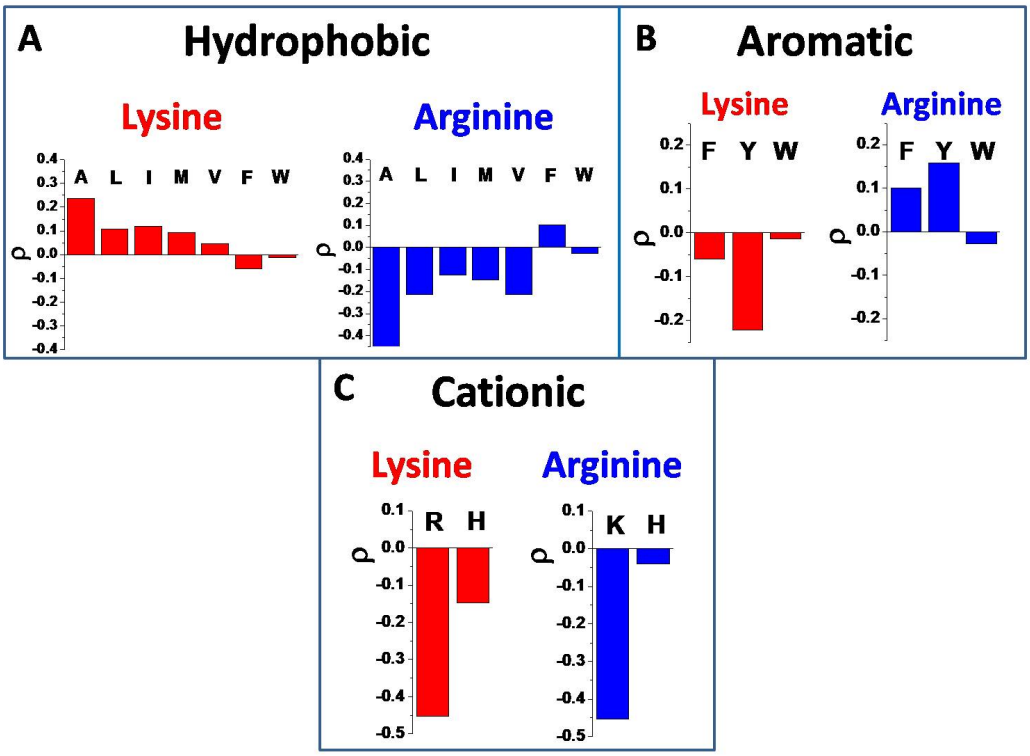

Figure 6.1: Correlation coefficients from 1080 AMP sequences show positive correlation between lysine and the hydrophobic aliphatic amino acids, while arginine is positively correlated with aromatic amino acids. A. Overall, lysine is positively correlated with the hydrophobic amino acids while arginine is negatively with them. B. Positive (negative) correlation between arginine (lysine) and aromatic amino acids. C. Cationic amino acids show negative correlations.

residues and between arginine and aromatic residues in terms of curvature generation.

6.3 Other natural amphipathic curvature generators

Membrane curvature results from non-specific electrostatic and hydrophobic interactions between lipid membranes and cationic, amphipathic molecules. Therefore, membrane-associating peptides or proteins which contain domains with similar motifs as AMPs should generate similar types of membrane curvature. For example, section 3.4 mentioned the M2 protein from the influenza virus contains an amphipathic α-helix with similar composition to AMPs, that is capable of inducing budding in vesicles. During viron release the M2 protein

localizes at the neck of budding virons, the site of maximal negative Gaussian curvature [240]. Other examples are found in proteins that modify membrane curvature for endocytic mechanisms. The epsin-1 protein promotes membrane invagination and has been implicated in clathrin-mediated endocytosis. Epsin-1 contains a highly conserved lipid binding N-terminal ENTH domain. Upon binding PtdIns(4,5)P2, an amphipathic α-helix is formed in this domain which inserts into the membrane and generates curvature. Furthermore, both epsin-1 and the ENTH domain tubulated liposomes [262, 226]. Certain BAR domains such as those found in amphiphysins and endophilins contain amphipathic α-helices at their N-terminus. An amphipathic α-helix in these N-BAR domains inserts into the membrane and acts as a molecular wedge inducing curvature along the concave surface of the BAR domain [263, 264, 265, 266]. Curvature generation by N-BAR domains has been proposed to be an important biophysical mechanism for vesicle budding [226, 265]. Other amphipathic sequences have been implicated as curvature sensors. Studies on the Golgi-associated protein ArfGAP have shown it preferentially absorbs onto membranes with strong positive curvature via a membrane associated amphipathic α-helix containing a weakly charged polar face [267, 268]. Evidently, reducing the positive charge in cationic, amphipathic molecules changes them from membrane curvature generators to curvature sensors. Taken together, these results indicate that the cationic, amphipathic structural motifs seen in AMPs are similarly employed by membrane remodeling proteins to generate controlled membrane curvature for a variety of important biological processes.

6.3.1 Amphipathic α-helices from apolipoproteins

In addition to the cationic versions mentioned above, other amphipathic helix motifs are commonly found in peptides and proteins [269]. One motif found in many apolipoproteins, the protein components of plasma lipoproteins, has attracted wide interest due its central role in atheroschlerosis. Complications of atherosclerosis, the thickening of artery walls due to the buildup of fatty materials such as cholesterol, are the leading cause of death in Western

societies [270]. Studies have demonstrated that high levels of high density lipoprotein (HDL) are inversely correlated with atherosclerotic events related to cardiovascular disease [271]. Plasma lipoproteins such as HDL consist of an outer layer of phospholipids, apolipoproteins, and cholesterol, and inner core of primarily cholesterol esters and triglycerides (Figure 6.2A). The main apolipoprotein of HDL, apoA-I, plays a critical role as apo A-I binds increasing amounts of cholesterol and phospholipids enlarging the HDL particle. The lipid-rich HDL are subsequently transported to the liver where cholesterol can be removed from circulation [272].

ApoA-I is a 243 amino acid protein that contains a series of amphipathic α-helical repeats which are responsible for its lipid associating properties [273] (Figure 6.2B). By mimicking the amphipathic helical motif in apoA-I, peptide mimetics of apoA-I have been synthesized as therapeutic agents to improve upon HDL function and reduce levels of atherosclerosis. The 4F peptide (aka D4F or L4F, based on the enantiomer used) is an 18 amino acid peptide whose sequence is based on the eight 22-mer α-helices in apolipoprotein ApoA-1 [271]. Like the parent ApoA-1 protein the 4F peptide displayed similar lipid restructuring properties [271] as well as good anti-inflammatory [274] and anti-atherogenic abilities [275].

The motif of the ApoA-1 derived 4F peptide differs from membrane lytic antimicrobial peptides on the polar face of the α-helix. The polar face of AMPs simply consists of a high proportion of cationic amino acids and polar residues (Figure 6.3). However, The polar face of the 4F peptide is decorated with anionic residues in the middle, whereas the cationic residues are placed near the polar-apolar interface (Figure 6.3). Therefore, while α-helical AMPs typically have net positive charge in the +4 to +9 range, the 4F peptide has zero net charge. The intricate arrangement of charged residues on the polar face along with zero net charge cause the 4F peptide to induce a dramatically different type of curvature than the antimicrobial peptides.

In this section we briefly discuss some current research on the interaction of the 4F peptide with lipid membranes. In general, the 4F peptide generates membrane positive

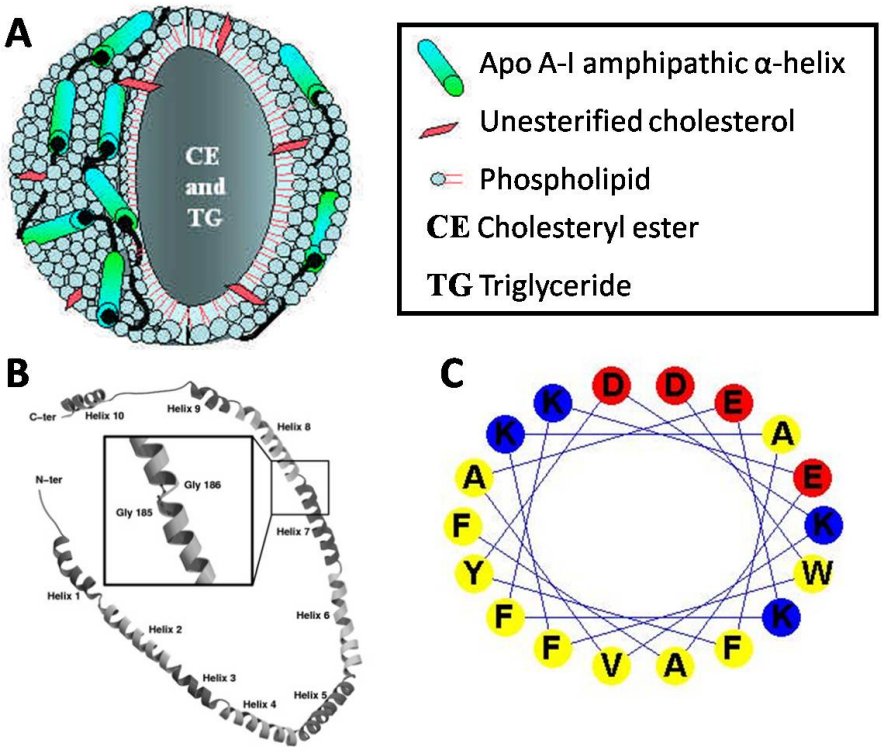

Figure 6.2: Apolipoproteins found in high density lipoprotein (HDL) contain amphipathic α-helices. A. HDL particles vary between 7-16nm in size, and are composed of an inner hydrophobic core of cholesterol esters and triglycerides, surrounded by an outer layer of phospholipids, sterols, and apolipoproteins. B. Structure of C-terminal domain of human apolipoprotein apoA-I (residues 44-243). This domain is predicted to contain eight 22-mer and two 11-mer amphipathic α-helices. C. Helical wheel projection of an ApoA-I consensus peptide: the 4F peptide. Sequence: KWFDAFYKDVAKEFEKAF. Anionic amino acids are colored red, cationic residues are blue, and hydrophobic residues are yellow. Illustration in A is from [276]. B is adopted from [277]

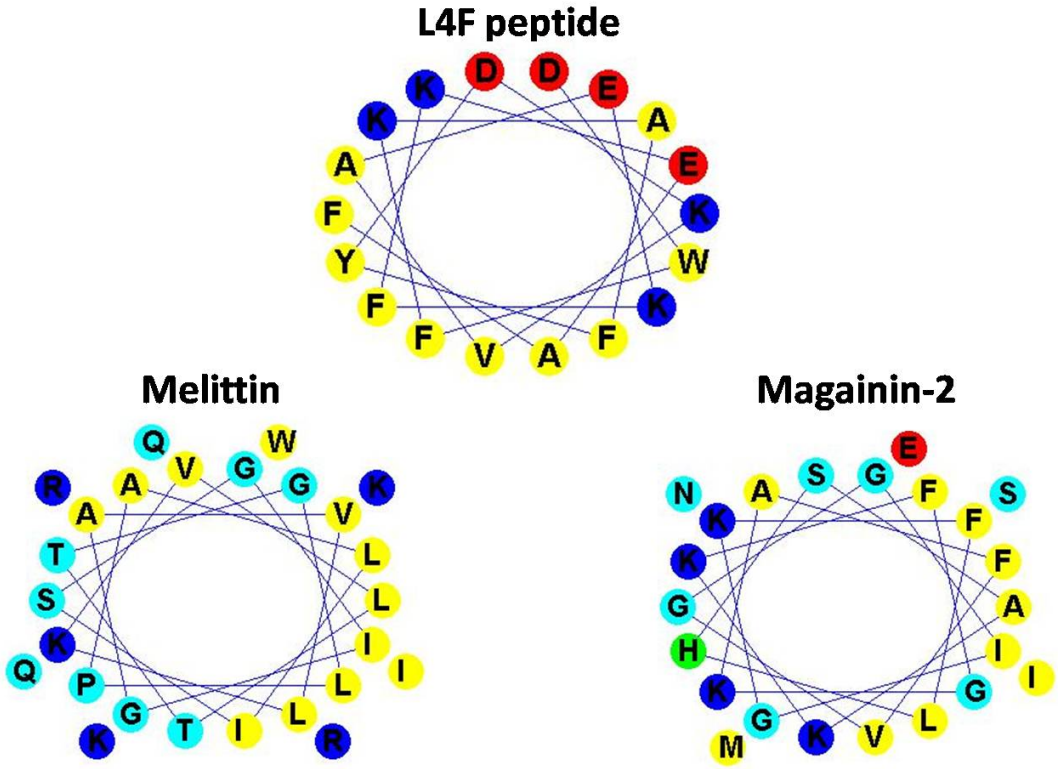

Figure 6.3: Helical wheel projections of the 4F peptide, melittin, and magainin-2. The structural motif of the 4F peptide differs from the α-helical antimicrobial peptides. Both classes are amphipathic. Differences in the distribution of charge on their polar faces affect their membrane deformation properties. Anionic amino acids are colored red, cationic residues are blue, hydrophobic residues are yellow, and polar residues are teal.

Gaussian curvature. This is not too surprising. The 4F peptide is a mimic of a protein which helps model spheroidal HDL particles. However, since positive Gaussian curvature is antagonistic to negative Gaussian curvature, the 4F peptide has the ability to 'turn off' membrane destabilizing peptides like AMPs. Small angle x-ray scattering is used to show that the 4F peptide quashes cubic phase formation by the antimicrobial peptide protegrin-1. These results are consistent with dye leakage experiments where treatment of vesicles with 4F peptide drastically reduces the ability of melittin to permeabilize membranes.

6.3.2 The D4F peptide does not restructure model liposomes

Small unilamellar vesicles (SUVs) with lipid composition DOPS/DOPE = 20/80 were incubated with D4F. SAXS profiles from the lipid solutions only show a broad feature from the form factor from an isolated lipid bilayer consistent with small unilamellar vesicles (Figure 6.4A). The same feature is observed when D4F is introduced (Figure 6.4A) indicating that D4F does not substantially restructure SUVs under these conditions[1]. This phase behavior is strikingly different to the substantial restructuring of DOPS/DOPE = 20/80 vesicles by membrane destabilizing antimicrobial peptides. Both melittin (Figure 6.4B) and magainin-2 (Figure 6.4C) generated the Pn3m cubic phase in membranes enriched with anionic and negative spontaneous curvature lipids. Therefore, unlike AMPs which generate negative Gaussian curvature, the D4F peptide did not deform membranes away from their (locally) flat native state.

[1]Restructuring liposomes into the discoidal or spheroidal particles commonly associated with lipoproteins requires much higher ($> 1/5$) peptide to lipid molar ratios. Furthermore, pure PC lipids are almost always used to make these particles.

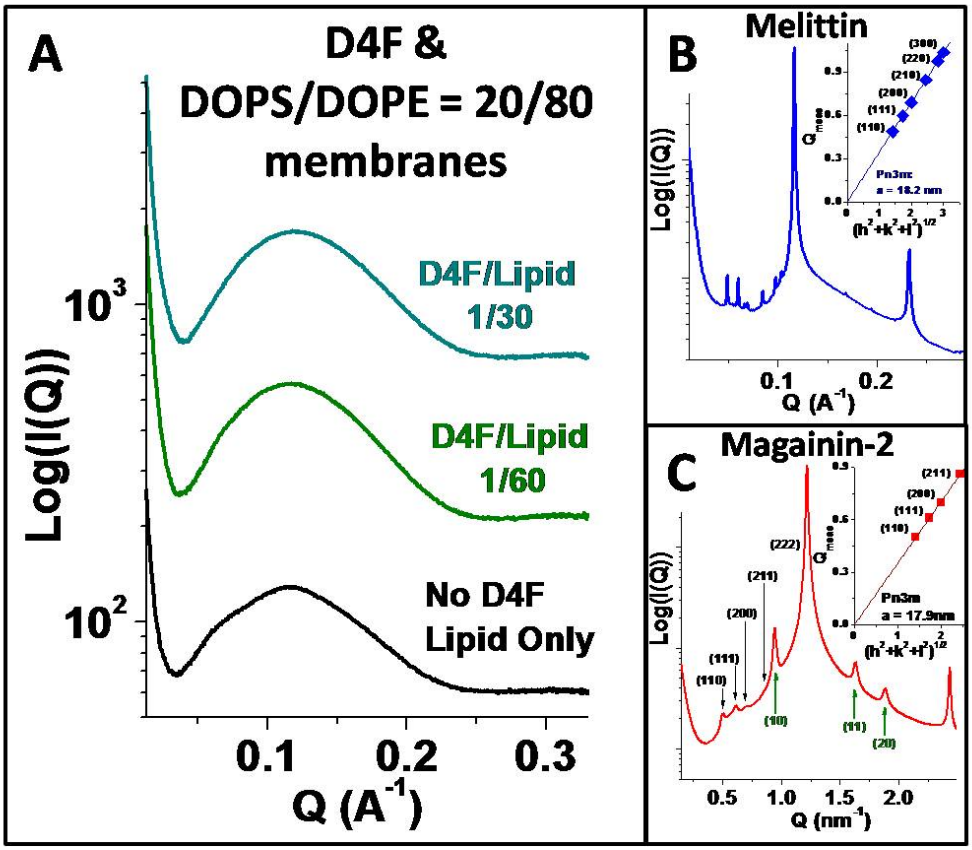

Figure 6.4: Apolipoprotein mimic peptide D4F did not restructure model bacteria membranes A. SAXS scattering spectra from DOPS/DOPE = 20/80 membranes only (black curve) are practically identical to those from membranes treated with D4F (green and teal curves). D4F/Lipid ratios are in moles. Under similar solution conditions membrane lytic antimicrobial peptides melittin, B, and magainin-2, C, restructured DOPS/DOPE = 20/80 membranes into Pn3m cubic phases with lattice parameters 18.2nm and 17.9nm, respectively. Insets show indexing of the cubic peaks. Peptide to lipid molar ratios are 1/40 for melittin and 1/60 for magainin-2. SAXS spectra in B&C are the same as in Figure 3.10.

6.3.3 The L4F peptide drastically reduces membrane permeabiliztion by melittin

To understand the effects of 4F peptides on membrane integrity large unilamellar vesicles (LUVs) were loaded with calcein dye and treated with L4F, and the dye leakage was monitored using fluorimetry as a function of time. The leakage profile for L4F was indistinguishable from the background (Figure 6.5). This behavior differs substantially from the behavior of melittin, the principle component of European honey bee venom [230]. Melittin is a 26 amino acid peptide with potent membrane disruption activity against both eukaryotic cells and bacteria [231, 232, 233]. Good dye leakage ($> 80\%$) was evident after exposure to melittin, consistent with its strong membrane permeabilizing ability (Figure 6.5). However, when melittin was added to vesicle solutions pre-treated with L4F, an eight fold reduction of leakage ($< 10\%$) was observed relative to the melittin only case (see Materials and Methods). The strong reduction of leakage indicates the 4F peptides can render membranes more resistant to permeabilization by inhibiting the mode of action of membrane lytic peptides.

6.3.4 The D4F peptide antagonizes negative Gaussian curvature generation by protegrin-1

To examine the effects of D4F on the membrane restructuring abilities of lytic peptides SUVs were co-incubated with a constant concentration of protegrin-1 (PG1), and varying concentrations of the D4F peptide. Protegrin-1 is an 18 amino acid cathelicidin originally isolated from porcine leukocytes, which displays potent broad spectrum activity against both Gram positive and Gram negative bacteria, but also shows hemolytic activity toward human erythrocytes [74, 124]. In the absence of D4F, PG1 restructured DOPS/DOPE = 20/80 vesicles into coexisting Pn3m cubic and inverted hexagonal phases with lattice parameters $a_{Pn3m} = 21.6nm$ and $a_{H_{II}} \sim 7.5nm$, respectively (Figure 6.6A&C). Therefore, PG1 generated both negative Gaussian curvature and negative mean curvature in model bacteria cell

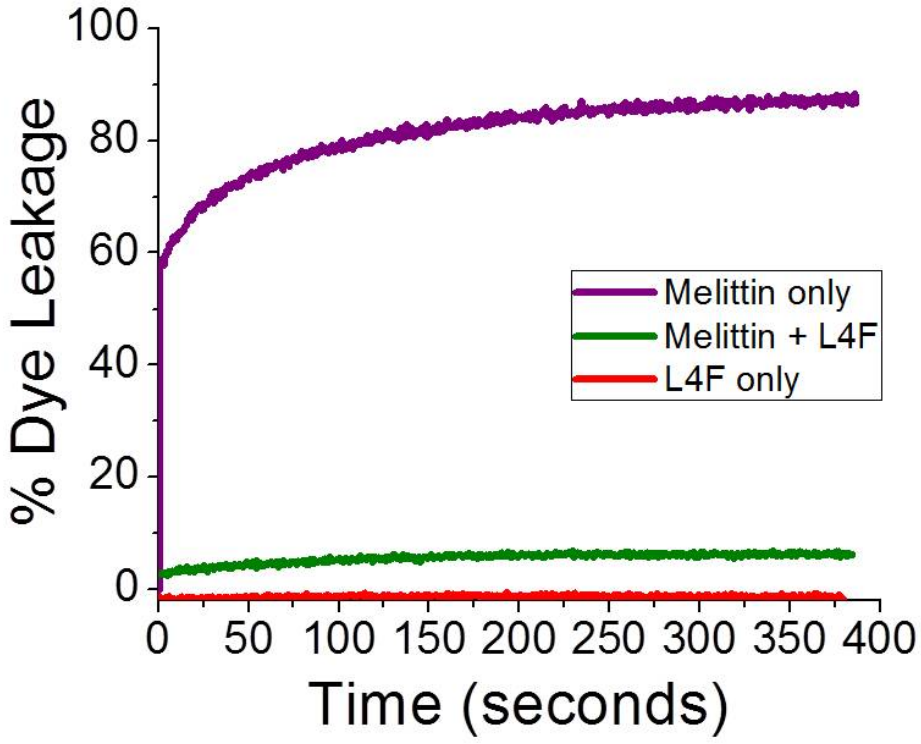

Figure 6.5: The leakage of dye from LUVs due to melittin exposure is inhibited by L4F. In vesicles with lipid composition DOPS/DOPE/DOPC = 20/60/20 melittin induced good dye leakage (purple curve), while negligible leakage was seen with L4F (red curve). When both melittin and D4F are present much less leakage occurred (green curve) than with melittin only. Peptide to lipid ratios are 1/15 for D4F and 1/50 for melittin. See Materials and Methods for details.

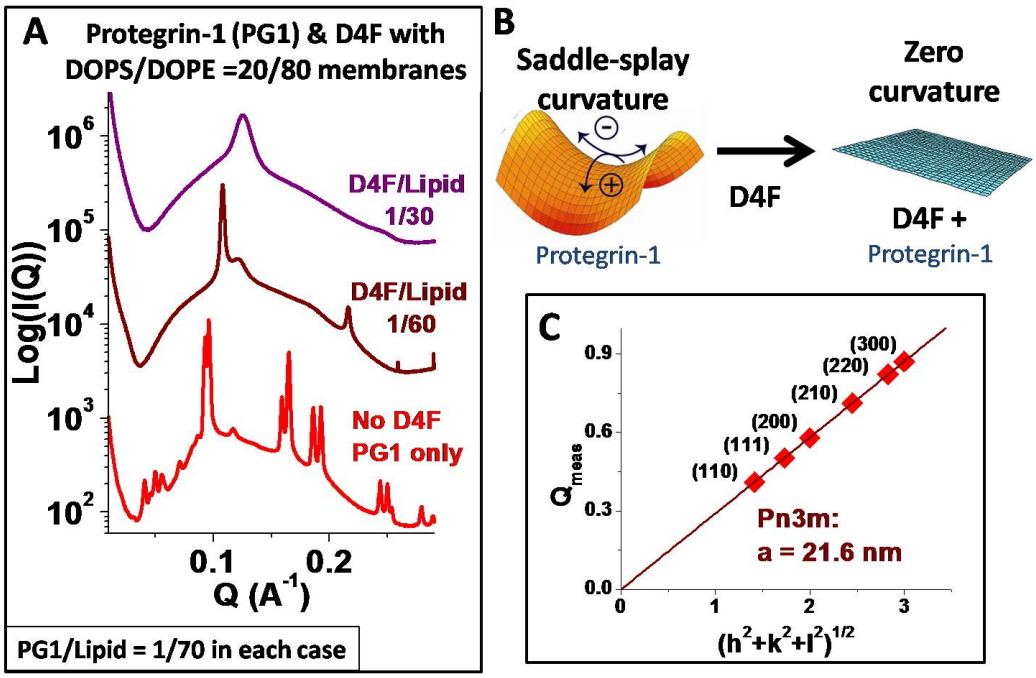

Figure 6.6: The D4F peptide turned off the negative Gaussian curvature and negative Mean curvature generated by the antimicrobial peptide protegrin-1 (PG1). A. At peptide/lipid = 1/70, PG1 generated coexisting Pn3m cubic and inverted hexagonal phases in DOPS/DOPE = 20/80 membranes. The 'double-peak' feature of the inverted hexagonal phase implies this sample may not be completely at equilibrium. When D4F is present only lamellar phases (lattice parameters d = 5.8nm for D4F/Lipid = 1/60, & d = 5.0nm for D4F/Lipid = 1/30) are observed. B. Schematic explaining that D4F stomps out saddle-splay curvature generated by PG1. C. Indexation of the Pn3m cubic phase generated by PG1 in DOPS/DOPE = 20/80 membranes.

membranes. Upon addition of the D4F peptide the correlation peaks corresponding to both the cubic and inverted hexagonal phases disappeared and were replaced by reflections with ratio, 1:2, indicating the presence of zero curvature lamellar phases (Figure 6.6A). While D4F is unable to substantially restructure vesicles its membrane interactions inhibit the generation of negative Gaussian curvature and negative mean curvature by PG1. Since negative Gaussian curvature is topologically required for membrane destabilization, the effect of D4F is to stabilize membranes by antagonizing the topologically-active curvature deformations generated by permeabilizing agents such as membrane lytic peptides (Figure 6.6B).

6.3.5 Discussion and conclusion

Differences in the polar faces of the 4F peptide and the α-helical membrane lytic antimicrobials are responsible for their distinct membrane curvature generating properties. The polar face of AMPs are usually populated by a large amount of cationic charges. As explained in Chapter 3, anionic membranes tend to wrap cationic peptides so their interaction generally produces negative mean curvature. This is complementary to the effect of hydrophobicity which acts as a molecular wedge and inserts into the membrane to produce positive curvature. Therefore, cationic and hydrophobic AMPs generate both negative and positive curvature, or negative Gaussian curvature. However, the polar face of the 4F peptide has zero net charge, and so this peptide does not promote membrane wrapping. Instead, the 4F peptide generates positive curvature only, or positive Gaussian curvature. Positive Gaussian curvature generation still requires strong interaction between the peptide and the anionic membrane. To ensure optimal contact between the 4F peptide and membrane the cationic amino acids are located around the polar-apolar interface so they can easily interact with the phosphates and other anionic moieties in lipid headgroups. Placing the anionic amino acids in the middle of the polar face keeps them further away from the lipid headgroups, but in an ideal position to electrostatically penalize membrane wrapping.

The contamination of negative Gaussian curvature by positive Gaussian curvature is summarized in Figure 6.7. Saddle-splay curvature deformations can cooperate to produce pores leading to the loss of barrier function of cell membranes (Figure 6.7A). Existing theoretical work supports the idea that anisotropic saddle-splay curvature defects attract each other [224, 278] and can stabilize pore structures in membranes [225]. However, when positive Gaussian curvature 'domes' are mixed together with saddle-shaped curvature patches the domes can antagonize pore formation (Figure 6.7B) and therefore reduce permeabilization.

In summary we show that a structural motif from the α-helices in apolipoprotein ApoA-I generates positive Gaussian curvature in lipid membranes. The specific arrangement of

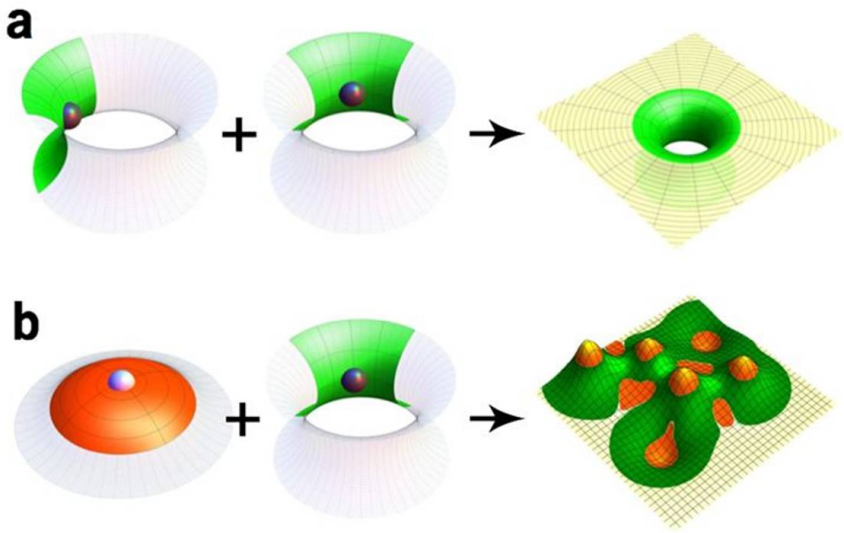

Figure 6.7: The synergistic and antagonistic effects of different curvature deformations. A. Saddle-shaped negative Gaussian curvature deformations combine to tile the interior of a pore. B. Combining negative Gaussian curvature saddles with positive Gaussian curvature domes leads to 'egg-carton' structures without pores. Figure adopted from [279].

charge on the polar face of the ApoA-I derived 4F peptide leads to strong peptide-membrane interactions without promoting negative curvature deformations from membrane wrapping. The molecular mechanisms of positive Gaussian curvature generation by the 4F peptide is entirely consistent with the molecular mechanisms of negative Gaussian curvature generation by membrane lytic peptides like AMPs. Since positive Gaussian curvature is antagonistic to negative Gaussian curvature, the structural motifs similar to those found in the α-helices of ApoA-I may be used to inhibit unwanted instances of saddle-splay curvature. In addition to bee stings, possible targets include: the endocytic and exocytic events that are essential in the replication cycle of enveloped viruses [280], and cell-cell fusion events such as those which occur during fertilization [281]. Therefore we believe this positive Gaussian curvature structural motif can be used in the rational design of new therapeutic agents.

6.4 Materials and Methods

6.4.1 Pearson's product-moment sample correlation coefficient calculations

The dataset of 1080 cationic AMPs from Chapter 3 was used for Pearson's product-moment sample correlation coefficient analysis. The sample correlation coefficient between the amino acids X and Y in a dataset of AMPs of size N, is defined

$$\rho_{XY} \equiv \frac{\sum_{i=1}^{N}(X_i - \langle X\rangle)(Y_i - \langle Y\rangle)}{\sqrt{\sum_{i=1}^{N}(X_i - \langle X\rangle)^2}\sqrt{\sum_{i=1}^{N}(Y_i - \langle Y\rangle)^2}} \tag{6.1}$$

where the X_i's are the number of instances the amino acid X is found in the ith peptide. The averages are written in the usual way

$$\langle X\rangle = \frac{1}{N}\sum_{i=1}^{N} X_i \tag{6.2}$$

The sequence lengths of antimicrobial peptides differ and this must be taken into account. Therefore, we want the correlation between amino acids X and Y while controlling for the effects of sequence length, L. This is known as partial correlation and is defined

$$\rho_{XY\cdot L} \equiv \frac{\rho_{XY} - \rho_{XL}\rho_{YL}}{\sqrt{1-\rho_{XL}^2}\sqrt{1-\rho_{YL}^2}} \tag{6.3}$$

The calculated partial correlation coefficients are plotted in Figure 6.1. All the plotted correlation coefficients have p-values ≤ 0.05 except the coefficients between: arginine and histidine ($p = 0.2$), arginine and tryptophan ($p = 0.38$), lysine and valine ($p = 0.14$), & lysine and tryptophan ($p = 0.65$). The lack of statistical significance for correlations with tryptophan and histidine are probably due to their infrequent usage (His constitutes 2.3% of residues found in AMP sequences while Trp constitutes 1.5%) within the collection of all

AMPs.

6.4.2 Liposome preparation for x-ray measurements, and SAXS experiments

Liposomes were prepared as described in section 3.2.2. X-ray samples were prepared and measured as described in section 3.2.3 except for the following changes. The D4F samples, and the D4F + protegrin-1 samples were prepared in 100mM NaCl and 10mM Hepes at pH 7.0. For the D4F + protegrin-1 samples both peptides were exposed to liposomes simultaneously. SAXS experiments were only collected at Stanford Synchrotron Radiation Laboratory (BL4- 2). The scattered radiation was collected using a Rayonix MX225-HE detector (pixel size, 73.2μm).

6.4.3 Fluorimetry experiments

Liposome preparation: DOPS, DOPE, and DOPC were mixed at a 20/60/20 w/w ratio. The solution was dried under N_2 and desiccated under vacuum overnight. The dried lipids are rehydrated with 1 ml buffer 1 (10mM NaCl, 50mM fluorescein, and 10mM Hepes, at pH 7.0). The hydrated mixture is incubated at 37°C for 24 hours. The resultant solution is freeze-thawed 8 times and extruded 13 times in a mini-extruder through 1 μm polycarbonate membrane to obtain LUVs. The resulting vesicles are purified by PD-10 desalting column against buffer 2 (100mM NaCl, 60mM Hepes at pH 7.0). 200ul of vesicle solution is collimated with 3ml of buffer 2 and only the first band (should be yellowish-red color) is collected into a glass vial.

Measuring dye leakage by fluorimetry: 20μl of collimated vesicle solution is diluted to 1600μl with buffer 2 inside a plastic cuvette. Fluorescence intensity is measured by the fluorimeter (λ_{exc} =490nm, λ_{em}=520nm, slits set at 1nm × 1nm). Baseline fluorescent intensity is first established by measuring the fluorescence emitted by vesicles and buffer

for 180s. Then, 400ul of peptide solution is diluted in buffer 2 (at the desired peptide to lipid molar ratio) and added to the cuvette. The cuvette is vortexed and placed back into the fluorimeter. Fluorescence intensity is then measured between 15-60min to obtain a dye leakage profile. Finally, 2μl of Triton-X detergent is added to the cuvette to get a maximum fluorescence intensity. The cuvette is vortexed and placed back into the fluorimeter until the end of the scan. For L4F & melittin samples the LUVs were incubated with L4F peptide for $\sim$10min before addition of melittin.

References

[1] Lodish, H. *Molecular Cell Biology*. W. H. Freeman and Company, New York, 4th edition, (2000).

[2] Alberts, B. *Molecular Biology of the Cell*. Garland Science, New york, 4th edition, (2002).

[3] Nelson, P. *Biological Physics*. W. H. Freeman and Company, New York, 1st edition, (2004).

[4] Andelman, D., Sackmann, Sackmann, E., and Arnold, K. *Structure and Dynamics of Membranes*. Elsevier Science Pub. Co, Amsterdam, (1995).

[5] Thompson, D. W. *On Growth and Form*. Camfridge University Press, Cambridge, United Kingdom, canto ed edition, (1992).

[6] Conner, S. D. and Schmid, S. L. *Nature* **422**(6927), 37–44 March (2003).

[7] Mayor, S. and Pagano, R. E. *Nature reviews. Molecular cell biology* **8**(8), 603–12 August (2007).

[8] Shibata, Y., Voeltz, G. K., and Rapoport, T. a. *Cell* **126**(3), 435–9 August (2006).

[9] Voeltz, G. K., Prinz, W. a., Shibata, Y., Rist, J. M., and Rapoport, T. a. *Cell* **124**(3), 573–86 February (2006).

[10] Okamoto, K. and Shaw, J. M. *Annual review of genetics* **39**, 503–36 January (2005).

[11] Chan, D. C. *Annual review of cell and developmental biology* **22**, 79–99 January (2006).

[12] McBride, H. M., Neuspiel, M., and Wasiak, S. *Current biology : CB* **16**(14), R551–60 July (2006).

[13] Paumard, P., Vaillier, J., Coulary, B., Schaeffer, J., Soubannier, V., Mueller, D. M., Brèthes, D., di Rago, J.-P., and Velours, J. *The EMBO journal* **21**(3), 221–30 February (2002).

[14] Zasloff, M. *Nature* **415**, 389–395 (2002).

[15] Brogden, K. A. *Nat. Rev. Microbiol.* **3**(3), 238–250 (2005).

[16] Hancock, R. E. W. and Sahl, H.-G. *Nat. Biotechnol.* **24**(12), 1551–1557 (2006).

[17] van Meer, G., Voelker, D. R., Feigenson, G. W., van Meer Voelker, D. R., Feigenson, G. W., G., and van Meer Voelker, D. R., Feigenson, G. W., G. *Nature reviews. Molecular cell biology* **9**(2), 112–24 February (2008).

[18] Chandler, D. *Nature* **417**(6888), 491 (2002).

[19] Gorter, E. and Grendel, F. *The Journal of Experimental Medicine* **41**(4), 439–443 (1925).

[20] Robertson, J. D. *Biochemical Society symposium* **16**, 3–43 (1959).

[21] Wiener, M. C. and White, S. H. *Biophysical journal* **59**(1), 162–73 January (1991).

[22] Wiener, M. C. and White, S. H. *Biophysical journal* **61**(2), 434–47 February (1992).

[23] Bretscher, M. S. *Scientific American* **253**(4), 86–90 (1985).

[24] Singer, S. J. and Nicolson, G. L. *Science (New York, N.Y.)* **175**(23), 720–31 February (1972).

[25] Vaz, W. L., Clegg, R. M., and Hallmann, D. *Biochemistry* **24**(3), 781–786 January (1985).

[26] Almeida, P. F., Vaz, W. L., and Thompson, T. E. *Biochemistry* **31**(29), 6739–6747 July (1992).

[27] Vaz, W. L., Criado, M., Madeira, V. M., Schoellmann, G., and Jovin, T. M. *Biochemistry* **21**(22), 5608–12 October (1982).

[28] Vaz, W L; Criado, M. *Biochimica et Biophysica Acta (BBA) - Biomembranes* **819**, 18–22 (1985).

[29] Jacobson, K., Sheets, E. D., and Simson, R. *Science (New York, N.Y.)* **268**(5216), 1441–2 June (1995).

[30] Vereb, G., Szöllosi, J., Matkó, J., Nagy, P., Farkas, T., Vigh, L., Mátyus, L., Waldmann, T. a., and Damjanovich, S. *Proceedings of the National Academy of Sciences of the United States of America* **100**(14), 8053–8 July (2003).

[31] Simons, K. and Toomre, D. *Nature reviews. Molecular cell biology* **1**(1), 31–9 October (2000).

[32] Lingwood, D. and Simons, K. *Science (New York, N.Y.)* **327**(5961), 46–50 January (2010).

[33] Pike, L. J. *Journal of lipid research* **44**(4), 655–67 April (2003).

[34] Sackmann, E. *Structure and Dynamics of Membranes.* Elsevier Science Publishing Company, Amsterdam, (1995).

[35] Silvius, D. R. *Thermotropic Phase Transitions of Pure Lipid in Model Membranes and Their Modifications by Membrane Proteins.* John Wiley & Sons, Inc, New York, (1982).

[36] Hyde, S. *The Language of Shape.* Elsevier, Ansterdam, (1997).

[37] Koltover, I., Salditt, T., Rädler, J. O., and Safinya, C. R. *Science* **281**(5373), 78–81 July (1998).

[38] Liang, H., Harries, D., and Wong, G. C. L. *Proceedings of the National Academy of Sciences of the United States of America* **102**(32), 11173–8 August (2005).

[39] Leal, C., Bouxsein, N. F., Ewert, K. K., and Safinya, C. R. *Journal of the American Chemical Society* **132**(47), 16841–7 December (2010).

[40] Landau, E. M. and Rosenbusch, J. P. *Proceedings of the National Academy of Sciences of the United States of America* **93**(25), 14532–5 December (1996).

[41] Shearman, G. C., Ces, O., Templer, R. H., and Seddon, J. M. *J. Phys.: Condens. Matter* **18**(28), S1105–S1124 July (2006).

[42] Israelachvili, J. N., Marcelja, S., and Horn, R. G. *Quarterly Reviews of Biophysics* **13**, 121–200 (1980).

[43] Israelachvili, J. N. *Intermolecular and Surface Forces.* Elsevier Inc, Amsterdam, 3rd, revis edition, (2011).

[44] Larsson, K. *Journal of Physical Chemistry* **93**, 7304–7314 (1989).

[45] Boni, L. T. and Hui, S. W. *Biochimica et biophysica acta* **731**, 177–185 (1983).

[46] Marianiti, P., Luzzati, V., and Delacroix, H. *Journal of Molecular Biology* **204**, 165–189 (1988).

[47] Helfrich, W. *Zeitschrift Naturforsch C* **28**, 693–703 (1973).

[48] Helfrich, W. *Amphiphilic mesophases made of defects, in: Physics of Defects.* North-Holland, Amsterdam, (1981).

[49] Seddon, J. M. and Templer, R. H. *Structure and Dynamics of Membranes.* Elsevier Science Pub. Co, Amsterdam, (1995).

[50] Siegel, D. P. and Kozlov, M. M. *Biophys. J.* **87**(1), 366–374 (2004).

[51] Zimmerberg, J. and Kozlov, M. M. *Nat. Rev. Mol. Cell Biol.* **7**(1), 9–19 (2006).

[52] Fischer, W. and Koch, E. *Zeitschrift für Kristallographie* **179**, 31–52 September (1987).

[53] Schwarz, U. S. and Gompper, G. *Phys. Rev. Lett.* **85**(7), 1472 (2000).

[54] Helfrich, W. and Rennschuh, H. *Colloque de Physique* **51**, C1789–95 (1990).

[55] Harper, P. and Gruner, S. *The European Physical Journal E* **2**(3), 217–228 July (2000).

[56] Zachowski, A. *The Biochemical journal* **294**, 1–14 August (1993).

[57] Epand, R. M. and Epand, R. F. *Journal of peptide science : an official publication of the European Peptide Society* **17**(5), 298–305 May (2011).

[58] Epand M., Epand, R. F., R. *Biochimica et Biophysica Acta (BBA) - Biomembranes* **1788**(1), 289–294 (2009).

[59] Bernfield, M., Götte, M., Park, P. W., Reizes, O., Fitzgerald, M. L., Lincecum, J., and Zako, M. *Annual review of biochemistry* **68**, 729–77 January (1999).

[60] Gonçalves, E., Kitas, E., and Seelig, J. *Biochemistry* **44**(7), 2692–702 March (2005).

[61] Andelman, D. *Structure and Dynamics of Membranes.* Elsevier Science Pub. Co, Amsterdam, (1995).

[62] Levin, Y. *Reports on the Progress in Physics* **65**, 1577–1632 (2002).

[63] Zimm, B. and Bret, M. *J. Biomol. Struct. Dyn.* **1**, 461–471 (1983).

[64] Grosberg, A. Y., Nguyen, T. T., and Shklovskii, B. I. *Reviews of Modern Physics* **74**, 329–345 (2002).

[65] Rädler, J. O., Koltover, I., Salditt, T., and Safinya, C. R. *Science* **275**(5301), 810–814 (1997).

[66] Moran, G. J., Krishnadasan, A., Gorwitz, R. J., Fosheim, G. E., McDougal, L. K., Carey, R. B., and Talan, D. A. *New England Journal of Medicine* **355**(7), 666–674 (2006).

[67] Bozdogan, B., Esel, D., Whitener, C., Browne, F. A., and Appelbaum, P. C. *Journal of Antimicrobial Chemotherapy* **52**(5), 864–868 (2003).

[68] Jassal, M. and Bishai, W. R. *The Lancet Infectious Diseases* **9**(1), 19–30 (2009).

[69] Shai, Y. *Biochim. Biophys. Acta, Biomembr.* **1462**(1-2), 55–70 (1999).

[70] Hancock Lehrer, R., R. E. W. *Trends in Biotechnology* **16**(2), 82–88 (1998).

[71] Yeaman, M. R. and Yount, N. Y. *Pharmacological Reviews* **55**(1), 27–55 (2003).

[72] Zasloff, M. *Proceedings of the National Academy of Sciences* **84**(15), 5449–5453 (1987).

[73] Dürr, U. H. N., Sudheendra, U. S., and Ramamoorthy, A. *Biochimica et Biophysica Acta (BBA) - Biomembranes* **1758**(9), 1408–1425 (2006).

[74] Kokryakov, V. N., Harwig, S. S. L., Panyutich, E. A., Shevchenko, A. A., Aleshina, G. M., Shamova, O. V., Korneva, H. A., and Lehrer, R. I. *FEBS Lett.* **327**(2), 231–236 (1993).

[75] Ganz, T. *Nat. Rev. Immunol.* **3**(9), 710–720 (2003).

[76] Lehrer, R. I. *Nat. Rev. Microbiol.* **2**(9), 727–738 (2004).

[77] Selsted, M. E. and Ouellette, A. J. *Nat. Immunol.* **6**(6), 551–557 (2005).

[78] Ouellette, A. J., Hsieh, M. M., Nosek, M. T., Cano-Gauci, D. F., Huttner, K. M., Buick, R. N., and Selsted, M. E. *Infect. Immun.* **62**(11), 5040–5047 (1994).

[79] Tang, Y.-Q., Yuan, J., Ösapay, G., Ösapay, K., Tran, D., Miller, C. J., Ouellette, A. J., and Selsted, M. E. *Science* **286**(5439), 498–502 (1999).

[80] Selsted, M. E., Novotny, M. J., Morris, W. L., Tang, Y. Q., Smith, W., and Cullor, J. S. *Journal of Biological Chemistry* **267**(7), 4292–4295 (1992).

[81] Agerberth, B., Lee, J.-Y., Bergman, T., Carlquist, M., Boman, H. G., Mutt, V., and JÖRnvall, H. *European Journal of Biochemistry* **202**(3), 849–854 (1991).

[82] Park, C. B., Kim, H. S., and Kim, S. C. *Biochem. Biophys. Res. Commun.* **244**(1), 253–257 (1998).

[83] Hwang, P. M., Zhou, N., Shan, X., Arrowsmith, C. H., and Vogel, H. J. *Biochemistry* **37**(12), 4288–4298 (1998).

[84] Jenssen, H., Hamill, P., and Hancock, R. E. W. *Clin. Microbiol. Rev.* **19**(3), 491–511 (2006).

[85] Ge, Y., MacDonald, D. L., Holroyd, K. J., Thornsberry, C., Wexler, H., and Zasloff, M. *Antimicrob. Agents Chemother.* **43**(4), 782–788 (1999).

[86] Trotti, A., Garden, A., Warde, P., Symonds, P., Langer, C., Redman, R., Pajak, T. F., Fleming, T. R., Henke, M., Bourhis, J., Rosenthal, D. I., Junor, E., Cmelak, A., Sheehan, F., Pulliam, J., Devitt-Risse, P., Fuchs, H., Chambers, M., O'Sullivan, B., and Ang, K. K. *International Journal of Radiation Oncology*Biology*Physics* **58**(3), 674–681 (2004).

[87] Sader, H. S., Fedler, K. A., Rennie, R. P., Stevens, S., and Jones, R. N. *Antimicrob. Agents Chemother.* **48**(8), 3112–3118 (2004).

[88] Scott, R. W., DeGrado, W. F., and Tew, G. N. *Current Opinion in Biotechnology* **19**(6), 620–627 (2008).

[89] Tew, G. N., Scott, R. W., Klein, M. L., and DeGrado, W. F. *Accounts of Chemical Research* **43**(1), 30–39 (2009).

[90] Hamuro, Y., Schneider, J. P., and DeGrado, W. F. *Journal of the American Chemical Society* **121**(51), 12200–12201 (1999).

[91] Porter, E. A., Wang, X., Lee, H.-S., Weisblum, B., and Gellman, S. H. *Nature* **404**(6778), 565 (2000).

[92] Schmitt, M. A., Weisblum, B., and Gellman, S. H. *Journal of the American Chemical Society* **129**(2), 417–428 (2006).

[93] Patch, J. A. and Barron, A. E. *Journal of the American Chemical Society* **125**(40), 12092–12093 (2003).

[94] Tew, G. N., Liu, D., Chen, B., Doerksen, R. J., Kaplan, J., Carroll, P. J., Klein, M. L., and DeGrado, W. F. *Proceedings of the National Academy of Sciences* **99**(8), 5110–5114 (2002).

[95] Arnt, L. and Tew, G. N. *Journal of the American Chemical Society* **124**(26), 7664–7665 (2002).

[96] Kuroda, K. and DeGrado, W. F. *Journal of the American Chemical Society* **127**(12), 4128–4129 (2005).

[97] Ilker, M. F., Nüsslein, K., Tew, G. N., and Coughlin, E. B. *Journal of the American Chemical Society* **126**(48), 15870–15875 (2004).

[98] Maemoto, A., Qu, X., Rosengren, K. J., Tanabe, H., Henschen-Edman, A., Craik, D. J., and Ouellette, A. J. *The Journal of biological chemistry* **279**(42), 44188–96 October (2004).

[99] Wu, Z., Hoover, D. M., Yang, D., Boulègue, C., Santamaria, F., Oppenheim, J. J., Lubkowski, J., and Lu, W. *Proceedings of the National Academy of Sciences of the United States of America* **100**(15), 8880–5 July (2003).

[100] Hadjicharalambous, C., Sheynis, T., Jelinek, R., Shanahan, M. T., Ouellette, A. J., and Gizeli, E. *Biochemistry* **47**(47), 12626–34 November (2008).

[101] Hetru, C., Letellier, L., Oren, Z., Hoffman, J. A., and Shai, Y. *Biochemical Journal* **345**, 653–664 (2000).

[102] Wade, D., Boman, A., Wå hlin, B., Drain, C. M., Andreu, D., Boman, H. G., and Merrifield, R. B. *Proceedings of the National Academy of Sciences* **87**(12), 4761–4765 (1990).

[103] Merrifield, R. B., Juvvadi, P., Andreu, D., Ubach, J., Boman, A., and Boman, H. G. *Proceedings of the National Academy of Sciences* **92**(8), 3449–3453 (1995).

[104] Yang, L., Gordon, V. D., Mishra, A., Som, A., Purdy, K. R., Davis, M. A., Tew, G. N., and Wong, G. C. L. *J. Am. Chem. Soc.* **129**(40), 12141–12147 (2007).

[105] Yang, L., Gordon, V. D., Trinkle, D. R., Schmidt, N. W., Davis, M. A., DeVries, C., Som, A., Cronan, J. E., Tew, G. N., and Wong, G. C. L. *Proc. Natl. Acad. Sci. U. S. A.* **105**(52), 20595–20600 (2008).

[106] Som, A., Yang, L., Wong, G. C. L., and Tew, G. N. *J. Am. Chem. Soc.* **131**(42), 15102–15103 (2009).

[107] Matsuzaki, K. *Biochim. Biophys. Acta, Biomembr.* **1462**(1-2), 1–10 (1999).

[108] Matsuzaki, K., Sugishita, K.-i., Ishibe, N., Ueha, M., Nakata, S., Miyajima, K., and Epand, R. M. *Biochemistry* **37**(34), 11856–11863 (1998).

[109] Huang, H. W. *Biochemistry* **39**(29), 8347–8352 (2000).

[110] Yang, L., Weiss, T. M., Lehrer, R. I., and Huang, H. W. *Biophysical Journal* **79**(4), 2002–2009 (2000).

[111] Yang, L., Harroun, T. A., Weiss, T. M., Ding, L., and Huang, H. W. *Biophysical Journal* **81**(3), 1475–1485 (2001).

[112] Ludtke, S. J., He, K., Heller, W. T., Harroun, T. A., Yang, L., and Huang, H. W. *Biochemistry* **35**(43), 13723–13728 (1996).

[113] Tang, M., Waring, A. J., Hong, M., and Tang Waring, A. J., Hong, M., M. *Journal of the American Chemical Society* **129**(37), 11438–11446 September (2007).

[114] Hallock, K. J., Lee, D.-K., and Ramamoorthy, A. **84**(5), 3052–3060 (2003).

[115] Pouny, Y., Rapaport, D., Mor, a., Nicolas, P., and Shai, Y. *Biochemistry* **31**(49), 12416–23 December (1992).

[116] Strahilevitz, J., Mor, a., Nicolas, P., and Shai, Y. *Biochemistry* **33**(36), 10951–60 September (1994).

[117] Marassi, F. M., Opella, S. J., Juvvadi, P., and Merrifield, R. B. *Biophysical journal* **77**(6), 3152–5 December (1999).

[118] Gazit, E., Boman, a., Boman, H. G., and Shai, Y. *Biochemistry* **34**(36), 11479–88 September (1995).

[119] Lee, M.-T., Chen, F.-Y., and Huang, H. W. *Biochemistry* **43**(12), 3590–9 March (2004).

[120] Spaar, A., Münster, C., and Salditt, T. *Biophysical journal* **87**(1), 396–407 July (2004).

[121] Saiman, L., Tabibi, S., Starner, T. D., Gabriel, P. S., Winokur, P. L., Jia, H. P., McCray, P. B., and Tack, B. F. *Antimicrobial agents and chemotherapy* **45**(10), 2838–2844 (2001).

[122] Kalfa, V. C., Jia, H. P., Kunkle, R. A., Tack, B. F., and Brogden, K. A. *Antimicrobial agents and chemotherapy* **45**(11), 3256–3261 (2001).

[123] Falagas, M. E. and Kasiakou, S. K. *Clin. Infect. Dis.* **40**(9), 1333–1341 (2005).

[124] Gidalevitz, D., Ishitsuka, Y., Muresan, A. S., Konovalov, O., Waring, A. J., Lehrer, R. I., and Lee, K. Y. C. *Proceedings of the National Academy of Sciences of the United States of America* **100**(11), 6302–7 May (2003).

[125] Yu, Y., Vroman, J. a., Bae, S. C., and Granick, S. *Journal of the American Chemical Society* **132**(1), 195–201 January (2010).

[126] Yonezawa, A., Kuwahara, J., Fujii, N., and Sugiura, Y. *Biochemistry* **31**(11), 2998–3004 (1992).

[127] Subbalakshmi, C. and Sitaram, N. *FEMS Microbiology Letters* **160**(1), 91–96 (1998).

[128] Boman, H. G., Agerberth, B., and Boman, A. *Infect. Immun.* **61**(7), 2978–2984 (1993).

[129] Lehrer, R. I., Barton, A., Daher, K. A., Harwig, S. S., Ganz, T., and Selsted, M. E. *The Journal of Clinical Investigation* **84**(2), 553–561 (1989).

[130] Patrzykat, A., Friedrich, C. L., Zhang, L., Mendoza, V., and Hancock, R. E. W. *Antimicrob. Agents Chemother.* **46**(3), 605–614 (2002).

[131] Territo, M. C., Ganz, T., Selsted, M. E., and Lehrer, R. *The Journal of Clinical Investigation* **84**(6), 2017–2020 (1989).

[132] Chertov, O., Michiel, D. F., Xu, L., Wang, J. M., Tani, K., Murphy, W. J., Longo, D. L., Taub, D. D., and Oppenheim, J. J. *Journal of Biological Chemistry* **271**(6), 2935–2940 (1996).

[133] Yang, D., Chen, Q., Chertov, O., and Oppenheim, J. J. *Journal of Leukocyte Biology* **68**(1), 9–14 (2000).

[134] Yang, D., Chertov, O., Bykovskaia, S. N., Chen, Q., Buffo, M. J., Shogan, J., Anderson, M., Schröder, J. M., Wang, J. M., Howard, O. M. Z., and Oppenheim, J. J. *Science* **286**(5439), 525–528 (1999).

[135] García, J.-R., Jaumann, F., Schulz, S., Krause, A., Rodríguez-Jiménez, J., Forssmann, U., Adermann, K., Klüver, E., Vogelmeier, C., Becker, D., Hedrich, R., Forssmann, W.-G., and Bals, R. *Cell and Tissue Research* **306**(2), 257–264 (2001).

[136] Garcia, J.-R., Krause, A., Schulz, S., Rodriguez-Jimenez, F.-J., Kluver, E., Adermann, K., Forssmann, U. L. F., Frimpong-Boateng, A., Bals, R., and Forssmann, W.-G. *The FASEB Journal* **15**(10), 1819–1821 (2001).

[137] Yang, D., Chen, Q., Schmidt, A. P., Anderson, G. M., Wang, J. M., Wooters, J., Oppenheim, J. J., and Chertov, O. *The Journal of Experimental Medicine* **192**(7), 1069–1074 (2000).

[138] Bowdish, D. M. E., Davidson, D. J., Scott, M. G., and Hancock, R. E. W. *Antimicrob. Agents Chemother.* **49**(5), 1727–1732 (2005).

[139] Huang, H. J., Ross, C. R., and Blecha, F. *Journal of Leukocyte Biology* **61**(5), 624–629 (1997).

[140] Kurosaka, K., Chen, Q., Yarovinsky, F., Oppenheim, J. J., and Yang, D. *The Journal of Immunology* **174**(10), 6257–6265 (2005).

[141] Befus, A. D., Mowat, C., Gilchrist, M., Hu, J., Solomon, S., and Bateman, A. *The Journal of Immunology* **163**(2), 947–953 (1999).

[142] Niyonsaba, F., Someya, A., Hirata, M., Ogawa, H., and Nagaoka, I. *European Journal of Immunology* **31**(4), 1066–1075 (2001).

[143] Van Wetering, S., Mannesse-Lazeroms, S. P., Van Sterkenburg, M. A., Daha, M. R., Dijkman, J. H., and Hiemstra, P. S. *American Journal of Physiology - Lung Cellular and Molecular Physiology* **272**(5), L888–L896 (1997).

[144] van Wetering, S., Mannesse-Lazeroms, S. P. G., van Sterkenburg, M. A. J. A., and Hiemstra, P. S. *Inflammation Research* **51**(1), 8–15 (2002).

[145] Braff, M. H., Hawkins, M. A., Nardo, A. D., Lopez-Garcia, B., Howell, M. D., Wong, C., Lin, K., Streib, J. E., Dorschner, R., Leung, D. Y. M., and Gallo, R. L. *The Journal of Immunology* **174**(7), 4271–4278 (2005).

[146] Scott, M. G., Davidson, D. J., Gold, M. R., Bowdish, D., and Hancock, R. E. W. *The Journal of Immunology* **169**(7), 3883–3891 (2002).

[147] Rosenfeld, Y. and Shai, Y. *Biochimica et Biophysica Acta (BBA) - Biomembranes* **1758**(9), 1513–1522 (2006).

[148] Mookherjee, N., Wilson, H. L., Doria, S., Popowych, Y., Falsafi, R., Yu, J., Li, Y., Veatch, S., Roche, F. M., Brown, K. L., Brinkman, F. S. L., Hokamp, K., Potter, A., Babiuk, L. A., Griebel, P. J., and Hancock, R. E. W. *Journal of Leukocyte Biology* **80**(6), 1563–1574 (2006).

[149] Murphy, C. J., Foster, B. A., Mannis, M. J., Selsted, M. E., and Reid, T. W. *Journal of Cellular Physiology* **155**(2), 408–413 (1993).

[150] Aarbiou, J., Ertmann, M., van Wetering, S., van Noort, P., Rook, D., Rabe, K. F., Litvinov, S. V., van Krieken, J. H. J. M., de Boer, W. I., and Hiemstra, P. S. *Journal of Leukocyte Biology* **72**(1), 167–174 (2002).

[151] Aarbiou, J., Verhoosel, R. M., van Wetering, S., de Boer, W. I., van Krieken, J. H. J. M., Litvinov, S. V., Rabe, K. F., and Hiemstra, P. S. *Am. J. Respir. Cell Mol. Biol.* **30**(2), 193–201 (2004).

[152] Thompson, A. C., Kirz, J., Attwood, E., Gullikson, M., Howells, M. R., Kortright, J. B., Liu, Y., and Robinson, A. L. *X-ray Data Booklet.pdf*. Lawrence Berkeley National Laboratory, Berkeley, California, 3rd edition, (2009).

[153] Frenkel, D. *Physica A* **313**(0), 1–30 January (2002).

[154] Als-Nielsen, J. and McMorrow, D. *Elements of X-ray Physics*. John Wiley & Sons, Inc, New York, 1st edition, (2001).

[155] Guinier, A. *X-ray Diffraction in Crystals, Imperfect Crystals, and Amorphous Bodies*. W. H. Freeman and Company, San Francisco, (1963).

[156] Warren, B. E. *X-ray Diffraction*. Addison-Wesley Publishing Company, Reading, Massachusetts, (1969).

[157] Vainshtein, B. K. *Diffraction of X-rays by Chain Molecules*. Elsevier Publishing Company, Amsterdam, (1966).

[158] Angelini, T. E. *Counterion Behavior in Polymers*. PhD thesis, University of Illinois, Urbana-Champaign, (2005).

[159] Pabst, G., Rappolt, M., Amenitsch, H., and Laggner, P. *Physical review. E, Statistical physics, plasmas, fluids, and related interdisciplinary topics* **62**(3 Pt B), 4000–9 September (2000).

[160] Pabst, G., Koschuch, R., Pozo-navas, B., Rappolt, M., and Laggner, P. *Journal of Applied Crystallography* **36**, 1378–1388 (2003).

[161] Harper, P. E., Mannock, D. a., Lewis, R. N., McElhaney, R. N., and Gruner, S. M. *Biophysical journal* **81**(5), 2693–706 November (2001).

[162] Turner, D. C. and Gruner, S. M. *Biochemistry* **31**(5), 1340–55 February (1992).

[163] Salditt, T., Koltover, I., Rädler, J., and Safinya, C. *Physical Review Letters* **79**(13), 2582–2585 September (1997).

[164] Pozharski, E. and MacDonald, R. C. *Biophysical journal* **85**(6), 3969–78 December (2003).

[165] Safinya, C. R., Sirota, E. B., Roux, D., and Smith, G. S. *Physical Review Letters* **62**(10), 1134–1137 (1989).

[166] Lau, a., Pincus, P., Levine, D., and Fertig, H. *Physical Review E* **63**(5), 1–9 April (2001).

[167] Arnold, K. *The Structure and Dynamics of Membranes*. Elsevier Science Publishing Company, Amsterdam, (1995).

[168] Arnt, L., Nusslein, K., and Tew, G. N. *Journal of Polymer Science Part A: Polymer Chemistry* **42**(15), 3860–3864 August (2004).

[169] Tew, G. N., Clements, D., Tang, H., Arnt, L., and Scott, R. W. *Biochimica et biophysica acta* **1758**(9), 1387–92 September (2006).

[170] DeChavigny, a., Heacock, P. N., and Dowhan, W. *The Journal of biological chemistry* **266**(8), 5323–32 March (1991).

[171] Schmidt, N., Mishra, A., Lai, G. H., and Wong, G. C. L. *FEBS Lett.* **584**(9), 1806–1813 (2010).

[172] Maiolo, J. R., Ferrer, M., and Ottinger, E. a. *Biochimica et biophysica acta* **1712**(2), 161–72 June (2005).

[173] Iwasa, A., Akita, H., Khalil, I., Kogure, K., Futaki, S., and Harashima, H. *Biochimica et biophysica acta* **1758**(6), 713–20 June (2006).

[174] Fretz, M. M., Penning, N. a., Al-Taei, S., Futaki, S., Takeuchi, T., Nakase, I., Storm, G., and Jones, A. T. *The Biochemical journal* **403**(2), 335–42 April (2007).

[175] Holowka, E. P., Sun, V. Z., Kamei, D. T., and Deming, T. J. *Nature materials* **6**(1), 52–7 January (2007).

[176] Ter-Avetisyan, G., Tünnemann, G., Nowak, D., Nitschke, M., Herrmann, A., Drab, M., and Cardoso, M. C. *The Journal of biological chemistry* **284**(6), 3370–8 February (2009).

[177] Richard, J. P., Melikov, K., Vives, E., Ramos, C., Verbeure, B., Gait, M. J., Chernomordik, L. V., and Lebleu, B. *The Journal of biological chemistry* **278**(1), 585–90 January (2003).

[178] Potocky, T. B., Menon, A. K., and Gellman, S. H. *The Journal of biological chemistry* **278**(50), 50188–94 December (2003).

[179] Richard, J. P., Melikov, K., Brooks, H., Prevot, P., Lebleu, B., and Chernomordik, L. V. *The Journal of biological chemistry* **280**(15), 15300–6 April (2005).

[180] Fittipaldi, A., Ferrari, A., Zoppé, M., Arcangeli, C., Pellegrini, V., Beltram, F., and Giacca, M. *The Journal of biological chemistry* **278**(36), 34141–9 September (2003).

[181] Ferrari, a. *Molecular Therapy* **8**(2), 284–294 August (2003).

[182] Wadia, J. S., Stan, R. V., and Dowdy, S. F. *Nature medicine* **10**(3), 310–5 March (2004).

[183] Nakase, I., Niwa, M., Takeuchi, T., Sonomura, K., Kawabata, N., Koike, Y., Takehashi, M., Tanaka, S., Ueda, K., Simpson, J. C., Jones, A. T., Sugiura, Y., and Futaki, S. *Molecular therapy : the journal of the American Society of Gene Therapy* **10**(6), 1011–22 December (2004).

[184] Kaplan, I. M., Wadia, J. S., and Dowdy, S. F. *Journal of controlled release : official journal of the Controlled Release Society* **102**(1), 247–53 January (2005).

[185] Vivès, E., Brodin, P., and Lebleu, B. *The Journal of biological chemistry* **272**(25), 16010–7 June (1997).

[186] Wender, P. a., Mitchell, D. J., Pattabiraman, K., Pelkey, E. T., Steinman, L., and Rothbard, J. B. *Proceedings of the National Academy of Sciences of the United States of America* **97**(24), 13003–8 November (2000).

[187] Mitchell, D. J., Kim, D. T., Steinman, L., Fathman, C. G., and Rothbard, J. B. *The journal of peptide research : official journal of the American Peptide Society* **56**(5), 318–25 November (2000).

[188] Futaki, S., Suzuki, T., Ohashi, W., Yagami, T., Tanaka, S., Ueda, K., and Sugiura, Y. *The Journal of biological chemistry* **276**(8), 5836–40 February (2001).

[189] Mishra, A., Gordon, V. D., Yang, L., Coridan, R., and Wong, G. C. L. *Angew. Chem., Int. Ed.* **47**(16), 2986–2989 January (2008).

[190] Schmidt, N. W., Mishra, A., Lai, G. H., Davis, M., Sanders, L. K., Tran, D., Garcia, A., Tai, K. P., McCray, P. B., Ouellette, A. J., Selsted, M. E., and Wong, G. C. L. *Journal of the American Chemical Society* **133**(17), 6720–7 May (2011).

[191] Zanetti, M. *J. Leukocyte Biol.* **75**(1), 39–48 (2004).

[192] Gelbart, W. M., Ben-Shaul, A., and Roux, D. *Micelles, Membranes, Microemulsions and Monolayers*. Springer, New York, 1st edition, (1994).

[193] Shirafuji, Y., Tanabe, H., Satchell, D. P., Henschen-Edman, A., Wilson, C. L., and Ouellette, A. J. *J. Biol. Chem.* **278**(10), 7910–7919 (2003).

[194] Tanabe, H., Qu, X., Weeks, C. S., Cummings, J. E., Kolusheva, S., Walsh, K. B., Jelinek, R., Vanderlick, T. K., Selsted, M. E., and Ouellette, A. J. *J. Biol. Chem.* **279**(12), 11976–11983 (2004).

[195] Figueredo, S., Mastroianni, J. R., Tai, K. P., and Ouellette, A. J. In *Antimicrobial Peptides,* Giuliani, A. and Rinaldi, A. C., editors, volume 618, 47–60. Humana Press (2010).

[196] Http://ca.expasy.org/tools.

[197] Garcia, A. E., Osapay, G., Tran, P. A., Yuan, J., and Selsted, M. E. *Infect. Immun.* **76**(12), 5883–5891 (2008).

[198] Tran, D., Tran, P. A., Tang, Y.-Q., Yuan, J., Cole, T., and Selsted, M. E. *J. Biol. Chem.* **277**(5), 3079–3084 (2002).

[199] Singh, P. K., Jia, H. P., Wiles, K., Hesselberth, J., Liu, L., Conway, B.-A. D., Greenberg, E. P., Valore, E. V., Welsh, M. J., Ganz, T., Tack, B. F., and McCray, P. B. *Proc. Natl. Acad. Sci. U. S. A.* **95**(25), 14961–14966 (1998).

[200] Taggart, C. C., Greene, C. M., Smith, S. G., Levine, R. L., McCray, P. B., ONeill, S., and McElvaney, N. G. *J. Immunol.* **171**(2), 931–937 (2003).

[201] Usaxs.xor.aps.anl.gov/staff/ilavsky/nika.html.

[202] Www.esrf.eu/computing/scientific/FIT2D/.

[203] Wang, Z. and Wang, G. *Nucleic Acids Res.* **32**(suppl_1), D590–592 (2004).

[204] Http://aps.unmc.edu/AP/main.php.

[205] Wang, W., Owen, S. M., Rudolph, D. L., Cole, A. M., Hong, T., Waring, A. J., Lal, R. B., and Lehrer, R. I. *J. Immunol.* **173**(1), 515–520 (2004).

[206] Yasin, B., Wang, W., Pang, M., Cheshenko, N., Hong, T., Waring, A. J., Herold, B. C., Wagar, E. A., and Lehrer, R. I. *J. Virol.* **78**(10), 5147–5156 (2004).

[207] Keller, S. L., Gruner, S. M., and Gawrisch, K. *Biochim. Biophys. Acta, Biomembr.* **1278**(2), 241–246 (1996).

[208] Prenner, E. J., Lewis, R. N. A. H., Neuman, K. C., Gruner, S. M., Kondejewski, L. H., Hodges, R. S., and McElhaney, R. N. *Biochemistry* **36**(25), 7906–7916 (1997).

[209] Hickel, A., Danner-Pongratz, S., Amenitsch, H., Degovics, G., Rappolt, M., Lohner, K., and Pabst, G. *Biochim. Biophys. Acta, Biomembr.* **1778**(10), 2325–2333 (2008).

[210] Ayabe, T., Satchell, D. P., Wilson, C. L., Parks, W. C., Selsted, M. E., and Ouellette, A. J. *Nat. Immunol.* **1**(2), 113–118 (2000).

[211] Llenado, R. A., Weeks, C. S., Cocco, M. J., and Ouellette, A. J. *Infect. Immun.* **77**(11), 5035–5043 (2009).

[212] Selsted, M. E., Miller, S. I., Henschen, A. H., and Ouellette, A. J. *J. Cell Biol.* **118**(4), 929–936 (1992).

[213] Mishra, A., Tai, K. P., Schmidt, N. W., Ouellette, A. J., and Wong, G. C. L. *Methods in enzymology* **492**, 127–49 January (2011).

[214] Harder, J., Bartels, J., Christophers, E., and Schroeder, J.-M. *J. Biol. Chem.* **276**(8), 5707–5713 (2001).

[215] Harder, J., Bartels, J., Christophers, E., and Schroder, J. M. *Nature* **387**(6636), 861 (1997).

[216] Starner, T. D., Agerberth, B., Gudmundsson, G. H., and McCray, P. B. *J. Immunol.* **174**(3), 1608–1615 (2005).

[217] Manning, G. S. *J. Chem. Phys.* **51**, 924–933 (1969).

[218] Wong, G. C. L., Tang, J. X., Lin, A., Li, Y., Janmey, P. A., and Safinya, C. R. *Science* **288**(5473), 2035–2039 (2000).

[219] Yang, L., Liang, H., Angelini, T. E., Butler, J., Coridan, R., Tang, J. X., and Wong, G. C. L. *Nat. Mater.* **3**(9), 615–619 (2004).

[220] May, S. and Ben-Shaul, A. *Biophys. J.* **73**(5), 2427–2440 (1997).

[221] Schug, K. A. and Lindner, W. *Chem. Rev.* **105**(1), 67–114 (2004).

[222] Wender, P. A., Galliher, W. C., Goun, E. A., Jones, L. R., and Pillow, T. H. *Adv. Drug Delivery Rev.* **60**(4-5), 452–472 (2008).

[223] Chou, T., Kim, K. S., and Oster, G. *Biophys. J.* **80**(3), 1075–1087 (2001).

[224] Dommersnes, P. G. and Fournier, J.-B. *Biophys. J.* **83**(6), 2898–2905 (2002).

[225] Fošnaric, M., Kralj-Iglic, V., Bohinc, K., Iglic, A., and May, S. *J. Phys. Chem. B* **107**(45), 12519–12526 (2003).

[226] McMahon, H. T. and Gallop, J. L. *Nature* **438**(7068), 590–596 (2005).

[227] Kyte, J. and Doolittle, R. F. *J. Mol. Biol.* **157**(1), 105–132 (1982).

[228] Eisenberg, D., Weiss, R. M., Terwilliger, T. C., and Wilcox, W. *Faraday Symp. Chem. Soc.* **17**, 109–120 (1982).

[229] Hessa, T., Kim, H., Bihlmaier, K., Lundin, C., Boekel, J., Andersson, H., Nilsson, I., White, S. H., and von Heijne, G. *Nature* **433**(7024), 377–381 (2005).

[230] Habermann, E. *Science* **177**(4046), 314–322 July (1972).

[231] Dempsey, C. E. *Biochimica et biophysica acta* **1031**(2), 143–61 May (1990).

[232] Blondelle, S. E. and Houghten, R. a. *Biochemistry* **30**(19), 4671–8 May (1991).

[233] Bechinger, B. *The Journal of Membrane Biology* **156**, 197–211 (1997).

[234] Zasloff, M., Martin, B., and Chen, H. C. *Proceedings of the National Academy of Sciences of the United States of America* **85**(3), 910–3 February (1988).

[235] Ladokhin, A. S. and White, S. H. *Journal of Molecular Biology* **285**(4), 1363–1369 (1999).

[236] Matsuzaki, K., Harada, M., Handa, T., Funakoshi, S., Fujii, N., Yajima, H., and Miyajima, K. *Biochimica et Biophysica Acta (BBA) - Biomembranes* **981**(1), 130–134 (1989).

[237] Hsu, C.-H., Chen, C., Jou, M.-L., Lee, A. Y.-L., Lin, Y.-C., Yu, Y.-P., Huang, W.-T., and Wu, S.-H. *Nucleic Acids Res.* **33**(13), 4053–4064 (2005).

[238] Lande, R., Gregorio, J., Facchinetti, V., Chatterjee, B., Wang, Y.-H., Homey, B., Cao, W., Wang, Y.-H., Su, B., Nestle, F. O., Zal, T., Mellman, I., Schroder, J.-M., Liu, Y.-J., and Gilliet, M. *Nature* **449**(7162), 564–569 (2007).

[239] Ganz, T. *Blood* **102**(3), 783–788 (2003).

[240] Rossman, J. S., Jing, X., Leser, G. P., and Lamb, R. A. *Cell* **142**(6), 902–913 (2010).

[241] Ericksen, B., Wu, Z., Lu, W., and Lehrer, R. I. *Antimicrobial agents and chemotherapy* **49**(1), 269–275 (2005).

[242] Lehrer, R. I. and Ganz, T. *Current opinion in immunology* **6**(1), 584–589 February (1994).

[243] Cunliffe, R. *Molecular Immunology* **40**(7), 463–467 November (2003).

[244] Aley, S. B., Zimmerman, M., Hetsko, M., Selsted, M. E., and Gillin, F. D. *Infection and immunity* **62**(12), 5397–403 December (1994).

[245] Hristova, K., Selsted, M. E., and White, S. H. *Biochemistry* **35**(36), 11888–94 September (1996).

[246] Satchell, D. P., Sheynis, T., Kolusheva, S., Cummings, J., Vanderlick, T. K., Jelinek, R., Selsted, M. E., and Ouellette, A. J. *Peptides* **24**(11), 1795–805 November (2003).

[247] Satchell, D. P., Sheynis, T., Shirafuji, Y., Kolusheva, S., Ouellette, A. J., and Jelinek, R. *The Journal of biological chemistry* **278**(16), 13838–46 April (2003).

[248] Shyamsunder, E., Gruner, S. M., Tate, M. W., Turner, D. C., So, P. T., and Tilcock, C. P. *Biochemistry* **27**(7), 2332–6 April (1988).

[249] Anderson, D. M., Gruner, S. M., and Leibler, S. *Proceedings of the National Academy of Sciences of the United States of America* **85**(15), 5364–8 August (1988).

[250] So, P. T. C., Gruner, S. M., and Erramilli, S. *Physical Review Letters* **70**(22), 3455–3458 (1993).

[251] El-Sayed Futaki, Shiroh, Harashima, Hideyoshi, A. *AAPS Journal* **11**, 13–22 (2009).

[252] Torchilin, V. P., Rammohan, R., Weissig, V., and Levchenko, T. S. *Proceedings of the National Academy of Sciences of the United States of America* **98**(15), 8786–91 July (2001).

[253] Lewin, M., Carlesso, N., Tung, C. H., Tang, X. W., Cory, D., Scadden, D. T., and Weissleder, R. *Nature biotechnology* **18**(4), 410–4 April (2000).

[254] Wender, P. a., Rothbard, J. B., Jessop, T. C., Kreider, E. L., and Wylie, B. L. *Journal of the American Chemical Society* **124**(45), 13382–3 November (2002).

[255] Wender, P. a., Kreider, E., Pelkey, E. T., Rothbard, J., and Vandeusen, C. L. *Organic letters* **7**(22), 4815–8 October (2005).

[256] Elson-Schwab, L., Garner, O. B., Schuksz, M., Crawford, B. E., Esko, J. D., and Tor, Y. *The Journal of biological chemistry* **282**(18), 13585–91 May (2007).

[257] Rothbard Jessop, T. C., Wender, P. A., J. B. *Adv. Drug Delivery Rev.* **57**(4), 495–504 (2005).

[258] Hennig, A., Gabriel, G. J., Tew, G. N., and Matile, S. *Journal of the American Chemical Society* **130**(31), 10338–44 August (2008).

[259] Mishra, A., Lai, G. H., Schmidt, N. W., Sun, V. Z., Rodriguez, A. R., Tong, R., Tang, L., Cheng, J., Deming, T. J., Kamei, D. T., and Wong, G. C. L. *Proceedings of the National Academy of Sciences* , accepted (2011).

[260] Hessa, T., Meindl-Beinker, N. M., Bernsel, A., Kim, H., Sato, Y., Lerch-Bader, M., Nilsson, I., White, S. H., and von Heijne, G. *Nature* **450**(7172), 1026–30 December (2007).

[261] Ulmschneider, M. B. and Sansom, M. S. P. *Biochimica et Biophysica Acta (BBA) - Biomembranes* **1512**(1), 1–14 (2001).

[262] Ford, M. G. J., Mills, I. G., Peter, B. J., Vallis, Y., Praefcke, G. J. K., Evans, P. R., and McMahon, H. T. *Nature* **419**(6905), 361–366 (2002).

[263] Takei, K., Slepnev, V. I., Haucke, V., and De Camilli, P. *Nat Cell Biol* **1**(1), 33–39 (1999).

[264] Farsad, K., Ringstad, N., Takei, K., Floyd, S. R., Rose, K., and De Camilli, P. *The Journal of Cell Biology* **155**(2), 193–200 (2001).

[265] Gallop, J. L., Jao, C. C., Kent, H. M., Butler, P. J. G., Evans, P. R., Langen, R., and McMahon, H. T. *EMBO J* **25**(12), 2898–2910 (2006).

[266] Jao, C. C., Hegde, B. G., Gallop, J. L., Hegde, P. B., McMahon, H. T., Haworth, I. S., and Langen, R. *Journal of Biological Chemistry* **285**(26), 20164–20170 (2010).

[267] Drin, G., Casella, J.-F., Gautier, R., Boehmer, T., Schwartz, T. U., and Antonny, B. *Nat Struct Mol Biol* **14**(2), 138–146 (2007).

[268] Drin, G. and Antonny, B. *FEBS Letters* **584**(9), 1840–1847 (2010).

[269] Segrest, J. P., De Loof, H., Dohlman, J. G., Brouillette, C. G., and Anantharamaiah, G. M. *Proteins* **8**(2), 103–17 January (1990).

[270] Navab, M., Reddy, S. T., Van Lenten, B. J., and Fogelman, A. M. *Nature reviews. Cardiology* **8**(4), 222–32 April (2011).

[271] Anantharamaiah, G. M., Mishra, V. K., Garber, D. W., Datta, G., Handattu, S. P., Palgunachari, M. N., Chaddha, M., Navab, M., Reddy, S. T., Segrest, J. P., and Fogelman, A. M. *Journal of Lipid Research* **48**(9), 1915–1923 (2007).

[272] Lund-katz, S. and Phillips, M. C. *Cholesterol Binding and Cholesterol Transport Proteins:*, volume 51 of *Subcellular Biochemistry*. Springer Netherlands, Dordrecht, (2010).

[273] Segrest, J. P., Jones, M. K., De Loof, H., Brouillette, C. G., Venkatachalapathi, Y. V., and Anantharamaiah, G. M. *Journal of lipid research* **33**(2), 141–66 February (1992).

[274] Barter, P. J., Nicholls, S., Rye, K.-A., Anantharamaiah, G. M., Navab, M., and Fogelman, A. M. *Circulation research* **95**(8), 764–72 October (2004).

[275] Navab, M. *Circulation* **105**(3), 290–292 January (2002).

[276] Lund-Katz, S., Liu, L., Thuahnai, S. T., and Phillips, M. C. *Fontiers in Bioscience* **8**, d1044–1054 (2003).

[277] Bolanos-Garcia, V. M. and Miguel, R. N. *Progress in Biophysics and Molecular Biology* **83**(1), 47–68 September (2003).

[278] Fournier, J. *Physical review letters* **76**(23), 4436–4439 June (1996).

[279] Lai, G. H., Ivashyna, O., Sanders, L. K., Christenson, E., Mishra, A., Schmidt, N. W., Akabori, K., Santangelo, C. D., Schlesinger, P. H., and Wong, G. C. L. *submitted* (2011).

[280] Fiorin, G., Carnevale, V., and DeGrado, W. F. *Science* **330**(6003), 456–458 (2010).

[281] Wassarman, P. M. *Cell* **96**(2), 175–83 January (1999).